Electrokinetic Methods and Applications in Australian Aquifer Settings: High-Dimension Electrical Tomography Imaging and Neural Network Filtration Techniques

A dissertation presented by

Joseph Rugari

In fulfilment of the requirements
for the degree of
Master of Philosophy
in the subject of
Geophysics

THE UNIVERSITY
of ADELAIDE

Submitted to the
Department of Earth Sciences,
School of Physical Sciences, Faculty of Sciences

Adelaide, July 2018

CONTENTS

LIST OF TABLES

LIST OF FIGURES

ABSTRACT

Being the driest continent in the world, there is a significant reliance on groundwater resources within many communities and industries throughout Australia. Particularly in regional areas with low rainfall and surface runoff resources, the underlying groundwater availability plays a pivotal role in population capacity and economic prosperity.

Whilst the importance of groundwater resources is indisputable, many aspects of its real world homeostatic processes, in both macro and micro scales, remain difficult to decipher and explain. Within Australia's fractured rock aquifer systems, attributed with storage of the largest volume of groundwater resources nationally, there is still only fragmented understandings of several of their principal components and capacities. This is inclusive even of key aquifer characteristics, such as total volume estimations, regeneration sources, and their flow or transportation methods.

Improved modeling capabilities and techniques based on prominent and robust hydrogeological principals are continually emerging from advancing technologies, new data sources and forward thinking. However, within the field data retrieval facet of hydrological research a seemingly slower evolution is taking place. A vast quantity of aquifer information is still derived directly from intrusive observation wells. Although the plethora of information these wells can yield in modelling is invaluable, there are some profound limitations that must still be addressed. Wells are costly to establish due to drilling expenses, can only provide single point information, and can also be disruptive to the homeostasis of the system.

The self-potential method is an electro-kinetic geophysical method that has recently been re-identified as an immensely promising groundwater technique. It is a fast, passive, inexpensive surface technique which requires no

drilling. Uniquely and most importantly however, it is the only geophysical method that is directly sensitive to not only the presence of groundwater, but also the physical flow of groundwater due to its generation of a measurable electrical signal. Previously regarded as a predominately qualitative geophysical tool, contributing factors including advancements in low-cost instrumentation and processing capabilities have meant self-potential surveys can now provide spatially significant quantitative data for a range of groundwater modelling inputs such as permeability.

The method has been recurrently reviewed since its early conception in international geophysical literature through to modern times. However, only a small quantity of this peer reviewed research has been conducted within Australia. A lesser extent of published literature therefore deals in particularly with addressing the challenges of both our harsh climate, and surface and geological conditions. With our own unique geological and hydrogeological settings, current and future challenges regarding securement of groundwater resources, and increasingly common practice of industrial geotechnical processes such as fracking, all research and findings are vital contributions to furthering our understanding of potential groundwater applications for self-potential methods on home soil.

This research thesis provides analyses of multiple electro-kinetic field research projects. New self-potential datasets have been collected in the Adelaide Hills targeting stimulated fractured-rock aquifers up to 40m below surface - a considerably deep target for the method, particularly within highly conductive Australian geological conditions. Previously collected geophysical datasets from the Adelaide Hills have been reprocessed from two to four-dimensions utulising newly constructed algorithms, then reanalysed with supporting geophysical datasets. And finally, a long term (46 day) self-potential monitoring program was conducted at a commercial-use porous media aquifer to investigate novel techniques in both autonomous groundwater flow presence investigation, and environmental noise filtering methodologies for a given self-potential dataset.

This research endeavors to draw further conclusion on the self-potential methods prospective as a value-adding and commercial viability modern geophysical technique in Australian groundwater research. Additionally, employing use of artificial neural networks (machine learning) for the self-

potential autonomous detection and environmental noise filtration methods, we highlight the current gap in geophysical literature regarding the combination of these techniques. A light is drawn to the combined techniques immensely promising future of potential applications and contributions within the wider electrical geophysics data automation and filtration space.

Much akin to our continual pursuit for mineralisation deposits, Australia is searching deeper than ever before for crucial groundwater supplies as shallower sedimentary aquifers are becoming fully utilised or depleted. As we move forward towards this new era of deepening natural resources, we must further develop both old and new tools which can enhance clarity of understanding within these challenging hydrogeological systems.

Thesis Supervisor: Graham Heinson

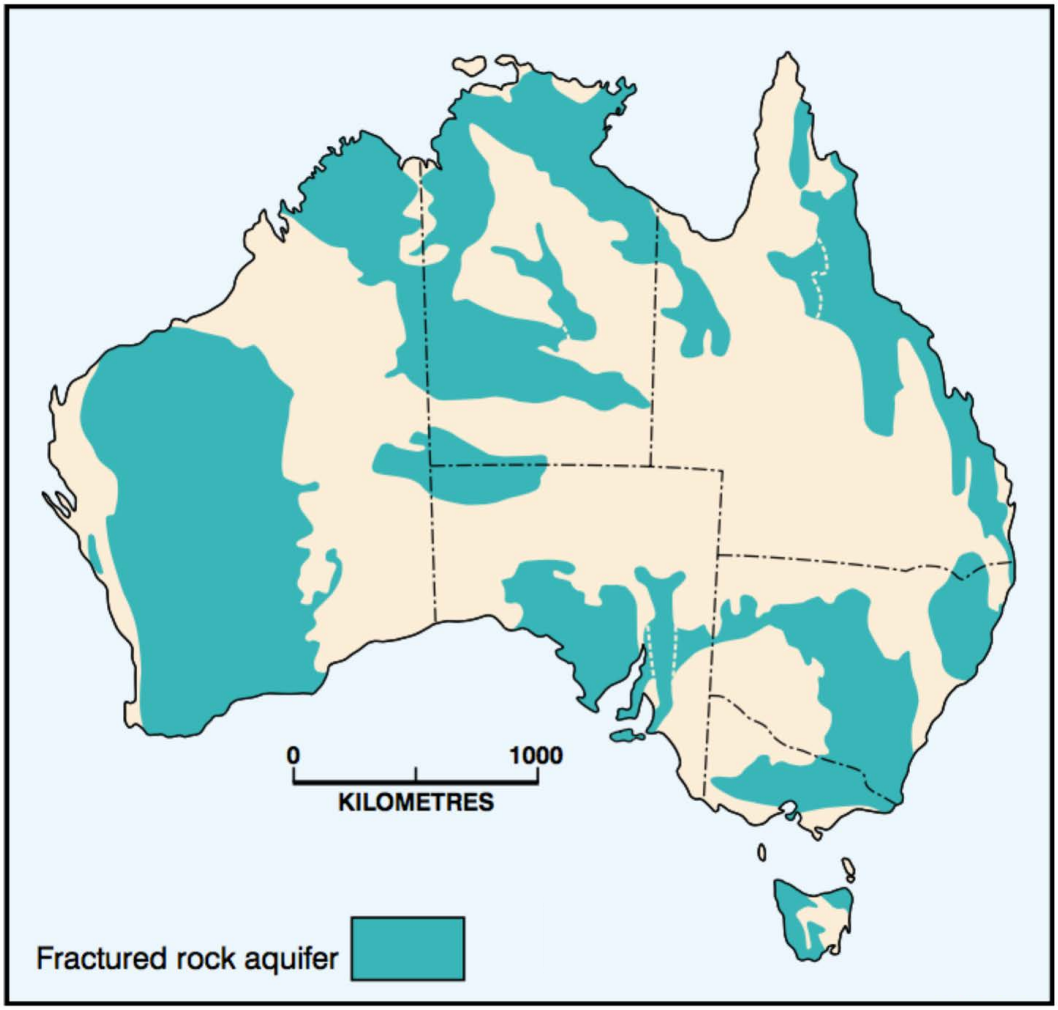

Figure 1: A map illustrating the approximate boundary locations of all major fractured rock provinces within Australia. Fractured rock aquifers underly approximately 40% of Australia, which account for a vast majority of our national groundwater resource. Regenerated from Jacobson and Lau (2017).

STATEMENT OF ORIGINALITY

I certify that this work contains no material which has been accepted for the award of any other degree or diploma in my name in any university or other tertiary institution and, to the best of my knowledge and belief, contains no material previously published or written by another person, except where due reference has been made in the text. In addition, I certify that no part of this work will, in the future, be used in a submission in my name for any other degree or diploma in any university or other tertiary institution without the prior approval of the University of Adelaide and where applicable, any partner institution responsible for the joint award of this degree.

I also give permission for the digital version of my thesis to be made available on the web, via the University's digital research repository, the Library Search and also through web search engines, unless permission has been granted by the University to restrict access for a period of time.

I acknowledge the support I have received for my research through the provision of an Australian Government Research Training Program Scholarship

I give consent to this copy of my thesis when deposited in the University Library, being made available for loan and photocopying, subject to the provisions of the Copyright Act 1968.

The author acknowledges that copyright of published works contained within this thesis resides with the copyright holder(s) of those works.

Signed

Date

ACKNOWLEDGEMENTS

I would like to thank my principal supervisor Professor Graham Heinson for his continual support, guidance, and belief in both myself and my projects throughout the entirety of my duration at the University. Also, a very special thanks to lead hardware specialist and great friend Goran Boren for teaching me to appreciate the complexities and importance of field logistics and instrumentation, but especially for the immense amount of technical support you always happily provided with a cheerful smile.

I would also like to thank fellow geophysics post-graduate students, both past and present, for providing a wonderful atmosphere and friendly work environment. I am thankful to have had the opportunity to work alongside many great personnel from various Australian universities, government agencies, and commercial and research partners. A special thanks to my closest friend through out my post-graduate studies, Dr. Dennis Conway. Dennis was a key source of motivation, academic inspiration and progressive unrestricted scientific thinking.

Finally, I would like to thank all my friends and family for their encouragement, support and confidence. Without all of you, this would not have been possible.

CHAPTER

ONE

BACKGROUND

1.1 History

The self-potential (SP) method can be summarised as a passive measurement of the electrical potential distribution at either the earth's surface or within boreholes (Revil et al., 2006). Considered the oldest of all field-utilised geophysical methods, the existence of natural polarization mechanisms associated with sulphurised ore deposits were first noted by Fox (1830).

Alike to most electrical geophysical methods, the SP method was originally envisaged and developed as a means of mineral prospecting (Sato and Mooney, 1960). Since then, the origins of many polarization source mechanisms have been proposed. Various polarization sources can be dynamic, both spatially and with time (Sato and Mooney, 1960; Corry, 1985; Ishido and Mizutani, 1981; Sivenas and Beales, 1982; Sill, 1983; Kilty, 1984; Patella, 1997a) and all these amounted together form the complex surface expressions we identify as the SP signal.

First established observations of the streaming potential, a then unknown member of the electrokinetic phenomena family, is generally accredited to Quincke (1859). Quincke demonstrated the generation and presence of

an electrical field due to the flow of water through a capillary or porous medium.

It wasn't until the 20th century that Poldini (1938) suggested use of the SP method to map these electrokinetic streaming potentials and their affiliated groundwater flow pathways. Well documented observations of self-potential signal anomalies associated with pumping tests were first recorded by Gorelik and Nesterenko (1956).

Among the geophysical methods, the self-potential method is the only one sensitive to electrokinetic streaming potentials directly associated to hydrological fluxes (Thony et al., 1997). And as these electrokinetic phenomena are a key contributor to observable Self-Potential anomalies (Aubert and Atangana, 1996; Birch, 1998; Patella, 1997a; Revil et al., 1999a, 2003), there has been ongoing focus to unravel the complex under determined nature of these surface expression to enhance hydrogeological investigations. Modern geophysical research has slowly brought the self-potential method forward from its qualitative origins, towards a more precise and quantitative technique which can now be considered one of few key groundwater flow detection methodologies.

1.1.1 Physics of self-potential phenomena

Within the ground, an electric charge polarization is naturally occurring; this is responsible for constant electric current circulation within conductive rock types.

The electrical potential distribution is the sum of two factors. Firstly, a polarization source and its associated divergence of the electrical current density. Secondly, the heterogeneous resistivity distribution of a system and its subsequent affect on electrical current pathway distributions and electrical potentials (Jouniaux and Ishido, 2012).

Using Maxwell's equations forming the classical foundation of electromagnetism (Maxwell, 1865), we can more precisely understand the fundamental macroscopic mechanisms of natural polarization at play within the earth. Fundamental electrical properties within the quasi-static limit of Maxwell's equations can describe Ohm's law, that total current density is equal to the sum of conduction current plus net source current density.

$$\boldsymbol{j} = -\sigma \nabla \varphi + \boldsymbol{j_s} \quad \text{Ohm's Law} \tag{1.1}$$

where j describes the total current density in porous material; a combination of the materials d.c. electrical conductivity σ and the electrical potential φ, determined by the systems spatial distribution and gradient of electrical potential ∇; and the net source current density in the ground j_s (Revil and Jardani, 2013). The existence of macroscopic polarization processes are intimately related to the pre-existence of a net source current density (j_s).

Note that in the current density equation, the current density j is considered to be a solenoidal (or divergenceless) vector field. Subsequently, when combining this current density equation with the continuity equation, the earth's electrical potential will obey the following:

$$\nabla^2 \varphi = \frac{1}{\sigma} \nabla \cdot \boldsymbol{j_s} + \frac{\nabla \rho}{\rho} \nabla \varphi \tag{1.2}$$

Finally, stationary current flow within an inhomogenous, isotropic half-space is governed by the formal solution of Poisson's linear differential equation at a given observation point $\boldsymbol{P}$:

$$U(\boldsymbol{P}) = \frac{1}{2\pi} \left[\int_V \frac{\rho \, div \boldsymbol{J}}{r} dV + \int_V \frac{\boldsymbol{E} \cdot grad \, \rho}{\rho \, r} dV \right] \tag{1.3}$$

Measured electrical anomalies, or SP signals, are the surface evidence of a near steady state of electrical polarization continuously at play within the earth (Patella, 1997a,b). Maxwell's equations also imply that electrical energy is transmitted instantaneously between source and any given measurement point.

1.1.2 Sources of self-potential

There are several key mechanisms that contribute to produce the mostly naturally occurring surface detectable electrical field. Some of these mechanisms provide more substantial contributions to the overall electrical field

than others, however each play their own important role within the complex near steady state system (Corwin, 1990).

Long term, lower-frequency electrical fields are principally driven by two contributing factors at play: (1) the streaming potential or hydroelectric coupling (Fournier, 1989; Birch, 1993, 1998; Aubert and Atangana, 1996; Revil and Leroy, 2001); and (2) electrochemical processes (membrane, diffusion or redox potentials) associated with gradients of the chemical potentials of ionic species in the pore water (Sen, 1991; Naudet et al., 2003, 2004; Revil et al., 2005).

An overview summary of major contributors to the earths electrical field, including their principal driving force and the laws in which to define them, and the affected fluxes are summarised within Table 1.1.

	Electric gradient	**Hydraulic gradient**	**Chemical gradient**	**Temperature gradient**
Electric	***Ohm's Law***	Electrokinetic effect	Electro-diffusion	Seebeck effect
Fluid	Electro-osmosis	***Darcy's Law***	Chemico-osmosis	Thermo-osmosis
Solute	Electrophoresis	Ultrafiltration	***Fick's Law***	Soret effect
Heat	Peltier effect	Thermal filtration	Dufour effect	***Fourier's Law***

Table 1.1: The coupled forces and fluxes which generate known electrical phenomena within the earth, and the mathematical laws in which to describe these observed phenomena. Adapted from Bader (2005) and Wurmstich (1995).

1.1.3 Physics of electrokinetic phenomena

The coupling mechanism between hydraulic flow and electrical current density is considered electrokinetic in nature. The electrokinetic phenomena are due to macro and micro-system pore pressure gradients generating fluid flow in porous media or fractures that induce electrical fields (Jouniaux and Bordes, 2012). Principally, the electrokinetic effect (otherwise known as streaming) phenomenon requires the motion of ions with the flow of a liquid.

The streaming potential is the measured voltage difference between upstream and downstream of liquid flow at zero electric current (Jiang et al., 1998; Jouniaux and Bordes, 2012; Revil et al., 1999a).

This hydraulic flow is responsible for a dipolar charge separation within the porous ground that is generally, but not always, positive in the direction of flow (Pengra et al., 1999).

Analysing the process at a micro-scale, flowing groundwater drags excess electrical charge through a porous rock. This excess charge flows through in the vicinity of the pore-water mineral interface, and at large scale produces a net current density (Revil et al., 2003).

When assuming flow is laminar, the convective electric current per unit area, j_{conv}, over a capillary or pore is given by:

$$j_{conv} = \frac{\zeta \varepsilon_r \varepsilon_0}{\eta} \overline{\nabla_n P} \tag{1.4}$$

where ζ is the zeta-potential, ε_r is the relative dielectric constant of the liquid and ε_0 is the dielectric constant of a vacuum, η is the viscosity of the fluid and $\overline{\nabla_n P}$ is the mean pressure gradient normal to the cross-section area. Note that since fluid flows in direction of negative pressure gradient ($-\nabla P$), and as ε_r, ε_0 and η are positive constants, if ζ is negative, then j_{conv} is positive in the direction of flow, and there is a resultant transport of positive charge ions with flow (Jouniaux et al., 2009).

As consequence to groundwater convection currents, an electric potential gradient (the streaming potential) is generated along the flow path. The potential gradient causes current to flow back through the liquid by electrical conduction. The conduction current per unit area, j_{cond}, is given by Ohm's law:

$$j_{cond} = -\sigma \overline{\nabla_n V} \tag{1.5}$$

Where σ is the bulk conductivity of the liquid, and $\overline{\nabla_n V}$ is potential gradient normal to the cross section.In absence of external current sources the total current is the sum of the convective and conductive currents, $j_{total} = j_{conv} + j_{cond}$ .For steady-state conditions the convective current produced

by fluid flow is balanced by the return conduction current, $j_{conv} = j_{cond}$, and the total current equals zero. A combination of (1.4) and (1.5) results in a directly proportional relationship between $\overline{\nabla_n V}$ and $\overline{\nabla_n P}$ known as the Helmholz-Smoulchovsky equation (**?**Jouniaux and Bordes, 2012):

$$\overline{\nabla_n V} = \frac{\varepsilon_r \varepsilon_0 \zeta}{\eta \sigma} \overline{\nabla_n P} = C_S \overline{\nabla_n P} \tag{1.6}$$

In (1.6), $C_S = \frac{\varepsilon_r \varepsilon_0 \zeta}{\eta \sigma}$ is the streaming potential coefficient; However, the conductive part of the current flow can only be described by (1.5), provided that conduction takes place solely in the bulk fluid.

Groundwater flow is driven by the hydraulic head gradient,∇H, rather than ∇P. Since $P = \rho g H$, where ρ is the density of the fluid (in kg/m^3), g is the specific gravity (9.81 m/s^2) and H the hydraulic head, (1.6) can be written as:

$$\overline{\nabla_n V} = \frac{\varepsilon_r \varepsilon_0 \zeta \rho g}{\eta \sigma} \overline{\nabla_n H} = C'_S \overline{\nabla_n H} \tag{1.7}$$

It can be concluded that the streaming potential gradient is proportional to the pressure gradient, and in a controlled laboratory environment (1.6) or (1.7) are excellent determinants for C_S and ζ (Revil and Jardani, 2013).

1.1.4 Physics of electrochemical phenomena

The oxidation-reduction process is considered the largest contributing electrochemical effect that can result in anomalous self-potential surface signals. Like the streaming potential, the electrochemical process takes place at the mineral-electrolyte interface and is often referred to as the redox potential (Stoll et al., 1995). Such anomalies are hypothesised to result from electromotive forces in the ground, arisen from differences in the redox potential that can significantly vary with depth (Sato and Mooney, 1960).

The earth's redox zones are determined most often by depth, and split by a line of zero potential. These redox zones are classified as either a highly oxidizing region near the earth's surface (cathode), or a highly reducing region at some depth (anode). Often referred to as a geobattery, graphically

represented in Figure 1.1, an electric dipole field is induced if an electronic conductor (such as a sulphuric ore) connects the domains of varied redox potentials (Sivenas and Beales, 1982; Timm and Möller, 2001; Bigalke and Grabner, 1997).

In order to produce a large and measurable self-potential anomaly, both the redox potential difference between cathode and anode zones, and the conductivity ratio of the electronic and ionic conductor must be large (Bigalke and Grabner, 1997; Furness, 1992).

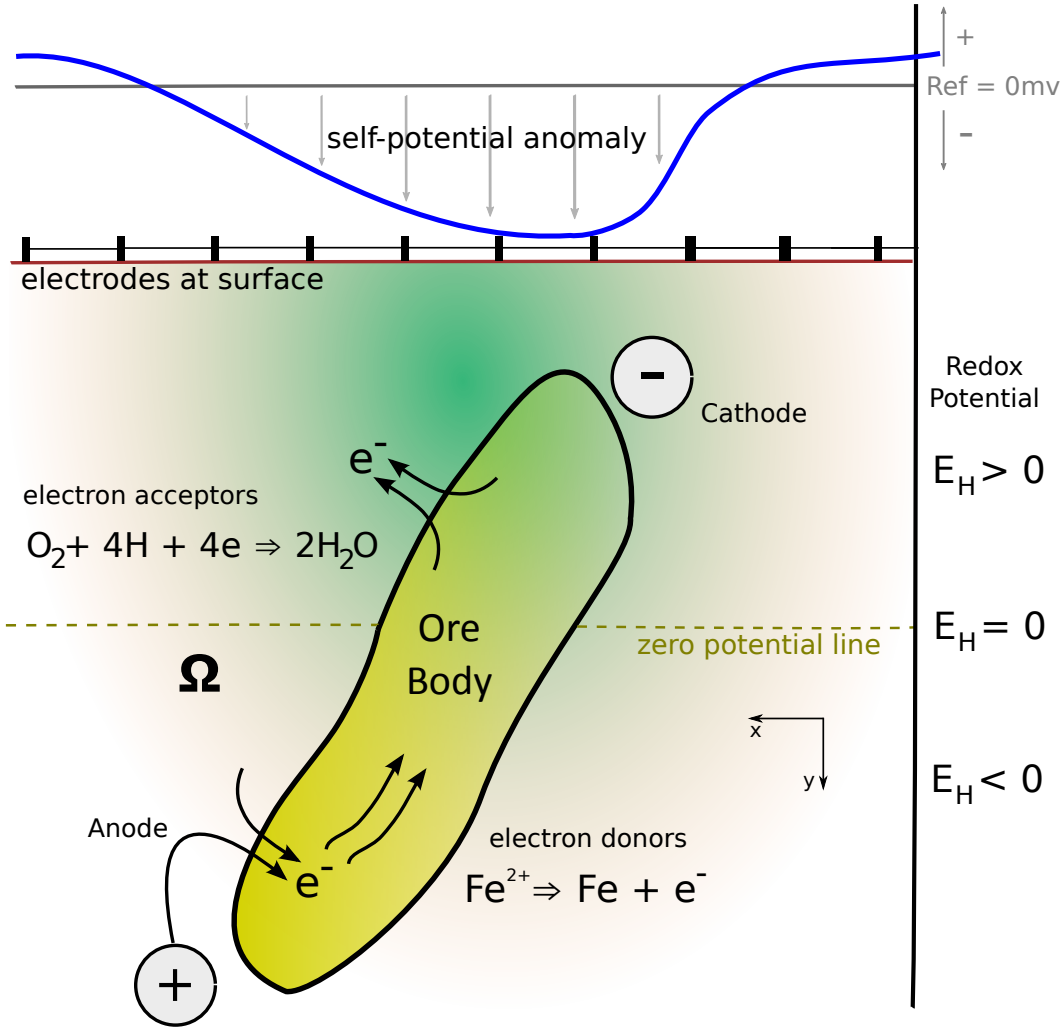

Figure 1.1: Schematic representation of a geobattery - an induced electric dipole field caused by a electronic conductor, in this case a sulphuric ore body, in contact with both shallow (oxidizing) and deep (reducing) redox potential zones. Origins of the self-potential technique in mineral exploration relied primarily on these geobattery structures which are known to cause a significant electrical potential phenomena. A self-potential anomaly is therefore present at the earths surface, detectable and measurable by a singular or array of surface electrodes. Reproduced from original figure by Bigalke and Grabner (1997)

In a geobattery model where electrons are only transferred from an ionic to an electronic conductor and vice versa, and any external charge sources do not exist (Bigalke and Grabner, 1997):

$$\nabla \cdot \vec{j}_i = -\nabla \cdot \vec{j}_e \tag{1.8}$$

With $\vec{j}_i$ the ionic current density (in J/mol) and $\vec{j}_e$ the electronic current density (in A/m^2). As the anomalies result from the initial ionic current $\vec{j}_i$, from the Ohmic law we can describe:

$$\vec{j}_i = \sigma_i \nabla \phi \tag{1.9}$$

where ϕ is the electrical potential (in V), and σ_i the ionic conductivity of the rock, assumed to be a scalar function.

A method for testing of specific ionic redox signals in the field is possible and discussed in Timm and Möller (2001). Similar to the self-potential technique, the redox potential of an active system is measured by placing a high-grade metal (eg. platinum) and reference electrode in very close proximity to another.

CHAPTER

TWO

ELECTROKINETICS

2.1 Petrophysics

The natural electrokinetic phenomena can be described in more detail by the electrical double (or triple) layer and grain water interface model.

When all mineral types are in contact with groundwater that contains dissolved ions, their reactive surfaces become charged through proton exchange and sorption of these ions. The charged mineral surface is then responsible for formation of the Stern layer (Revil et al., 2003; Bockris and Khan, 2013), which additionally hosts its own net charge. Together these two net charge densities are responsible for the minerals microscopic electric field and electric potential difference (with reference to the bulk pore water). Shielding of these two net charge densities is provided by attachment of additional ions from flowing groundwater at the Stern layer. A Coulombic field is created by the charge separation of groundwaters anions and cations being attracted or repelled to the mineral surface, resulting in the Diffuse Layer of counterions. Ionic concentrations in this layer obey Boltzman statistics. This balancing of ions results in electrical potential decreasing exponentially from the grainwater interface out (Revil et al., 2006). A detailed graphical representation of the described double layer model can be viewed in Figure 2.1.

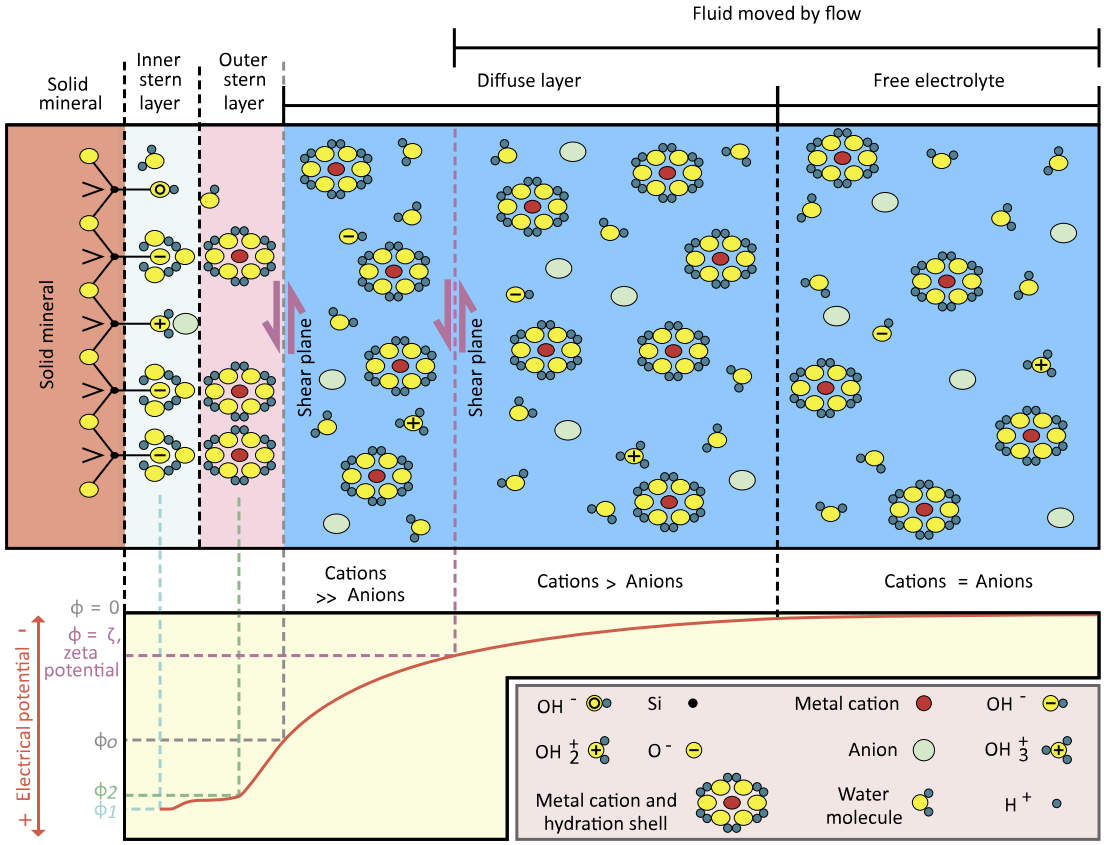

Figure 2.1: The electrical double layer of a silica grain. At pH of above the isoelectric point, excess cations of the diffuse layer are adsorbed within the inner and outer Stern layer. The zeta potential is defined at the outer shear plane of the diffuse layer. The fluid flow creates a streaming current balanced by the conduction current, thus leading to a streaming potential. Reworked from original figure by Jouniaux and Ishido (2012).

2.1.1 Zeta potential

Detectable presence of information rich SP anomalies at a surface site is dictated by numerous factors, but can be overwhelmingly attributed to the soil and bedrock lithologies zeta potentials (Corwin, 1990). The zeta potential is a quantitative summary of a rock's ability to host and transport electrical signal (Fagerlund and Heinson, 2003).

The zeta potential was first defined by Overbeek (1956), although even from a qualitative point it was poorly understood. Later, Pride (1994) unified several previous works under a generalised framework of the vari-

ous individual phenomena. In more recent time, Revil and Leroy (2001) established a framework of quantitative factors which are still utilized in determining the zeta potential of a sample.

When relative motion occurs between a mineral surface and an electrolyte, for example groundwater moving through porous sandstone, there is resulting shear within the electrical diffuse layer. Shear occurs along the 'slipping plane', and the electrical potential along this plane can be defined as the zeta potential (Revil et al., 1999a).

2.1.1.1 Calculating zeta potential

For modelling all types of electrokinetic phenomena, the zeta potential is the most fundamental parameter required to predict and interpret a resulting signal more rigorously (Revil et al., 1999b).

Several factors combined determine the zeta potential of a given sample. These include: mineral type; grain size and shape characteristics; surface electrical conductivity; hydraulic conductivity; temperature; groundwater viscosity; a solutions ionic availability or salinity; and its pH.

When at a steady state, a sample's zeta potential is calculated from streaming potential coupling coefficient (Sill, 1983). The streaming potential coupling coefficient is defined as the simultaneous ratio of streaming potential and pressure drop for a given porous sample:

$$C_S = \frac{\Delta V}{\Delta P}\Big|_{j=0} \tag{2.1}$$

Where C_s represents the streaming potential coupling coefficient, ΔV the streaming potential, and ΔP the applied steady state pressure drop. Once calculated, the zeta potential of a sample can be deduced:

$$\zeta = \frac{C_S\, \eta_f\, \sigma_f}{\epsilon_r\, \epsilon_o}\Big|_{j=0} \tag{2.2}$$

where ζ is the zeta potential to be calculated, η represents the dynamic viscosity of the fluid, ϵ_r defines relative permitivity of the fluid, ϵ_o the dielectric permittivity in a vacuum ; and σ_f is the fluid conductivity, a generally true simplification of the effective conductivity:

$$\sigma_{eff} = \sigma_f + \sigma_s = \sigma_f + 2\frac{\Sigma_s}{\Lambda} \tag{2.3}$$

where surface conductivity σ_s is dependent on conduction in the electrical double layer and Stern layer (Revil and Glover, 1998; Glover et al., 2012). Λ represents a characteristic length scale:

$$\Lambda = \frac{d}{3\left(F - 1\right)} \tag{2.4}$$

which describes the varied microstructure characteristics of the given sample (Ishido and Mizutani, 1981; Luong and Sprik, 2013). It is determined by the mean grain diameter d, and the formation factor of the given sample rock F.

2.1.2 Streaming potential coupling coefficient

There are several key parameters that greatly affect and ultimately determine both the zeta potential of a grain mineral surface, and the streaming potential coupling coefficient of a mineral or rock specimen. This section outlines these parameters in more detail, and will additionally touch on complications of linking both laboratory and theoretical test result values with real-world SP survey investigations.

2.1.2.1 Fluid conductivity

It is well established that the magnitude of the streaming potential coupling coefficient decreases as the fluid brine salinity increases (see Figure 2.2). This has been a consistent trend to all experimental measurements of streaming potential coefficients versus salinity (Wang et al., 2015; Esmaeili et al., 2016).

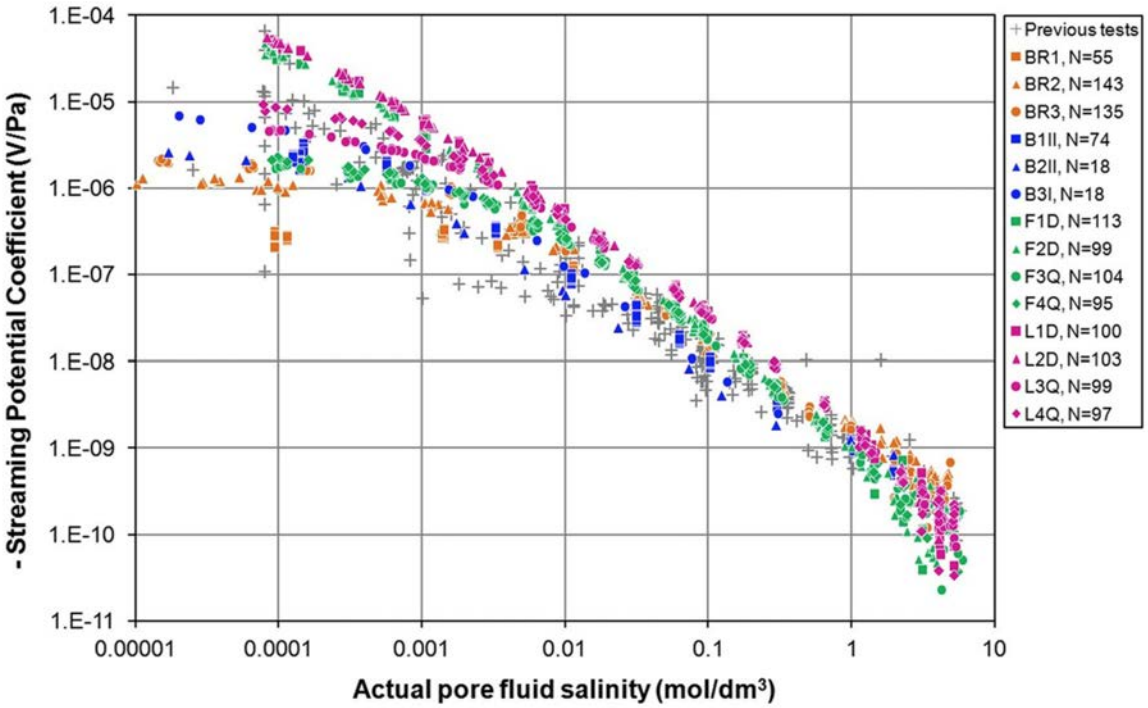

Figure 2.2: Measured streaming potential coupling coefficients from various published data sets, as a function of brine salinity. The relationship is a generally linear one, with some grain-types exhibiting non-linear features at very low and high salinities only. These non-linear relationships can be generally attributed to a samples porosity and microstructure (microstructural flattening). Figure from Walker and Glover (2018).

At very low salinities (~<0.001 mol/dm^3), there is a flattening of the streaming potential coupling coefficient curve that has been attributed to microstructural properties. The flattening is more pronounced in samples with larger formation factors and electrical tortuosities, hence reduced connectednesses and connectivities (Glover and Déry, 2010; Glover et al., 2012).

At high salinities (~>0.001 mol/dm^3), behavior is characterised by continuation of the power law relationships that exists at medium salinities. The nature of this trend can be described as a bi-logarithmic linear plot, continually reducing towards zero as fluid salinity approaches full saturation (Walker and Glover, 2018).

In laboratory testing of sandstones saturated with NaCl electrolyte, the zeta potential has been shown to no longer decrease when increasing ionic strength beyond 0.3 mol/dm^3 (Vinogradov et al., 2010; Jaafar et al., 2009).

It is suggested maximum packing of sodium (Na+) counterions within the diffuse layer is reached at this ionic strength. Therefore, as the double layer counterion density remains constant, the zeta potential will also remain constant (Vinogradov and Jackson, 2015).

2.1.2.2 Porosity, permeability and microstructure

The streaming potential coefficient is a function of both zeta potential properties and permeability, or general ability to host fluid pressure. This permeability dependence was experimentally studied by Jouniaux and Pozzi (1995) and Glover et al. (2012) with sandstones and limestones, and then combined with a model to quantify the effect of permeability on the streaming potential as shown in Figure 2.4.

In practice, it is hard to represent permeability dependence of streaming potential coefficients due to constant variance in the zeta potential from sample to sample (Luong and Sprik, 2013).

Recent laboratory studies by Thanh and Sprik (2016) have reinforced that permeability of the reservoir rock is an important parameter influencing streaming potential coefficient for fluids with low electrical conductivity. However, when fluid conductivity is larger than 0.50 S/m in natural sandstone samples, the streaming potential coefficient is independent of permeability. Regions of saline water are likely not affected by bedrock changes in permeability due to the low ratio of surface conductivity to fluid electric conductivity.

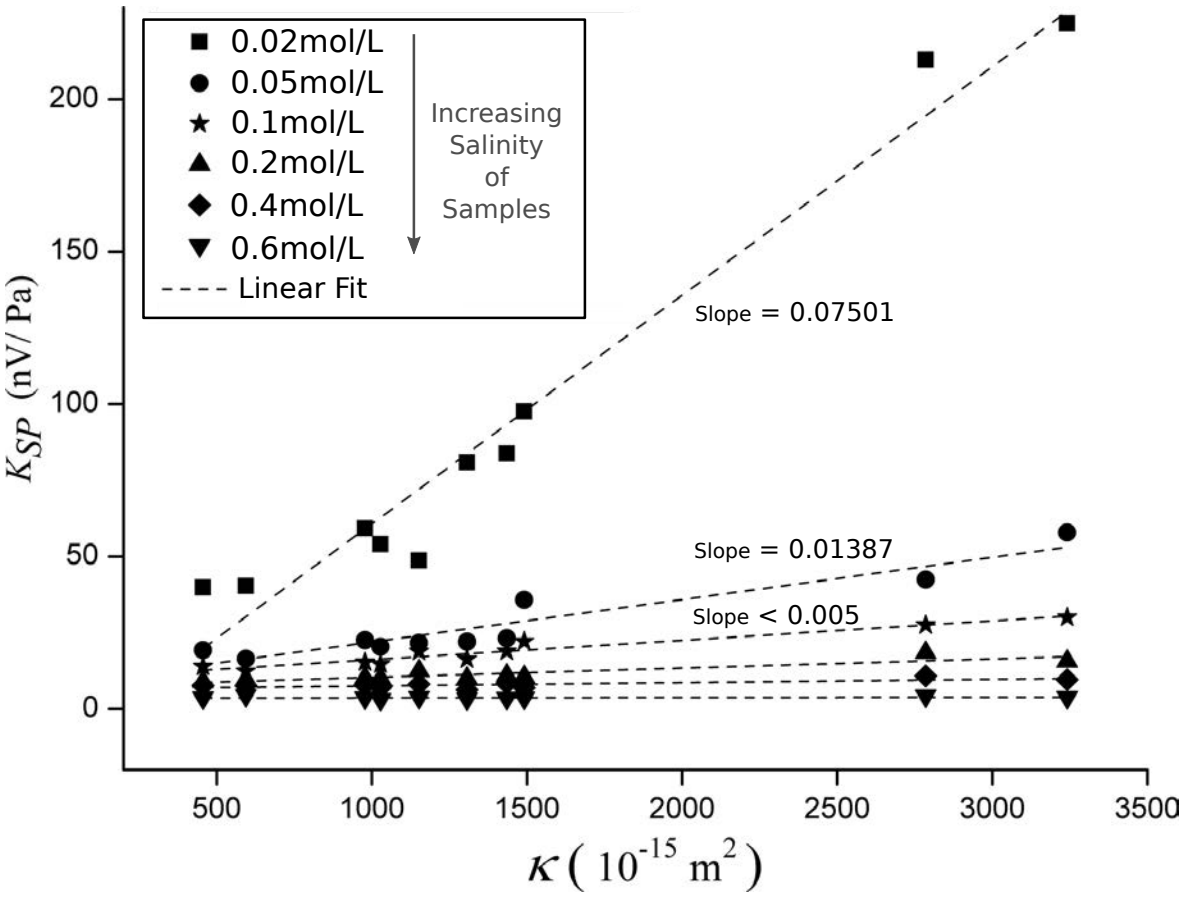

Figure 2.3: Experimental data of streaming potential coefficients, linearly increasing as a function of rock permeability at six varied salinities. The streaming potential coefficients increase as permeability increases at low salinities, but less so at high salinities. Differences in a samples microstructure, porosity and permeability are more readily identifiable at lower salinities. Figure from Walker and Glover (2018).

2.1.2.3 Fluid pH

Fluid pH can have substantial affect on the streaming potential coefficient. As represented in Figure 2.4, an increased (more basic) pH tends to increase and displace the streaming potential coefficient as a function of salinity, but does not greatly affect the associating slope angle.

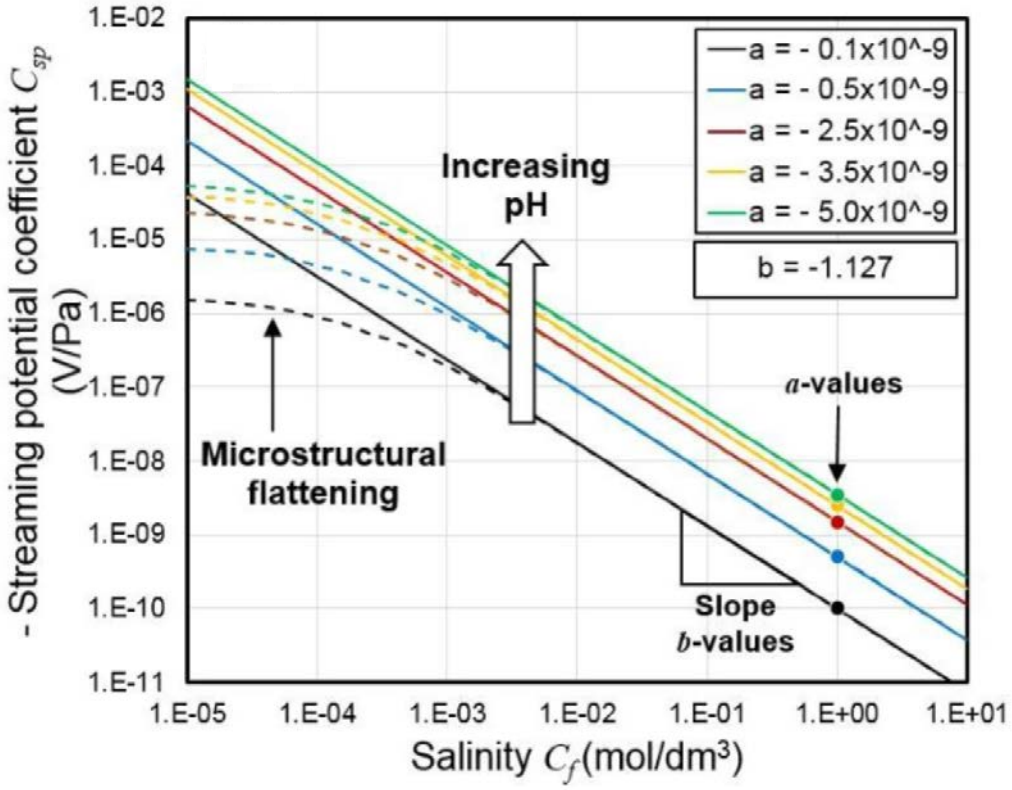

Figure 2.4: Schematic illustrating the variation of streaming potential coefficient (C_{sp}) on samples with varied pore fluid pH. Changes in pH tend to displace the C_{sp} (α-values), but do not alter their slope (β-values). Microstructural flattening can be seen to alter the C_{sp} slope at low salinities. Reworked from original figure by Walker and Glover (2018).

2.1.2.4 Surface conductivity

The surface electrical conductivity of porous materials occurs at the fluid-grain interface, and is an important parameter closely related to all forms of electrokinetic phenomena (Revil and Glover, 1998; Revil et al., 1999a,b).

Previously surface electrical conductivity's role in zeta potential was underestimated, particularly for samples with a small electrokinetic radius below 100 κa (a double layer Debrye length thickness) (Rice and Whitehead, 1965; Levine et al., 1975).

It has been seen in experimental settings that the effects of surface conductivity on zeta potential are dominant at low salinity fluid concentrations, such as that of freshwater groundwater samples. Surface electrical con-

ductance of a bedrock or sample should not be ignored as this can lead to underestimation of zeta potential (Wang et al., 2015).

2.1.2.5 Temperature

Due to few available experimental studies, and those existing reporting inconsistent behavior, the temperature dependence of the zeta potential remains somewhat poorly understood (Glover, 2015). Contradicting evidence can be found to support opposing theories that zeta potential both increases or decreases in magnitude due to temperature variations (Ishido and Mizutani, 1981; Reppert and Morgan, 2003). These contradictions are likely due to the difficulties of stabilizing all experimental controls and influences on the zeta potential.

Zeta potential variation for sandstones saturated in moderate to high fluid saline conditions greater than 0.3 mol are insensitive to any changes that would be caused by temperature(Saunders et al., 2012). Laboratory experiments with fixed pH present that zeta potential increases in magnitude with increasing temperature. The results have broad application to deep sandstone reservoirs and hydrothermal fields (Vinogradov and Jackson, 2015).

2.2 Non-static and local potentials

2.2.1 Groundwater models

Various groundwater electrical models have been determined, namely by media types in which the flow of ground water occurs. These models, graphically represented in Figure 2.5, are useful for understanding macro scale non-equilibrium electrical field fluctuations that occur during groundwater flow.

2.2.1.1 Porous media: saturated and unsaturated

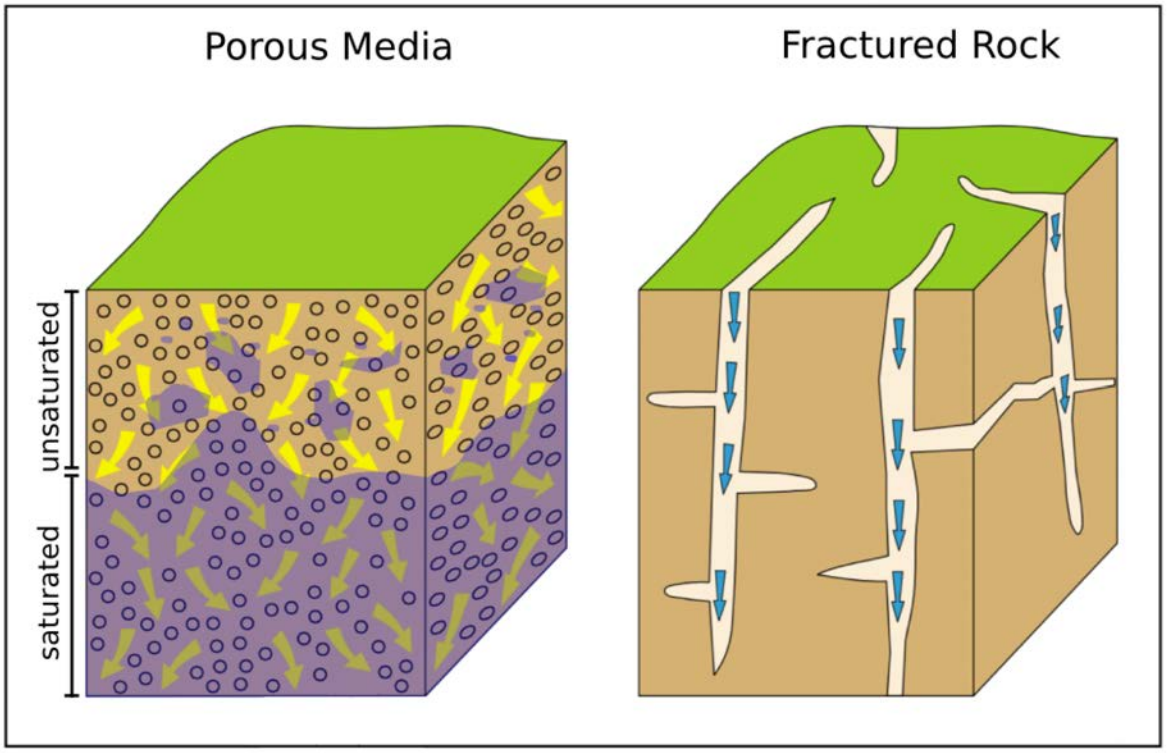

Figure 2.5: Various groundwater electrical models have been determined namely by media types in which the flow of ground water occurs: The porous media groundwater model, sub-categorised into the deeper saturated model relating to groundwater flow in unconfined aquifers, and the unsaturated model relating to vertical percolation of groundwater in the vadose zone towards the water table; and the fractured rock groundwater model, consisting of fractures where a majority of flow occurs, and the matrix acting as the storage reservoirs for these systems. Reworked from original figure by Love et al. (2001).

Two main sources and conceptual models of electrokinetic groundwater flow have been identified and described in literature.

Firstly, the unsaturated model which describes SP signals relating to vertical percolation of groundwater towards the water table (Jackson and Kauahikaua, 1987; Aubert and Atangana, 1996). Often referred to as the infiltration model, these conditions are mostly present in shallower unconsolidated, or consolidated vadose zone conditions. Few modeling studies of measured SP variations in unsaturated flow vadose zone conditions are available (Revil and Jardani, 2013; Adler et al., 1997; Darnet and Marquis, 2004).

Secondly, the deeper saturated water table model relating to groundwater flow in unconfined aquifers (Fournier, 1989; Revil and Jardani, 2013). In saturated conditions, the coupling coefficient of pressure (hydraulic head) and SP signals in both laboratory and field conditions has a well established quasi-linear relationship (Rizzo et al., 2004). The less predictable quasi element of the relationship can be attributed to several additional factors.

Sand-column drainage experiments in unsaturated conditions have highlighted predominant, non-monotonous and dynamic electrokinetic signal behavior at the onset of slow water flow and drainage. The effect appears to vanish to a quasi-static model with increasing drainage velocity. These results highlight fluid flow and water distribution at the pore scale have an important influence on SP response in unsaturated conditions (Allègre et al., 2010; Linde et al., 2007). Surface area and flow velocity across both negatively charged rock/water and water/air interfaces during the desaturation processes are thought to contribute to the non-monotonous behavior of the SP coefficient. When water saturation decreases, due to the additional quantity of water/air interfaces the SP coefficient can increase by approximately 10 to 40 times greater than previous (Allègre et al., 2015).

It is generally understood that additional influences of water pressure dynamics induced by capillary flow are present for streaming potential measurements in unsaturated conditions (Perrier and Morat, 2000)

2.2.1.2 Fractured rock

A majority of fractured rock aquifers are comprised of basalt, granite, metamorphics, shale, slate and some dolomites and limestones (Morton et al., 1998). The fractured rock aquifer systems consist of two major components: the fractures, and the matrix. Within fractures, which includes all faults, cracks and joints of varying length, is where a majority of groundwater flow in fractured rock aquifers occurs. The matrix principally act as the storage reservoirs for these systems (Revil et al., 2006)

Obtaining reliable groundwater supplies in fracture rock aquifers is complicated by irregular, unpredictable distributions of fractures. They are generally characterised by high spatial variability in hydraulic conductivity, and as a result can produce large spatial variations in bore yield (Krásnỳ and Sharp, 2007).

Traditional geophysical methods for estimating groundwater recharge and flow rate are not transferable to fractured rock aquifer systems (Roubinet et al., 2016a). Theoretical and experimental studies have shown that changes in permeability and flow rate can be attributed mainly to three factors: changes in mean aperture; changes in roughness; and changes in contact area (Huo and Benson, 2015). Flow rate increases dramatically as the width (or aperture) of the fracture increases. Doubling width of an aperture can increase flow rate by up to a factor of eight (Snow, 1968).

Fluid flow through transmissive fractures or fracture zones generate azimuthal SP signal variations related to preferential flow directions and flow rates (Wishart et al., 2006).

Several laboratory and field studies have utilised the SP method to detect and correlate anomalous signal magnitude with aquifer fracture frequency (Suski et al., 2008; Wishart et al., 2008; DesRoches et al., 2017). In recent work, Roubinet et al. (2016a) discussed that fluid flow must occur through both an aquifers fractures and rock matrix, and not fractures alone, for the resulting SP anomalies to be of detectable magnitude at the Earths surface.

2.2.1.3 Combined models and shallow zone effects

Field sites will often be a mixed interaction of the two overarching groundwater flow models (saturated and unsaturated). Field site geology will generally consist of an unsaturated overlying vadose zone, including unconsolidated soils and consolidated rocks, and a saturated permeable aquifer.

Even if groundwater flow is only stimulated in the lower saturated aquifer, constant various hydrogeological interactions can still be present in the shallower vadose zone. Electrical daily variations can be induced by factors including: the soil water flux (Thony et al., 1997); and more general capillary flows in the non-saturated zone (Perrier and Morat, 2000).

The detectable presence and amplitude of each models individual or combined electrokinetic signals at the surface is dependent on several factors, but can be mainly attributed to both the groundwater flow source depth and a sites overall geological features.

2.2.2 Additional phenomena

2.2.2.1 Rapid fluid-rock or fluid-gas interactions

Recorded deviations of more than 10 mV potential difference, in laboratory and field conditions respectively, have been attributed to rapid fluid rock or fluid gas interactions (Stumm and Morgan, 2012). These interactions are typical of non-saturated field conditions, occurring during drainage when a non-wetting fluid displaces a wetting fluid.

Similar electrical burst signatures, defined as Haines jump electrical disturbances, are documented in saturated sandbox laboratory drainage experiments (Figure 2.6). These pore scale drainage, high frequency electrical events are attributed to pore-water meniscus displacements (Haas and Revil, 2009; Revil et al., 2012; Bultreys et al., 2015).

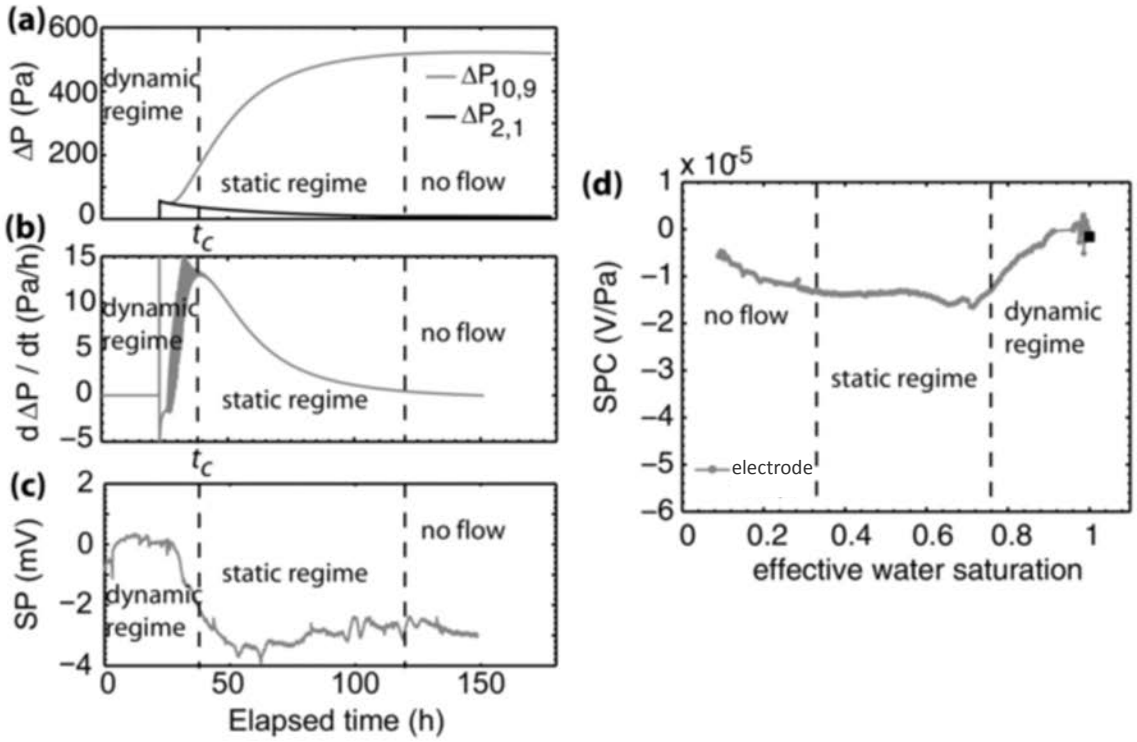

Figure 2.6: A sandbox experiment observing passive electrical burst disturbances using highly sensitive electrodes during drainage. Dashed lines separate static and dynamic domain conditions: (a) Computed total water pressure differences ΔP , (b) first time derivative ΔP , (c) measured streaming potential , and (d) measured streaming potential coefficient for an experimental dipole. These SP events were only observed during imbibition or drainage, not prior to or after the fluid flow inside the porous sandbox (Haas and Revil, 2009).

2.2.2.2 Redox stability

Poor reproducibility and fluctuations in redox anomalies are caused by shifts in the chemical system constantly re-establishing equilibrium, known as polarisation of the potential. Laboratory condition and field survey experiments highlight that the polarisation of a redox system can be significant.

The constant drift of a redox potential will remain low if concentration of the redox-active ions is high (Stumm and Morgan, 2012). Generally, SP measurements should be given ample time (time length dependent on conditions eg. rainfall) at a position to obtain a stable, more reliable insight to the redox equilibrium.

2.2.2.3 Telluric currents

Additional noise sources when conducting SP measurements result from telluric currents due to external magnetic field changes (Corwin, 1989; Petiau, 2000; Perrier and Pant, 2005). As telluric currents are continually changing, its effects can be difficult to identify and mitigate. The use of pattern filtration must be considered and intelligently applied to SP datasets which exhibit these telluric features. High frequency telluric waves can be readily detected and removed using simple, low-pass filtration techniques (Rizzo et al., 2004).

2.2.3 Field-site consideration and instrumentation

In field conditions, many undesirable electrical phenomena are concurrently at play. Differentiating these sources is a difficult task, and the signal to noise strength (or ratio) is a commonly termed comparison of these desired versus undesired electrical signals present (Revil et al., 2008).

2.2.3.1 Petrophysical factors

Petrophysical factors which affect a laboratory sample's zeta potential at micro-scale, are also significant when determining the suitability of a macro scale field site. Overall subsurface conductivity and the geological structures of a field site are critical factors in determining the capable surface expression of a SP signal.

When possible, preliminary investigations for a field sites suitability to SP methods should begin by or include a synthetic site model survey. A synthetic model is constructed from known key parameters including a sites conductivity, permeability, and expected groundwater flow rates. To develop models, physics workspace simulation tools such as *COMSOL Multiphysics* are often used in conjunction with prominent groundwater approaches. In Figure 2.7, developed using the COMSOL Multiphysics package and following the approach of Sill (1983), two models (M1 and M2) are presented for preliminary investigations of a horizontal coal seam site within the Surat Basin, Queensland, Australia. The two models are differentiated only by a change in conductivity of the horizontal coal seam from 5 Ω m to 50 Ω m at a depth of 500 m. This conductivity change alone causes an increase in the surface detectable electrokinetic signal to

10 times that of the original model (M1 5 Ω m) during active groundwater pumping.

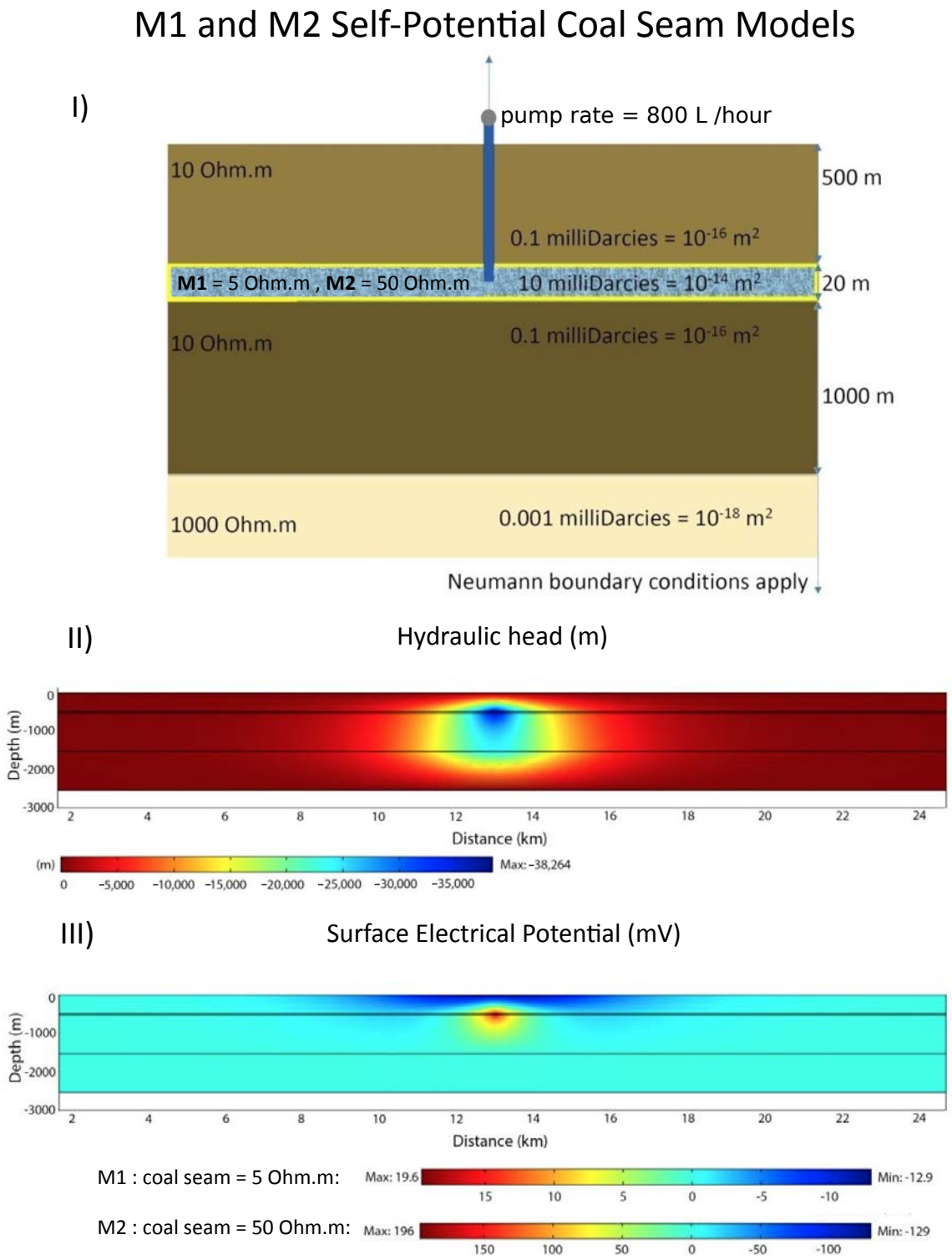

Figure 2.7: Two models, M1 and M2, are presented as a preliminary investigation of a theoretical horizontally bedded coal seam site within the Surat Basin, Queensland, Australia. The two models differ only by a change in conductivity of the coal seam from 5 Ω m to 50 Ω m, resulting in a surface detectable electrokinetic signals of 12.9 mV and 129 mV respectively. Models were constructed utulising the COMSOL Multiphysics package.

The heterogeneous nature of these petrophysical factors must also be considered when planning or analysing self-potential survey results, in particularly the varying conductivity of the subsurface. Additional physical surface factors can also include unique lithology, chemistry, and compaction conditions (Ernstson and Scherer, 1986; Revil et al., 2006; Khesin et al., 2013), the presence of organics, and microbial electrical contributions (Slater and Atekwana, 2013).

Environmental conditions can greatly impact SP recording instruments and electrodes, therefore it is important to understand how this can affect overall survey results. More significantly impacting environmental variables include: magnetics, temperature, humidity, rainfall, (Ernstson and Scherer, 1986; Perrier et al., 1998; Perrier and Morat, 2000; Darnet and Marquis, 2004; Revil et al., 2006), tidal influence (MacAllister et al., 2016), and atmospheric pressure (Adler et al., 1997). Depending on time length, several of these environmental factors can be dynamic throughout the survey. Data filtering must be considered to minimise or remove the influence of environmental noise, particularly in surveys across medium to long time periods (hours to days).

Anthropogenic noise must be considered, especially in areas of high human activity. Amplitudes and interaction in SP measurements is variable, and again data processing techniques must be considered and applied if required (Corwin and Hoover, 1979; Perrier et al., 1998).

2.2.3.2 Electrodes

When conducting SP monitoring operations, the main possible measurement errors arise from electrode instability (Jougnot and Linde, 2013). Causes of this can include drying and increased contact resistance between electrode and soil, or degradation and chemical contamination including diffusion of salts between inside of the electrode and the outside soil medium. Petiau (2000) nonpolarizable style electrodes are used to reduce these effects, and are believed to be stable for monitoring operations over several years.

A contact resistance is always present between an electrode and a given medium. High electrode contact resistances within field conditions are generally caused by very low levels of soil moisture, for example in soils

with a low clay content. If required, water or clay can be added to bond an electrode to its medium and ensure a lower contact resistance is achieved (Inverarity, 2014).

It is suggested by Revil et al. (2012) that contact resistances should not exceed one-tenth of the input impedance of the voltmeter being used. Higher contact resistances cause leakage currents in the voltmeter, which then degrade the accuracy of the potential measurement.

2.3 Self-potential in groundwater exploration

Works by Fitterman (1978, 1979) developed integral equations which were used to derive electrical and magnetic fields associated with non-equilibrium conditions. Soon after, pairing these works with generalized Darcy and Ohm coupled laws, Sill (1983) quantified the self-potential signals associated with the flow of ground water.

2.3.1 Methods for groundwater surveys

Performing the SP method is simple, inexpensive and safe, as it requires no addition of an electrical current to the Earth. They are considered a standard method to assess the hydraulic transmissivity and storativity of aquifers (Butler and Zhan, 2004; Suski et al., 2006).

A self-potential monitoring logger is principally a high sensitivity (at least 0.1 mV) and high input impedance (typically 10-100 MΩ) voltmeter (Revil et al., 2012). Measurements by the logger are performed using non-polarizing electrodes (Petiau, 2000). Loggers record the electrical difference between a number of surface electrodes situated at the pumping target, and a reference electrode (or grounding probe), typically some distance (100 – 1000 meters) from the target. The reference electrode method provides a fixed base signal to monitor changes in electrical potential signal as a result of pumping causing streaming potential activity. Choice of location for a reference station is extremely important: great care should be taken to ensure the absence of electrical noise around a reference station (Revil et al., 2003). It is also preferable to keep measurement and reference electrodes within consistent/unchanging lithological and bedrock geology conditions.

Various arrangements of surface electrode arrays can be used to specifically suit surveys needs, or cater to topographic or geological conditions. Examples of SP survey array styles for pump tests include radial arms surrounding a central pumping point, or a boxed grid style that is more generally adaptable to compliment additional geophysical datasets. Spacing of observation arrays in pump testing is dependent on the expected zone of pumping influence determined by previously discussed factors, and resolution. This can generally range from anywhere between 1 m to 25 m.

Additional styles of SP surveying not specific to pump testing includes straight line observations along or across strike of a bedrock, or 'hot spot' observations at specific points of interest.

2.3.2 Self-potential instrumentation

2.3.2.1 Setup

The University of Adelaide commissioned the construction of four SP field instruments. The SP loggers were designed to measure voltage difference between two points separated by some distance. At each point in space, using electrodes we can effectively measure the following:

$$\Delta V = (V_{SP}^{Electrode\#} - V_{SP}^{Reference}) + E_{induced} \cdot \Delta x \tag{2.5}$$

where $E_{induced}$ is the induced electric field, and Δx the distance between the measuring electrode and its reference.

2.3.2.2 Electrical resolution of instrument

A series of electrical tests were conducted to trial and test components of, and the overall electrical clarity of the loggers. These tests were designed to resolve the instruments minimum and maximum electrical noise window.

A Datataker model DT85 (DataTaker Intelligent data loggers website, 2018) was used as the SP instruments analogue signal receiver and recorder. As the Datataker unit is equipped with an internal self-test calibration function, further controlled testing was undergone primarily to ensure additional electrical components within the SP instrument, particularly the AC power supply and DC to AC converter, had not introduced any measurable electrical noise signal.

A custom-made, low-resistance wiring set-up was produced to connect the SP loggers analogue channels directly to required electrical testing instruments. Using this set-up, the Datataker's analogue channels were connected to a stable electrical potential difference signal of 15 mV via a battery and resistor configuration. Measurements and recordings were conducted every one second, for a minimum of 10 hours.

Results from the best performing SP logger were as follows. A total number of 75,045 observations (~ 21 hours) were recorded. Of the 900,540 samples collected (75045 x 12 channels), fewer than 30 samples recorded incorrect values of 14.9 mV (a - 0.1 mV difference). This calculates to a 0.0033 % margin of error over the 21 hour testing period. All four of the SP instruments performed this test with a margin of error falling below 0.005 %.

2.3.2.3 Electrode wiring clarity

To connect the SP instruments to field electrodes, seismic geophone instrument connection lines were refurbished and repurposed. Each line comprised of 24 individually insulated copper wires (12 to electrode connection points, 12 additional points for extending the line) sealed in a heavy-duty, insulated plastic outer casing. Each line measured 130 m in length.

Laboratory testing was conducted on the lines to ensure conducting properties of the refurbished seismic lines had not been compromised. Potential causes of compromise include electrical wire degradation or oxidation over time, or connection and soldering issues at either the newly installed military connector head (cable to instrument connection head) or electrode breakouts along the line.

For this experiment, 12 electrodes were submerged in a fine silica sand and saline water sandbox. Using all 24 of the SP loggers available analogue channels, each of the 12 electrodes were simultaneously connected to the SP logger to check that the wiring polarity was correct.

Examples of this experiments dual signal analysis, and overall comparison of the recorded signals can be seen in Figure 2.8. From the histogram it can be seen that electrical signal difference of the two wiring variables most commonly fell within -0.05 mV and 0 mV. This range of difference can

therefore be considered the overall electrical noise window that is directly attributable to the SP loggers field wiring.

Whilst some electrical loss and general error of difference was observed during the experiment, this small difference can be considered unlikely to alter a surveys outcome and therefore regarded as of negligible influence.

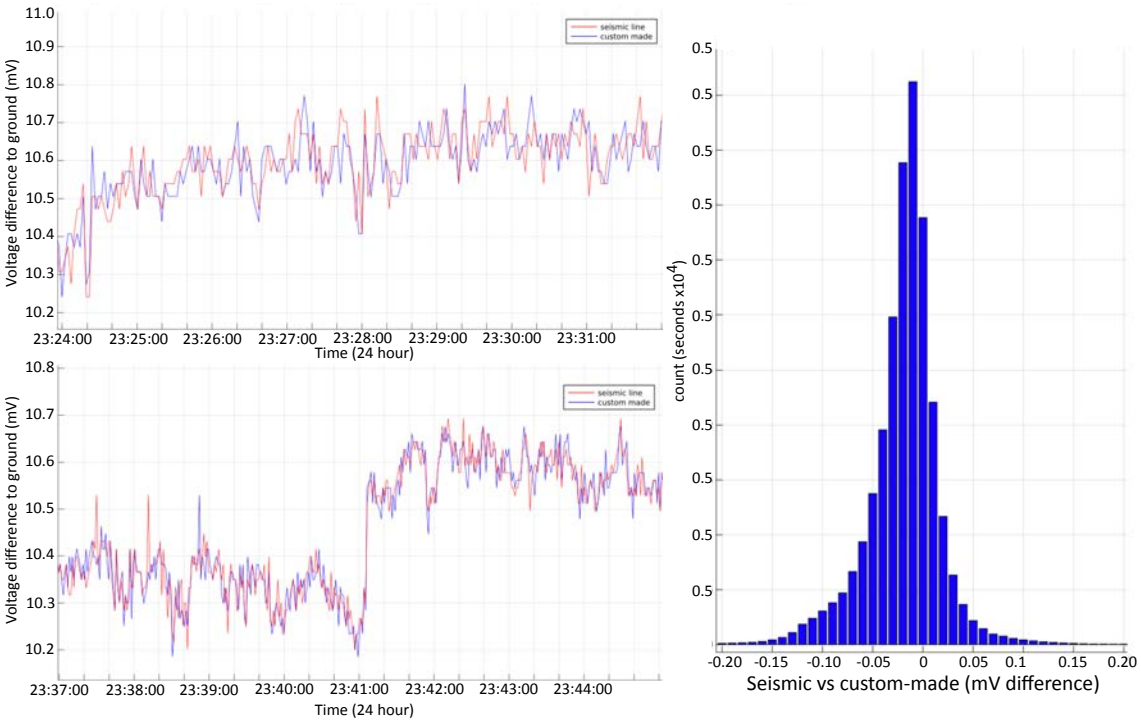

Figure 2.8: Laboratory testing of newly constructed SP logger field wire lines (repurposed seismic lines). 12 electrodes, submerged in a fine silica sand and saline water sandbox, were each simultaneously connected to two SP logger analogue channels via both the newly constructed field line (seismic), and a previously tested noise free line (custom made). With the electrode line connection serving as the experimental independent variable, a comparison of the two resulting electrical signals could be made. Left: Comparisons of the resulting electrical signal at random points in time; and right: A histogram summarising signal difference (custom-made signal minus seismic signal) at each one second measurement (in mV difference) between the two discussed variables.

2.3.2.4 Electrode resolution

In electrical geophysics, it is considered common practice to record all surface and down hole measurements using non-polarizing electrodes (Revil et al., 2006). There are many forms of non-polarizing electrodes comprised

of various casing and inorganic compound setups; the current gold standard in non-polarizing electrodes is the second generation Petiau lead-lead Chloride (Pb-PbCl2)(Petiau, 2000). Although considered to require only low-maintenance, they are relatively expensive, heavy in weight and must be kept upright, and still experience a slow degradation over time.

It is not uncommon for industry electrical geophysics to utilise metallic alloy rods for the recording of observations. Although these alloy rods are subject to polarization effects, rusting and therefore degradation, they are inexpensive, lightweight, rapid to set-up and require no maintenance. The advantages they pose to a survey crew can far outweigh polarization issues, which can be largely corrected for during post-processing.

To test the commercial viability of these alternative low-cost electrodes, 10 various types of alloy metal electrodes were chosen and compared against a research leading Petiau style lead-lead chloride electrode. The electrodes were purchased from several geophysical suppliers, and were all of greatly varied styles and material compositions. The electrodes were ranged within lengths of approximately 15cm to 50cm, and diameters of approximately 1cm to 2.5cm.

For the experiment, a total of 20 electrodes (10 varied types of electrodes in pairs) were connected to an SP logger, and submerged in a controlled sandbox experiment containing fine silica sand fully saturated with saline water. The experiment was conducted for a total duration of two days. The alloy electrodes were compared to the Petiau style electrodes for both general signal stability and drifting properties. From the initial 10 tested, two metallic electrode signals were considered as comparable to that of the Petiau style electrode - an iron based alloy electrode with zinc galvanizing, and a non-galvanized high grade stainless steel alloy electrode. A comparison of these three electrodes can be seen in Figure 2.9. It is probable these specific metallic electrode types (galvanised and high grade stainless steel) signals were stable and comparable with that of the Petiau electrode due to their oxidation resistant materials.

An additional testing period in Figure 2.10 shows the continually comparable signal of the two alloy electrodes, and the Petiau style electrode. For means of researching a commercially viable and cost effective substitute to

the Petiau style electrode, an alloy electrode was used for groundwater experiments in the Balhannah fractured rock aquifer setting (see Chapter 4). The iron alloy, zinc galvanised electrode was selected over the stainless steel electrode, due to its lower cost.

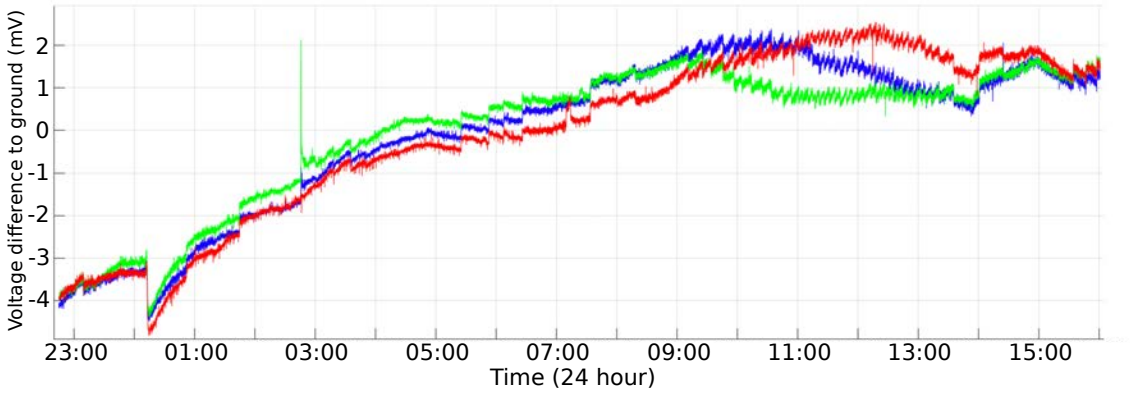

Figure 2.9: A controlled fully saturated laboratory sandbox experiment comparing three electrode types for their signal stability and drifting qualities. Metal electrodes, including an iron alloy, zinc galvanised electrode (red) and a high grade stainless-steel electrode (green), are compared to a lead-lead chloride Petiau style electrode (blue). Petiau style electrodes are non-polarizing and overall considered highly suitable to the requirements of field geophysics. Alternatively, metal based electrodes are low-cost, low-maintenance and faster to setup. The sandbox experiment presents the three electrodes to have a comparable electrical signal. The comparable signal is likely due to the oxidation resistant material properties of both zinc-galvanization and stainless-steel.

A secondary laboratory sandbox experiment was conducted, shown in Figure 2.10, utulising the same sandbox experiment setup as previously described. This secondary testing phase was comprised of nine iron alloy, zinc galvanised electrodes, and three lead-lead Petiau style electrodes. This additional sandbox experiment was to ensure there was no obvious widespread variation in electrical signal quality of the selected iron alloy electrodes. Potential variations among the same material electrodes can be caused by impurities or inconsistencies present in either the alloy or its galvanised exterior. Some iron alloy electrodes did infact exhibit a larger amount of drift than others. The largest drift exhibited was 10 mV over the 15 hour period

Drift effects were noticeable across both electrodes but were more prominent in the iron alloy electrodes, drifting on average at approximately 0.2 mV per hour. All three Petiau style electrodes are relatively stabalised after 5 hours, and from this time do not exhibit any obvious linear long term polarisation noise characteristics.

As one would have assumed previous to this experiment, polarization effects were more prominent in the iron alloy, zinc galvanised electrodes when compared against the Petiau style lead-lead chloride electrodes. As these effects were both linear and considered of low amplitude, and taking into account part of the experimental scope was to trial a form of low-cost, low-maintenance and fast set-up electrode for industry SP processes, the iron alloy, zinc galvanised electrodes were selected as an acceptable substitute to the industry's standardised Petiau electrode.

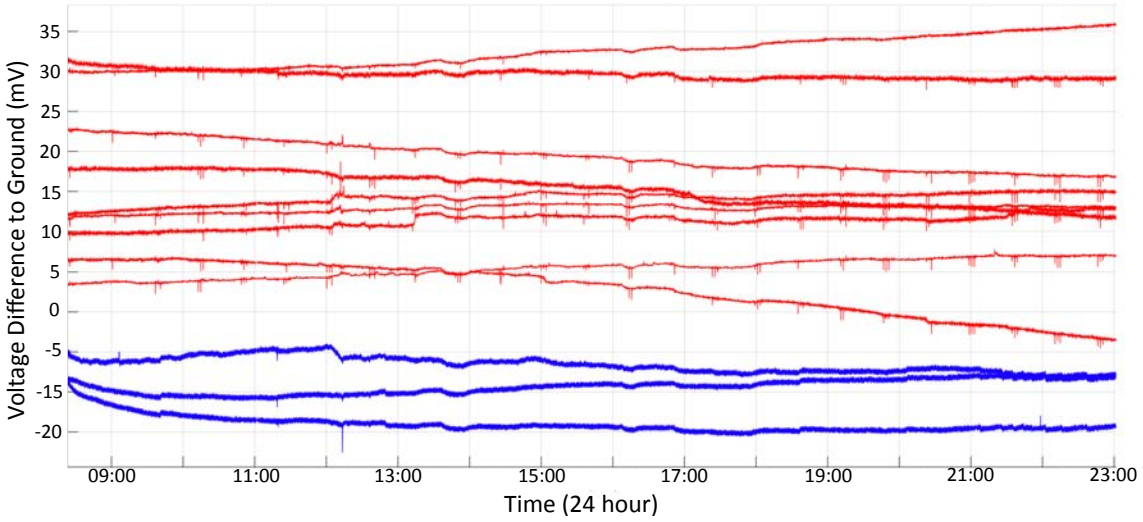

Figure 2.10: A controlled laboratory sandbox experiment comparing a total of nine iron alloy, zinc galvanised electrodes (red) with three lead-lead chloride Petiau style electrodes (blue). Long term linear drifting effects are more prominent in the iron alloy electrodes drifting at approximately 0.2 mV per hour. Petiau style electrodes are relatively free of linear drift effects after approximately five hours. As the best of 10 previously trialled alloy electrodes, and taking into consideration the original experimental scope for trialling low-cost, low-maintenance and fast set-up electrodes, the iron alloy, zinc galvanised electrodes will be used as a substitute to the industry's standardised Petiau electrodes in a field research trial.

2.3.3 Processing, tomography and inversion

It has been long established that if subsurface pressure distribution is identified during a pump test, inverse groundwater modelling can determine the distribution of the hydraulic conductivity and storativity around a borehole (Cooley, 1977; Neuman et al., 1980; Yeh and Yoon, 1981; Kitanidis, 1986; Loaiciga and Mariño, 1987). An aquifers piezometric surface is generally not well constrained due to a lack of observation wells, which are both costly and can be disruptive to hydraulic head distribution. Due to this required bridging in hydrogeological information, the self-potential method has been preferred as a nondestructive, cheap method for determining the shape of the piezometric surface (Revil et al., 2003). Over the last 15 years, there is a considerable reawakening interest in the application of electrokinetic phenomena in geohydrology. A major refocusing of SP surveying has gradually advanced the method from a quantitative complementary geophysical technique, into a sophisticated quantitative modelling technique across a broad range of applications (Revil et al., 2006).

Several approaches to field signal analysis, including more recent tomographic (Mao et al., 2013; Brauchler et al., 2013; Straface et al., 2010) and inversion algorithms (Soueid Ahmed et al., 2014; Revil, 2016; Soueid Ahmed et al., 2013) have aided in growth and versatility of the self-potential technique. Although different in application, the problems are governed by an elliptic partial differential equation involving measurement of a potential field interpreted directly in data-space (tomography), or inverted to determine a source model which incorporates underlying physics of the problem. Examples of some synthetic SP profiles and their sources spatial characteristics can be seen in Figure 2.11.

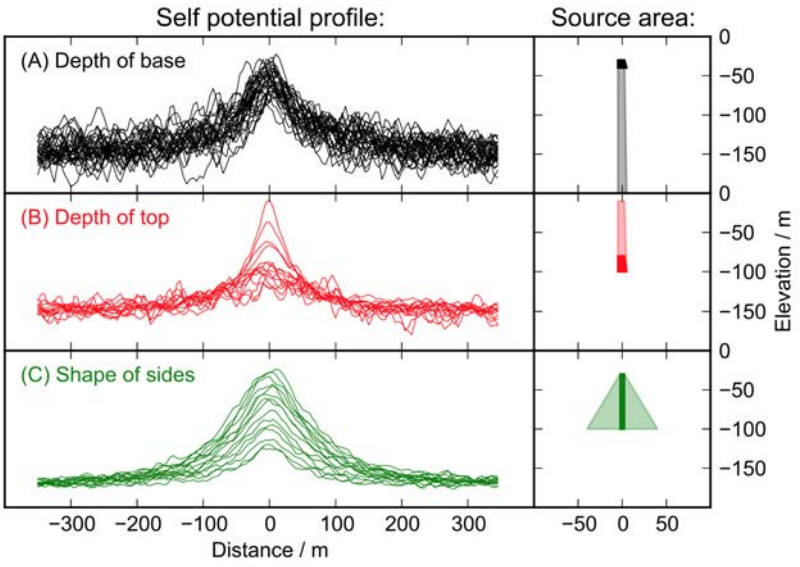

Figure 2.11: Characteristics of a forward-modeled self-potential signal profile sensitive to variations in the geometry of a signal source area, including I) the depth to the base of a source, II) the depth to the top of a source area, and III) the dip of a source zone's sides. A Gaussian noise of 2% was added to each self-potential signal and then stacked. Figure from Inverarity (2014).

As a form of field mapping, acquired field measurements would be used to produce a distance (x) to signal (y) graph where contrasting anomalous signal behavior could be spatially detected. An example of this style of mapping can be seen in Figure 2.12. These visualisations still remain prominent in the field as a trusted and simplified method of feature visualisation, but only for a few simple charge geometries can numerical estimates of the source parameters be directly derived from analysis of field SP profiles (Fitterman and Corwin, 1982; Murty and Haricharan, 1985; Patella, 1997a).

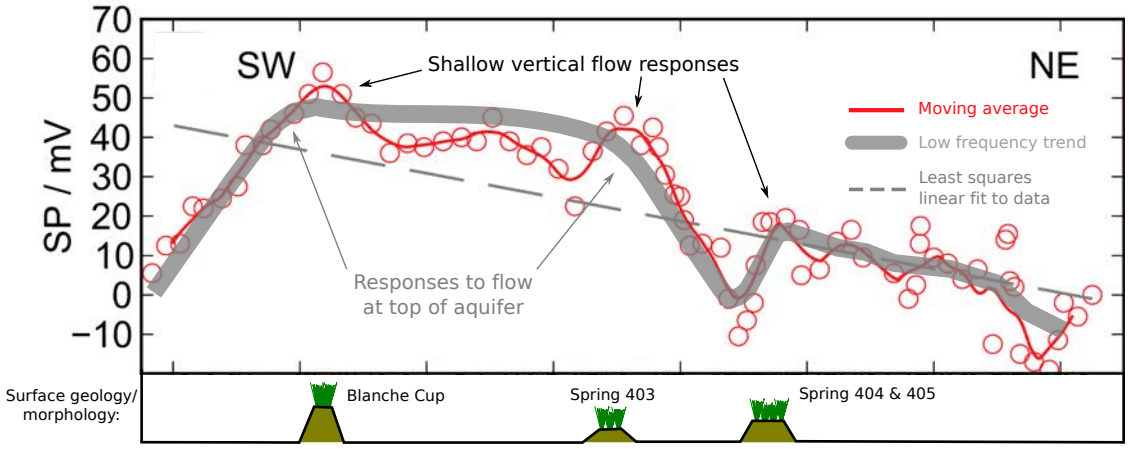

Figure 2.12: Hydrogeology of the Bubbler Spring Complex, Lake Eyre Region, South Australia. Collected SP data conferring with surface morphology, caused by shallow vertical flow responses of springs (black arrows). Flow in a shallower top aquifer (100m depth) results in an increased surface response (grey arrows). Reworked from Inverarity (2014).

Moreau et al. (1999) conceptualised the use of the continuous wavelet transform to analyze potential fields and locate their causative sources. The analysis can estimate parameters of a source including its horizontal location, depth, multipolar nature and strength. The wavelet transform can provide a local analysis of the measured field contrary to the global Fourier transform, and the inherent ability to correctly handle noise present in the data (Hornby et al., 1999). Its application to spatial SP profiles in Figure 2.13 was introduced by Gibert and Pessel (2001), and are still used extensively (Saracco et al., 2004; Mauri et al., 2010).

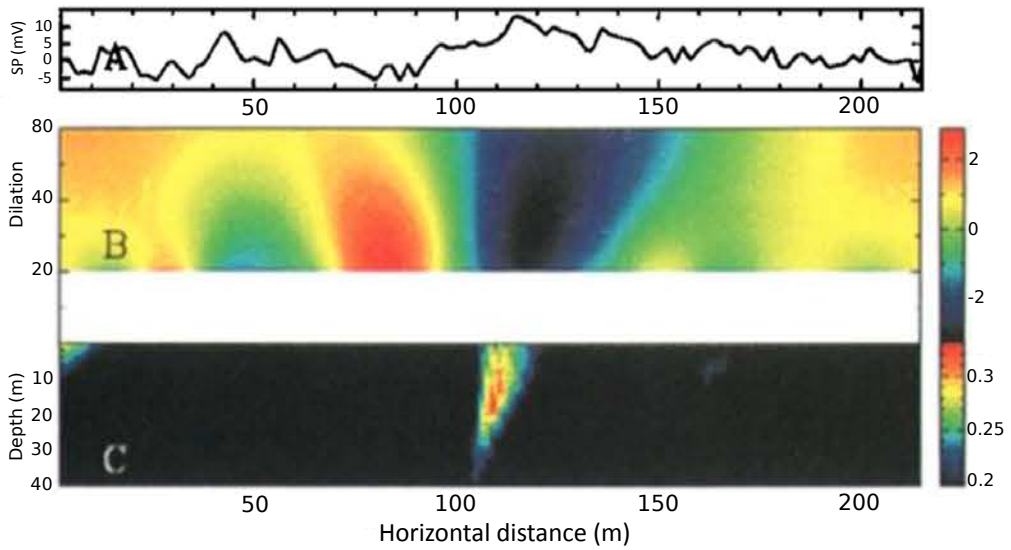

Figure 2.13: Identification of sources of potential fields with the continuous wavelet transform. A) surface SP response running perpendicular to a volcanic dyke fault (located at approximately x= 100m) in Pont-Péan, France. B) Continuous wavelet transform of the data. C) From the continuous wavelet transform, the most likely position of the detected current sources. Figure from Gibert and Pessel (2001).

Higher precision and sampling rate field instrumentation, and more powerful computing capabilities gave rise to development of newer tomographic methods. A new approach to SP anomaly interpretation was developed by Patella (1997b) where imaging of a section (2D) or space (3D) is defined as a probability function of electric charge distributions. This style of self-potential tomography algorithm can be referred to as a charge occurrence probability function, but is more generally known as a scanning function. It is an algebraic function independent of any unknown strength coefficient and containing only source location coordinates (Patella, 1997b).

The algebraic framework of Patella (1997b) SP scanning function was reworked by various authors (Hämmann et al., 1997; Sailhac et al., 2004; Gibert and Pessel, 2001; Iuliano et al., 2002) incorporating uses of alternative properties that could define a spatial point's source correlation coefficient. A relatively simple method of the Patella framework reconstructing

images of the most likely location of self-potential sources is outlined by Hämmann et al. (1997).

Non-forward methods are still commonly used in SP analysis, particularly when a definitive prior knowledge of a field domain information is unknown. Data and information obtainable includes the shape and number of potential source charges, relative depth range, and multipolar nature of a source (Gibert and Pessel, 2001). Results can also be used as a prior model for more sophisticated or joint inversion methods (Patella, 1997a; Lapenna et al., 2000).

A simplified semi-empirical approach was developed by Revil et al. (2003) (Figure 2.14) based on previous works by Fournier (1989) to investigate SP signals associated with the piezometric surface of an unconfined aquifer. The technique can be used to estimate spatial variability in drawdown during pumping, and subsequently lateral variations in hydraulic properties of an aquifer. It showed that in the simple case of steady state pumping in homogeneous, unconfined aquifers, surface variations in SP should be proportional to drawdown of the water table below the electrode.

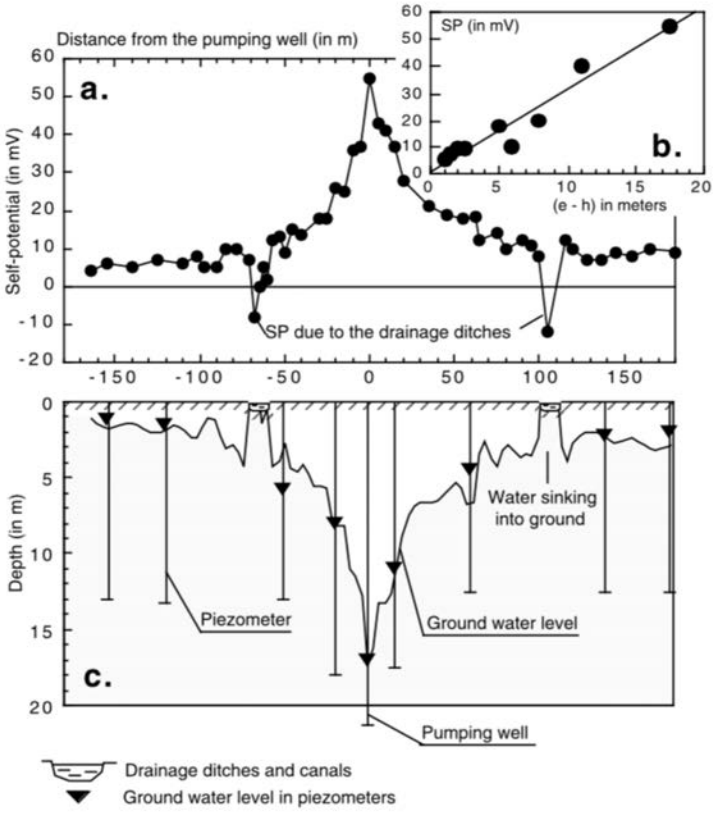

Figure 2.14: Self-potential signals associated with groundwater flow at a pumping well, with data sourced from Bogoslovsky and Ogilvy (1973). *a)* A surface SP anomaly, with central point $x = 0$ corresponding to the investigated pumping well. *b)* The relationship between surface SP signal and true depth of the water table, for each of 9 downhole piezometers. *c)* Piezometer readings (solid triangles) of the actual water table depth, and the interpreted water table (solid line) using a semiempirical approach developed by Revil et al. (2003). Original figure from Revil et al. (2003).

Inversion techniques are considered to provide the highest probability of producing the most useful images of underground SP sources. By inversion, a trial-and-error procedure is required that operates to minimize differences between real observed self-potential and pre-modelled self-potential data obtained for specific model parameters (Tarantola and Valette, 1982).

In recent times, solving of the forward problem specific to SP has allowed for the inversion of SP profiles (Jardani et al., 2007, 2008, 2009; Soueid Ahmed et al., 2013, 2014; Ahmed et al., 2016). For this, it is necessary to account for both the various sources of current density corre-

sponding to different mechanisms of polarization (eg. streaming potential and redox potentials), and the distribution of the electrical conductivity of the system. For streaming potentials, the hydraulic problem can be solved first (Sill, 1983) and its solution used to compute the sources of current, and then the distribution of the electric field. This process is mapped in Figure 2.15 from works by Soueid Ahmed et al. (2013) on the streaming potential inversion process 'SP2DINV'.

The principal limitation to these inversion methods concerns the inclusion of electrical resistivity data from additionally performed geophysical methods, including induced polarisation, or electrical resistivity tomography (Revil et al., 2006).

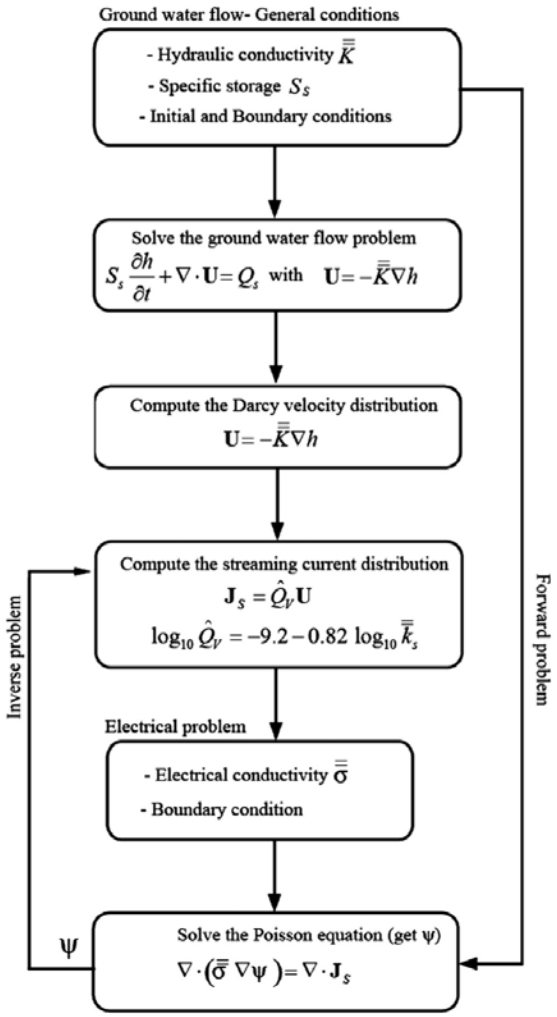

Figure 2.15: Flowchart for simulation and inversion of SP data that is associated with groundwater flow. In saturated conditions, the required inputs for the forward modeling are hydraulic conductivity, electrical conductivity tensors and specific storage coefficient. $\mathbf{U}$ = Darcy velocity , J_s = source current density, h = hydraulic head, and ψ = electrical potential. Figure from Soueid Ahmed et al. (2013).

CHAPTER

THREE

FRACTURED ROCK AQUIFER 1: WATERVALE

3.1 Aim

Characterization of directional flow paths within a fractured rock aquifer provides significant insight regarding the effective utilisation of groundwater regions groundwater resources. Considering SP method techniques are both fast and low in cost, the quantitative or qualitative groundwater flow information it provides can be invaluable for the determination of future well locations and their required depths. SP methods have previously shown a great deal of success at mapping the flow of groundwater in homogeneous, isotropic media type settings (Rizzo et al., 2004; Jaafar et al., 2009; Soueid Ahmed et al., 2014; Ahmed et al., 2016). However, within heterogeneous fractured rock aquifers, both the successful delineation of preferential fluid pathways, and reliable quantification of aquifer properties such as permeability, has continued to be problematic (Roubinet et al., 2016b).

A groundwater pumping and surface SP survey investigation was conducted during September 2015 at a groundwater research site in Watervale, Clare Valley, South Australia. The principal aim was to locate and delineate directional groundwater flow within the fractured rock aquifer towards the pumping well during pumping, utilising only the surface SP method. Correlating the observation wells hydraulic head fluctuations with

detectable surface SP electrical anomalies provides a measure of how well the SP technique can be used to map groundwater flow.

3.2 Background

3.2.1 Site description

Watervale is situated in the Clare Valley, within the northern Mount Lofty Ranges and approximately 100 km north of Adelaide, South Australia. The region has a globally recognised reputation for production of premium quality grapes and wines. The Clare Valley region makes for an appropriate groundwater testing site, as its expanding viticultural industry requires increasing amounts of water for reliable irrigation, from both surface and underground resources. The Clare Valley is not a singular valley, but rather a number of valleys and small catchments sub-divided by a series of ridges. The numerous valleys and ridges can be attributed to neo-tectonic activity.

The Climate can be described by hot, dry summers daily averaging 30°, and cool to cold, moist winters daily averaging 14°. Mean annual rainfall is 653 mm at Watervale; there are no surface perennial streams, and flow within catchment watercourses generally occurs for less than half of the year.

3.2.2 Geology

The Clare Valley and Watervale location in Figure 3.1 forms part of the larger Adelaide geosyncline, an exposed failed continental rift valley (Love et al., 2001). Tectonism during the Cambro-Ordovician Delemerian Orogeny caused folding and faulting, also subjecting the original sediments to low-grade metamorphism (Preiss, 1987; Foden et al., 2006). A second period of tectonic activity occurred during the Tertiary period, resulting in further uplift and rejuvenation of earlier tectonic features (Love et al., 2001).

The Clare Valley is a syncline (Figure 3.1), with its fold axis in the north-south direction. The western limb of the fold is overturned with bedding planes dipping more than 90°, and the eastern limb of the fold dips only mildly. It is bounded to the west by a north-northwest trending fault ridge, elevated at approximately 400m.

The region consists predominantly of Neo-proterozoic rocks of the Burra and overlying Umberatana Groups (650–780 Ma). Low-grade metamorphism of the bedrock resulted in new mineral growths, and an overall reduction of porosity. Rock types within the area consist primarily of shale, siltstone, dolomite and quartzite (Morton et al., 1998).

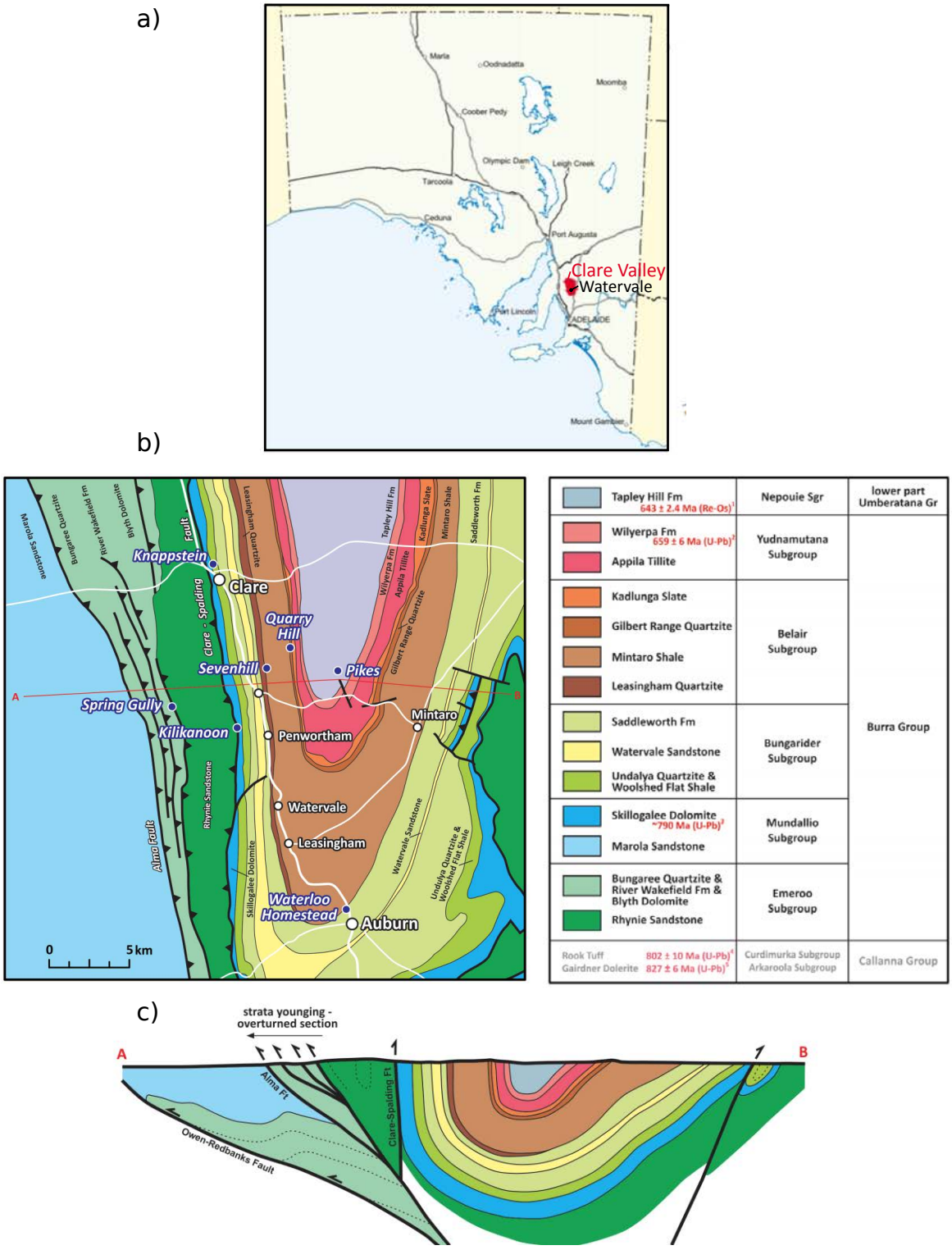

Figure 3.1: *a*) Location map of the Clare Valley Catchment region (red) and research area Watervale, South Australia (black) (modified from Love et al. (2001)) *b*) A generalised geological map and stratigraphy of the Clare Valley region. *c*) A schematic cross- of the Clare Valley area between points A and B (presented in *b*). (Original figure by Preiss (2006)).

3.2.3 Groundwater

Two main aquifers exist within the Clare Valley; minor alluvial/colluvial porous rock aquifers to the north of Clare, and substantial fractured rock aquifers through the remainder of the region. Fracturing in the region is considered to be ubiquitous and groundwater can flow across the Clare Valley hydrogeologic units. Subsequently, variations in wells groundwater yield is likely a result of fracturing or other structural constrains, and is generally independent of rock type.

Groundwater well yields can vary from less than 0.1 L/s, and upwards of 25 L/s, dependent purely on characteristics of the accessed fractures. Figure 3.2 shows well yield for all wells across the Clare Valley as a function of depth. There is no understood association between high well yields and locality, and rock type. Previously high yield bores on occasion have become dry; reasoning for these sporadic permanent recharge failures are unknown. Groundwater salinity varies considerably from less than 500 mg/L, to in excess of 7000 mg/L. Lower salinity and higher irrigation quality groundwater is associated with the higher rainfall and therefore superior recharge zones in the Watervale area.

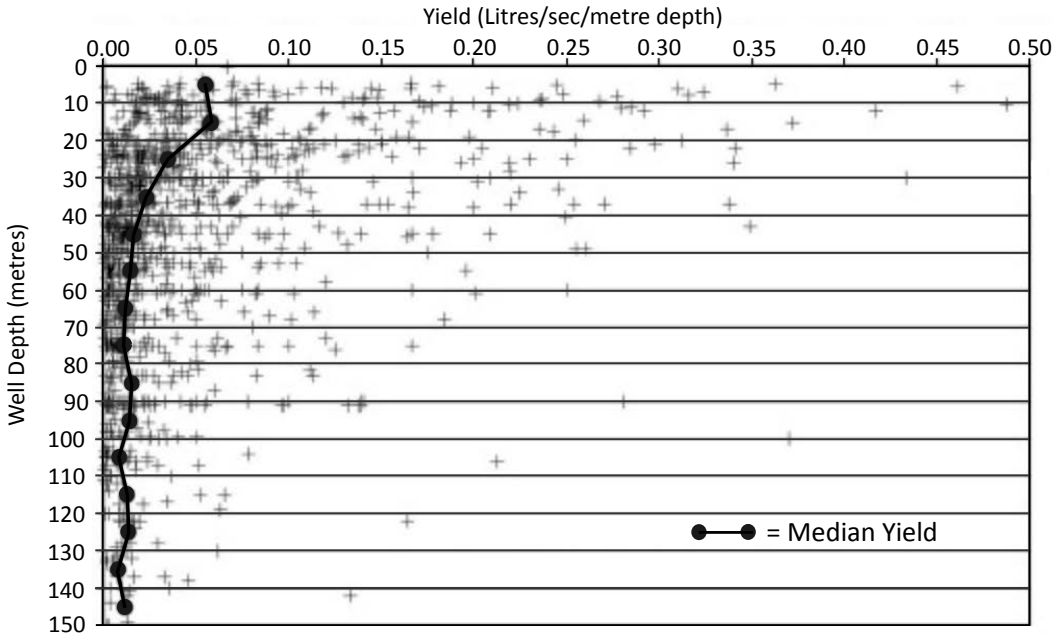

Figure 3.2: A graph of the Clare Valley catchment zones median borehole groundwater yield. Each of the wells groundwater yield measurements (n=1315) were normalised by the total depth of the well (x-axis), and plotted as a function of the wells overall depth (y-axis). Solid circles represent the calculated median yield per 10 m depth. Note that weathered to fresh rock transition across the Clare Valley catchment occurs generally at above 20 m depth below surface. Data from **?**, and original figure reworked from Mortimer et al. (2011).

3.3 Field survey

A surface array of 48 electrodes were used to measure changes to the electrical potential field (in mV diference to ground) as a result of groundwater pumping at the Watervale site. A graphical representation of the Watervale sites configuration can be viewed in Figure 3.3.

The array was comprised of four straight radial arm electrode lines that adjoined the main pumping well to four surrounding observation wells, named Well 1 through Well 4. Each of the four lines, named SP1 through SP4, hosted a total of 12 electrodes. Each lines' first electrodes was 2 m from the pumping well, and were numbered E1 through E12, towards their respective observation wells. Electrode spacing for each line was determined by total line distance required to reach each of the sites observation wells.

Spacing between electrodes for lines SP1 through SP4 were set at 2 m, 3 m, 5 m and 3 m respectively.

Non-polarizing, Petiau style (Petiau, 2000) $PbPbCl$ electrodes were used to record electrical signal. Electrodes were buried to a depth of approximately 30 cm, watered to increase contact with ground, and given approximately two hours post-burial to stabilise before data recording commenced.

A reference electrode was buried approximately 150 m from the pumping well. Generally, a further reference distance is favorable, however distance was greatly limited by topographic features including changes in regolith, surface streams and urbanisation.

With use of handheld piezometers, the pumping and four observation wells on site were monitored during the pump cycle. Observations were made both pre-pumping commencement, and throughout the pumping and recovery periods. Measurements taken provided information regarding the water table depth, drawdown or recovery rates, and to the overall shape of the localised water table as a result of the pumping process. Observation wells were PVC (plastic) cased to a depth of 10 m, and continued open and uncased to a depth of 36 m. The pumping well reached a greater maximum depth of 55 m.

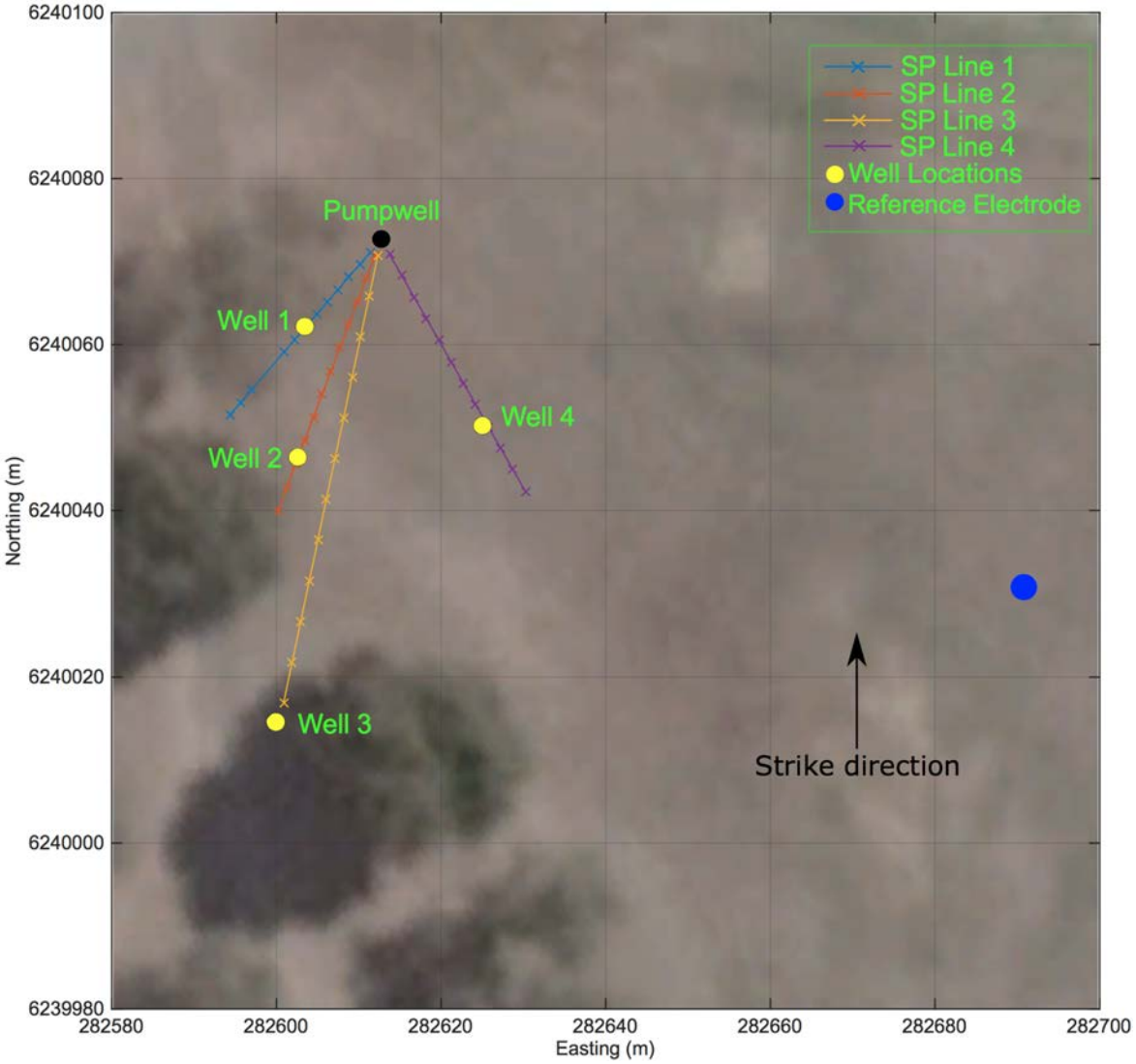

Figure 3.3: A site and surface SP survey array map of the Watervale, Clare Valley, South Australia groundwater investigation location. The SP surface array comprised of four straight line radial arms (from left to right, SP1 to SP4) which connected the pumping well to its four surrounding observation wells. Each radial arm consisted of 12 electrodes (E1 through E12), with E1 positioned closest to the pumping well. Each line required a varied electrode spacing (2 m, 3 m, 5 m and 3 m, respectively) to appropriately position E12 by the observation well. A total of 48 surface electrodes made up the array. The arrays referencing electrodes were approximately 150 m distance from the pumping well.

Figure 3.4: A field photograph of the University of Adelaide SP Instrument setup at the pumping well in Watervale, Clare Valley, South Australia.

3.4 Results

3.4.1 Groundwater pumping

Two days of groundwater pumping investigation commenced on the 9th and 10th of September, 2015. Resulting groundwater level fluctuations (hydraulic head) of the pumping and observation wells for the first day of pumping (9th September) can be viewed in Figure 3.5.

The first groundwater extraction period (P1) began at 14:00:00, with an average pumping rate of 1.1 L/s for an overall 40 minute period concluding at 14:40:00. A recovery period of 1.5 hours (R1) was allowed before the commencement of a second extraction period. This second period (P2) began at 16:10:00, with an average lower pump rate of 0.75 L/s for an overall

35 minute period concluding at 16:45:00. A second 40 minute recovery period (R2) followed.

Using a piezometer, water level of the pumping well was continually measured every one minute. Water level observations for the surrounding four pumping wells were measured every two to five minutes dependent on the drawdown activity.

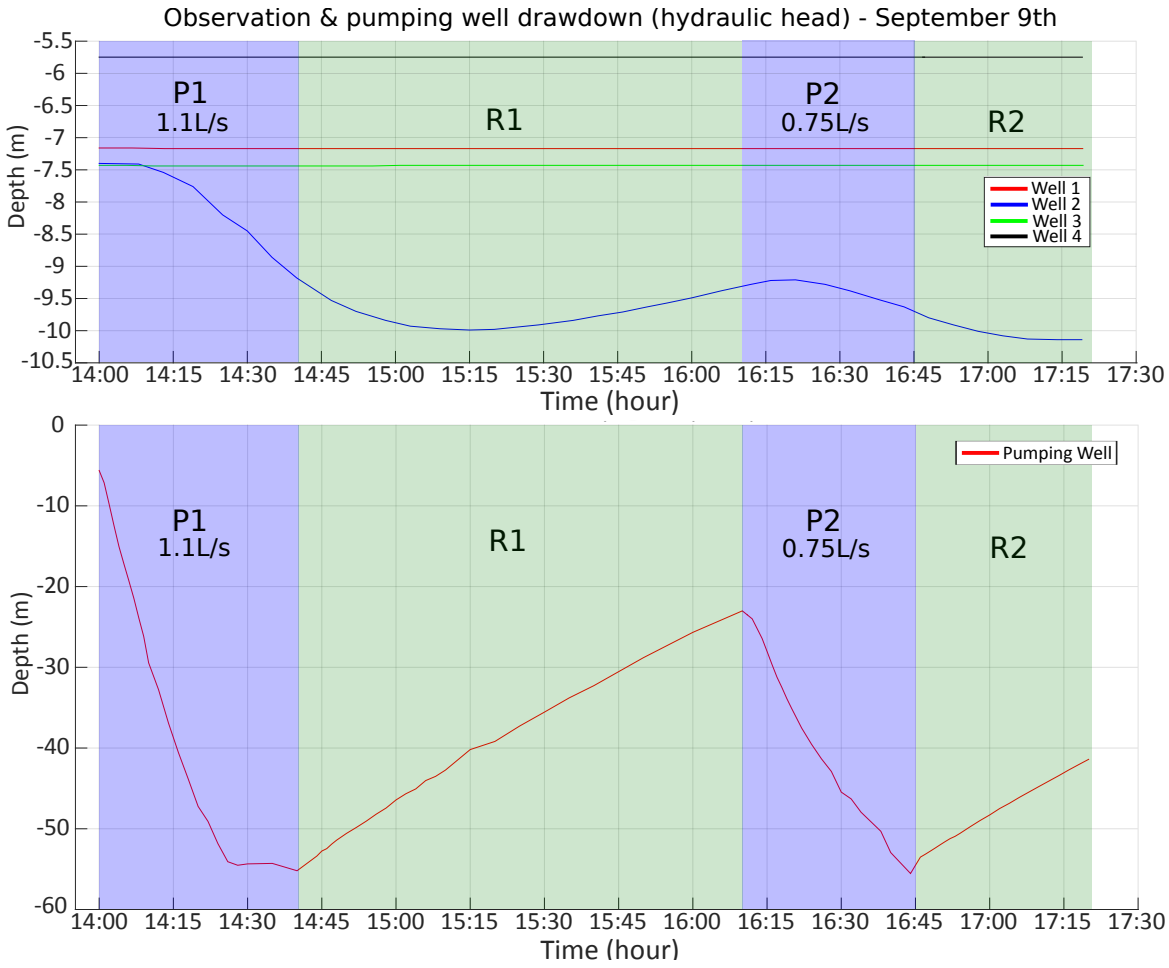

Figure 3.5: Observation and pumping well drawdown (or hydraulic head) for day 1 of pumping tests at Watervale, Clare Valley, South Australia. Blue periods P1 and P2 represent active groundwater pumping periods from the pumping well at rates of 1.1 L/s and 0.75 L/s respectively. Green periods R1 and R2 represent groundwater relaxation and re-infiltration periods. The pumping wells drawdown reaches its maximum well depth of 55 m, thus resulting in a dry well and therefore concluding each of the two pumping periods. Observation well 2 records a maximum drawdown variation of 1.8 m during the R1 relaxation period, and is therefore the only of four observation wells (within 50 m^2 from the pumping well) that is considered hydrogeologically connected to the pumping well via the complex fractured rock aquifer.

P1 and P2 groundwater extraction rates (1.1 L/s and 0.75 L/s) were held at a single steady rate, therefore producing steady electrokinetic responses. Varying extraction rates can subsequently alter an aquifers preferential fluid pathways or hydraulic head properties (Moore and Glaser, 2007), therefore resulting in a varied electrical response.

Both the pumping rate and extraction durations were severely restricted by the quantity of groundwater available within the fractured rock aquifer. Both the P1 and P2 extraction phases extracted groundwater until the pumping well ran dry at a depth of 55 m. From the surrounding four observation wells (all 36 m depth), only Well 2 recorded any observable change to water table level of about 3 m (Figure 3.5) and was therefore considered the most hydraulically connected to the pumping well. Absence of measurable change to water levels among the remaining three observation wells (Well 1, 3 and 4) implies that these wells were not hydraulically connected to the pumping well. The lack of hydraulic connectivity between the pumping well and three of the four surrounding observation wells, all within a small area spanning approximately 50 m^2 , provides us with an exemplar research example of a commonly occurring highly complex fractured rock aquifer system.

Absence of measurable change to water levels among the remaining three observation wells (Wells 1, 3 and 4) implies that these wells were not hydraulically connected to the pumping well. The lack of hydraulic connectivity between the pumping well and three of the four surrounding observation wells, all within a small area spanning approximately 50 m^2, provides us with an exemplar research example of a commonly occurring highly complex fractured rock aquifer system.

The pre-pumping groundwater level in Well 2 was 7.40 m depth (in reference to ground surface), and as a result of the P1 pumping phase fell to 9.20 m depth; an overall 1.8 metre reduction in the water table. Upon commencement of the R1 relaxation phase (totalling 1.5 hours), during the initial 40 minutes (14:40:00- 15:20:00 hours) water level continued to decline and reached a maximum of 10.0 m depth. Eventually, an expected water table stabilisation and aquifer infiltration (refill) processes began (15:20:00 – 16:10:00 hours). By the end of the R1 phase Observation Well

2 had refilled only slightly to 9.40 m depth for an overall 0.6 m water level recovery.

The P2 pumping phase reduced the water level of Observation Well 2 from 9.40 m depth to 9.80 m depth; an overall 0.40 metre reduction of the water table. As for the previous R1 period, during the R2 period water level in the Observation Well 2 continued to drop to 10.14 m over a 25 minute period (16:45:00– 17:10:00 hours). During the R2 phase (totalling 35 minutes), the pumping well water level began at 55 m and recovered to 41 m, a total recovery of 14 metres.

Pumping on the second day was attempted, but due to unexpectedly slow overnight aquifer recovery, sufficient groundwater was not available; pumping could only be conducted for a few minutes, at a very slow and inconsistent rate. Therefore, SP data obtained on this second day of pumping was not used.

3.4.2 SP dataset

Examples of the SP data are presented in Figure 3.6. Lines SP1 (Well 1) and SP2 (Well 2) observed steady and consistent electrical observations throughout the entirety of the investigation. The largest signal variations from pre-pumping voltages occurred in the initial 30 minute period of groundwater pumping during the P1 phase. Over this period, in Line SP2 electrodes E3 through E8 recorded the largest positive mean deviations ranging between + 2.1 mV and + 3.4 mV. In line SP1, electrodes E7 and E8 recorded positive deviations of +2.6 mV and + 3.6 mV. Line SP2 E1 recorded the largest difference of + -4.0 mV, however the spatially close E1 electrodes on Lines SP1, SP3 and SP4 all recorded changes of below + 0.5 mV.

Figure 3.7 presents a crop section of SP1 and SP2 lines during the P1 pumping commencement and conclusion periods. These periods were selected to observe the onset (commencement) and termination (conclusion) of the electrokinetic phenomena on minimum or maximum voltage difference to ground due to pumping. During commencement of pumping, SP1 electrodes E7 and E8 saw changes of approximately + 4 mV and + 2 mV respectively. SP2 electrodes E1, E4, E7, E8 and E12 all saw changes in excess of + 6 mV. Average change across the SP2 line for the period at

+ 4.2 mV. At the conclusion and aquifer relaxation period, largest signal variation drops in SP1 line were again electrodes E7 and E8 to the order of - 4.5 mV, and in SP2 electrodes E1, E3, E4, E7 and E8 to the order of - 5 mV.

Although non-polarizing electrodes were used, based on a visual comparative assessment of the data it was concluded that SP line 4 had not recorded any anomalous electrical behavior resembling SP signal. The line recorded only a slow and very low amplitude drifting that was nearly entirely undisturbed. Additionally, some electrodes from SP lines 1 and 3 were removed to reduce noise within the remaining data. The removed electrodes were potentially affected by features of electrode drift, improper electrode grounding with the Earth that subsequently yielded greatly increased or reduced signal amplitudes, or heterogenous subsurface properties.

In regards to pre-processing of the SP dataset, as the electrodes signals were considerably stable, a equilibrium flatline signal was readily identifiable. A 60 second (0.01 Hz) low pass filter was used on all data to reduce spurious high-frequency effects. On line SP4 data, a linear detrend was applied to reduce slow drifting effects likely caused by its reference electrode not being grounded effectively.

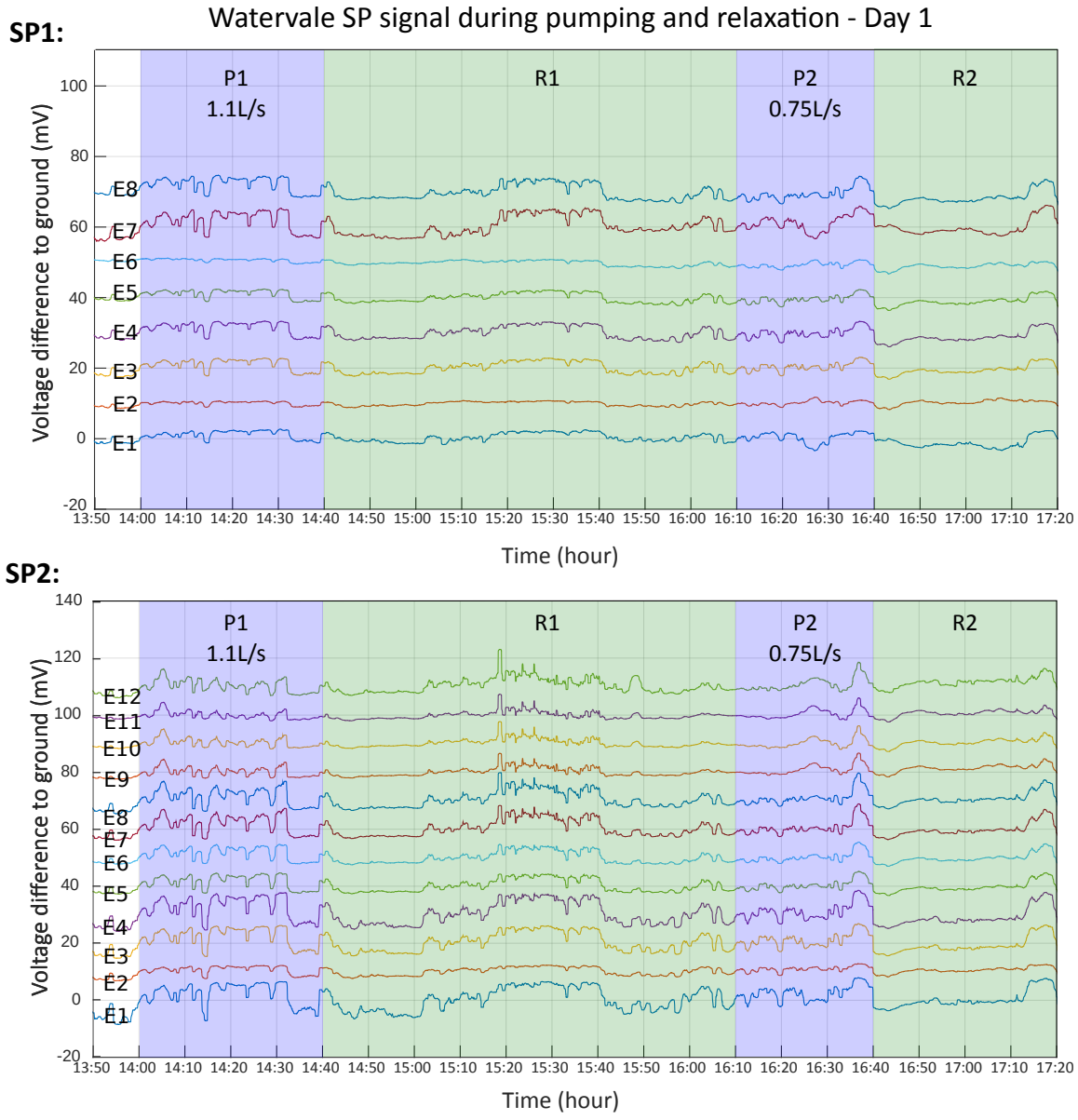

Figure 3.6: SP data results (mV difference from ground) for lines SP1 and SP2 during groundwater pumping tests at Watervale, South Australia. Electrodes on the straight radial arm lines are named E1 (closest to pumping well) through E12 (furthest). Individual electrodes are artificially spaced by +10 mV for ease of visual inspection. A low pass, 60 second median filtration was applied to raw data for smoothing of undesired high frequency electrical noise. Line SP1 electrodes E9 through E12 were removed due to high noise.

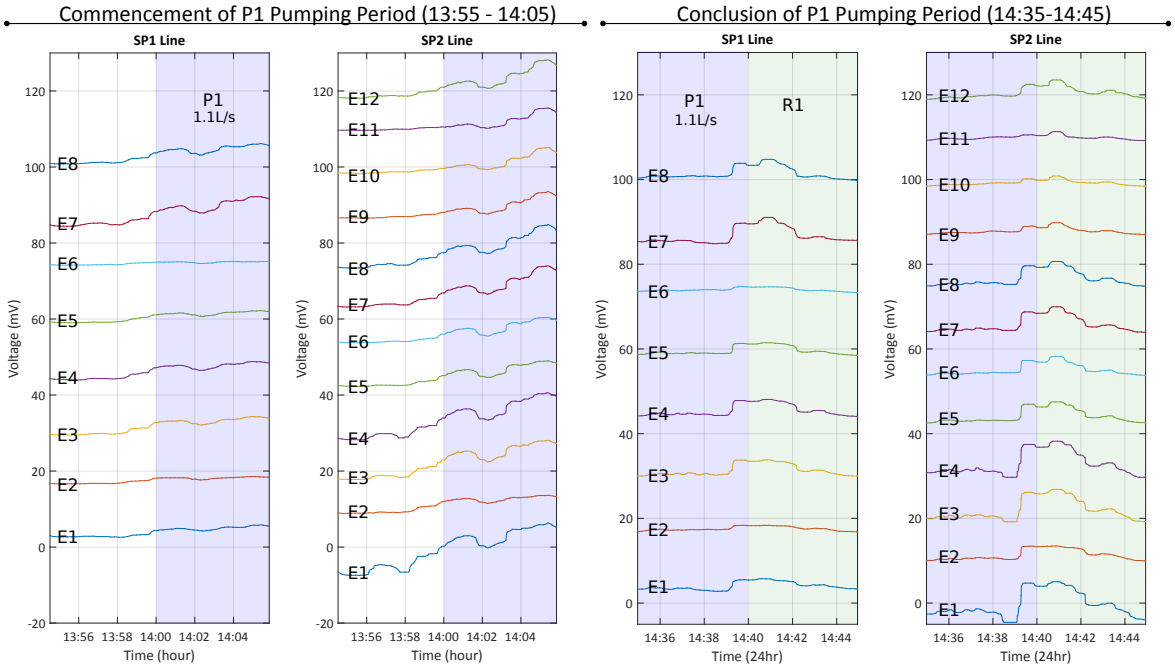

Figure 3.7: SP data results (voltage difference to ground) for lines SP1 and SP2 at the commencement and conclusion of the P1 pumping period. These periods were selected to observe the onset (commencement) and termination (conclusion) of the electrokinetic phenomena on minimum or maximum voltage difference to ground due to pumping. Spacing was applied for readability, and to reflect electrode distance from pumping well. Line SP1 electrodes E9 through E12 were removed due to high noise. During the commencement period (left), maximum changes in excess of + 6 mV were observed on line SP2 electrodes E1, E4, E7, E8 and E12.

3.4.2.1 3-D tomography modelling

The SP tomography technique is an image reconstruction method used to produce a probability estimate of the location of charges in the earth to reproduce observed surface potentials.

Construction of three-dimensional tomographic methods utilised previously discussed work by Hämmann et al. (1997) which expanded on earlier works by Patella (1997a). The algorithms were adapted to calculate absolute potentials rather than electric fields, and to generalise their method from a two-dimensional line-source to a point-source for a three-dimensional Earth.

The algorithm consists of three main steps. Firstly, a scanner function $g(x_i, y_j, x, y, z)$ defines desired elementary point sources across a region (x, y, z), and the potential component at the surface electrodes (x_i, y_j).

$$g(x_i, y_j, x, y, z) = \frac{1}{(x_i - x)^2 + (y_j - y)^2 + (z)^2} \tag{3.1}$$

Secondly, a cross-correlation coefficient is then calculated of the super-positioned source points to the measured voltage data at the electrodes. The resultant $\hat{C}$ is the sum of the observed potentials scaled by g.

$$\hat{C}(x, y, z) = \sum_i \sum_j g(x_i, y_j, x, y, z) \dot{V}_{measured}(x_i, y_j) \tag{3.2}$$

Finally, a normalisation of the cross correlation coefficient allows for direct comparison of coefficients associated with sources at varying depths:

$$C_{normalised}(x, y, z) = \frac{\hat{C}(x, y, z)}{[\sum_i \sum_j g^2(x_i, y_j, x, y, z) \sum_i \sum_j V^2_{measured}(x_i, y_j)]^{\frac{1}{2}}} \tag{3.3}$$

The normalised cross-correlation coefficient varies between 0 (no correlation) and 1 (perfect correlation). The addition of a third-dimension allows for each SP line to be interpolated as a unified tomography output of the investigation site, in comparison to several two-dimensional lines that require extrapolation. This significantly enhances the tomography algorithms potential of higher accuracy results, and and particularly at depth increases the visibility of potential electrical structures.

Our particular tomography technique indicates changes in the quasi-equilibrium source current density of the Earth. This interpretation of the tomography method utilises difference in mean SP (mV) signal (Figure 3.6) when comparing varied phases of conditions in the electrical Earth - for example, comparing signals of a groundwater pumping period to a relaxation period. The resulting electrical field difference tomography therefore indicates the probability that a SP source exists at a given point in both time and space, expressed in a zero to one range scale (low to high SP source probability).

Figure 3.8 presents the pre-pumping versus P1 pumping phases 3-D tomography model. The high SP likelihood zone (> 0.85 probability) encircled in blue is within close proximity (10 m) of the only hydrogeologically connected Well 2; the only of four observation wells that recorded groundwater level fluctuation during the pumping investigation (see Figure 3.5). The high likelihood zone begins at the near surface, and forming a tear-drop shape expands into the Earth beyond approximately 20 m depth. Both the end electrodes of line SP3 and line SP4 encircled in green present a very low probability (< 0.3 probability) of hosting anomalous SP signal.

The models mid-range probability regions (light-red) are mostly zones which did not have enough spatially relevant surface SP electrode data to better determine the probability of a SP source.

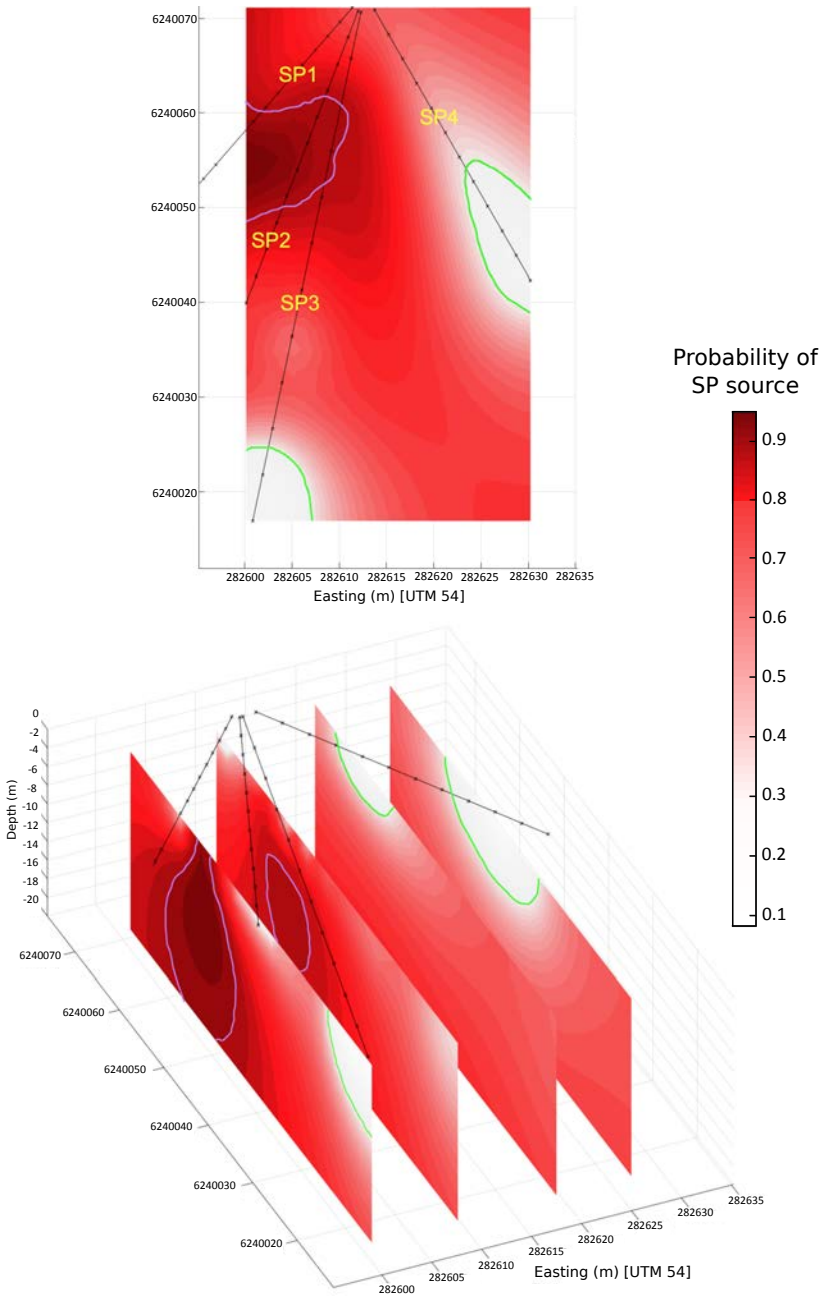

Figure 3.8: 3-D tomographic modeling output of SP dataset during groundwater pumping investigation at Watervale, South Australia. The technique indicates changes in the quasi-equilibrium source current density of the earth. This interpretation utilises difference in mean SP (mV) signal (Figure 3.6) between the 30 minute pre-pumping phase, and initial 1.1 L/s pumping phase (P1, Figure 3.5) of each given electrode. Resulting tomography output therefore indicates the probability between 0 and 1 that a SP source exists at a given point. Zones of highest (blue, > 0.8) and lowest (yellow, < 0.3) probability are encircled. Top: A birds eye (z-layer) view of the site tomography results at 10 m depth. Bottom: A panned view of easting (x-layer) slices to reveal the tomography's features of interest. Clearly shown is the size, shape and depth of the sites highest likelihood SP source between lines SP1 and SP2.

3.5 Discussion

The SP dataset collected suitably correlates with recorded observation wells drawdown fluctuations. Well 2 was the only observation well to demonstrate any variation as a result of the P1 and P2 pumping phases, and electrode line SP2 adjoining the pump,ing well and Observation Well 2 also recorded the largest mean SP signal shift. The SP dataset supports a conclusion that below SP line 2, between the pumping well and Well 2, a fractured rock pathway is the only preferential flow path within the surveyed area.

Our pumping investigation could draw on some comparisons with previous work done at the Watervale groundwater site by Fagerlund and Heinson (2003). For this investigation, groundwater pumping was instead conducted from Well 2 at a higher flow rate of 2.0 L/s over a longer period. Unlike our results, drawdown was recorded in all four of the surrounding wells. Well 1 experienced the highest drawdown fluctuation (6.5 m, five times higher than other surrounding wells), therefore having the highest hydraulic conductivity with the pumping well (Well 2). Although during our investigation Well 1 did not record drawdown as a result of pumping, the SP1 line (above Well 1) did record slightly elevated SP signals. Amounting these previous and new findings, it was likely Well 2 and 1 were in some way still hydraulically connected via the complex fracture system, but groundwater was rapidly infiltrating Well 1 from an alternative unknown location and depth.

In comparison to previous works, the lower flow rate and decreased hydraulic conductivity of the Watervale site was likely due to build up of fine groundwater particles and silts over time obstructing flow. The highest of four groundwater samples tested measured a 770 ppm salinity content, and was therefore considered very slightly saline to fresh.

Tomography of the pre-pumping versus P1 pumping event (Figure 3.8) located the highest likelihood of SP signal source to have originated nearby to Well 1 and 2, at between 10 m to 18 m depth. Referring to Figure 3.9 of previously conducted down-hole electrical and temperature gradient measurements at the investigation sites pumping well, we observe a fracture plane likely exists at a depth of approximately 15 m (Love et al., 2001).

Overall, available geophysical datasets from previous research are well correlated to the investigations acquired groundwater monitoring, SP survey and tomography results.

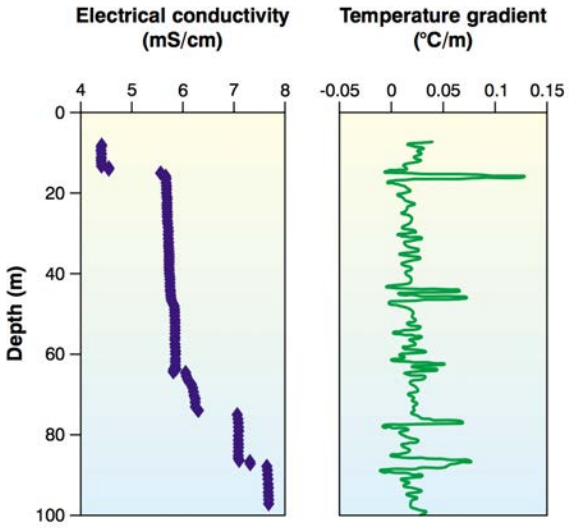

Figure 3.9: Downhole electrical conductivity and temperature gradient measurements of the main pumping well (SA water number 6630-3062) at the groundwater investigation site in Watervale, South Australia. Fluctuations of downhole conductivity and temperature gradients are excellent indicators of potential fracture plains at depth. Several potential fracture planes are present, most obviously at 20 m, 75 m and 85 m depths. Original figure from Love et al. (2001).

3.6 Conclusion

Based on observation well data, both Fagerlund and Heinson (2003) and our findings inferred that the preferential groundwater flow direction was north to south. Although the output tomography data is well correlated with supporting geophysical datasets, a specific fracture orientation and non-azimuthal (to the pumping well) groundwater flow direction can not be interpreted from the shape of the tomography SP source. The Watervale survey was severely hindered by surface obstacles (eg. surface streams, flora, urbanisation) that did not allow for a more uniform, widely distributed electrode arrangement. The site epitomizes the heterogeneity of detecting fractured aquifer fluid pathway flow, with only one of four observation wells within a small 50 m^2 area appearing to be hydrogeological connected to the pumping well. However, the overarching success of the

SP and tomography techniques correlating with piezometer measurements and additional geophysical investigations gives confidence to the potential for the SP technique to be utilised, even only quantitatively, for the detection of preferential pathways in fractured rock. The relatively high horizontal resolution of the SP technique survey can be very useful in these fractured rock conditions for targeting of regions of interest surrounding a well. Combination of SP methods with additional geophysical techniques (invasive or non-invasive) can result in an overall greater understanding of a given heterogenous groundwater system, whilst also potentially reducing surveying costs and duration.

CHAPTER

FOUR

FRACTURED ROCK AQUIFER 2: BALHANNAH

4.1 Aim

A groundwater pumping and surface SP survey investigation was conducted at a fractured rock aquifer groundwater research site in Balhannah, Adelaide Hills, South Australia. The principal aim was to detect anomalous electrical potential differences at the sites surface generated as a result of groundwater pumping, and therefore presumed to of an electrokinetic nature. Additionally, drawdown levels of the pumping at several surrounding observation wells were monitored to be compared with the SP surveys resulting 3-D tomography dataset.

As a secondary investigation aim, previously tested iron based, zinc galvanised alloy electrodes were substituted for standardised Petiau non-polarising style electrodes. These electrodes are low in cost, and rapid to set-up - their overall electrical stability and performance will be evaluated and discussed.

4.2 Background

4.2.1 Site description

Balhannah, shown in Figure 4.1, is a township within the Adelaide Hills, roughly 30 km south-east of Adelaide, South Australia. The key land uses

are primarily vineyards and grazing, however semi-urban living also plays an important role. The region is characterised by broad, undulating valleys with elevations generally at 400-450 m above sea level.

Annual Rainfall in Balhannah is 807 mm, and overall catchment totals to 8,261 ML, with an effective rainfall penetration of 6,615 ML due to surface evaporation during summer rainfall events. Only winter rainfall (April-October) is considered as effectively contributing to the water table level (Zulfic et al., 2008)

4.2.2 Geology

The greater Onkaparinga Catchment is underlain by consolidated basement rocks, including: The Barossa Complex, Adelaidean sediments, and the Kanmantoo Group; All of which are present in the Balhannah catchment region.

The Barossa Complex basement is comprised of high pressure and temperature metamorphosed rocks including gneisses, schists, and pegmatites. They occur at the center of large folds, and are exposed at surface due to erosion. This exposed basement forms the Oakbank inlier present within the Balhannah Catchment (Zulfic et al., 2003).

The Adelaidean sediments (Adelaide Geosyncline sediments) overly the Barossa Complex and is present through out most of the greater Onakparinga Catchment Region. It is predominately comprised of marine environment sediments, and some minor volcanics. The belt ranges up to 24,000 m in thickness. The rock unit has been strongly folded, but is relatively unaffected by heat processes (Zulfic et al., 2003).

4.2.3 Groundwater

Groundwater moves through, and is stored within the mostly fractured rock aquifers that underlie the Onkaparinga Catchment. There are generally three groundwater flow systems operating within these fractured rock aquifer systems. Firstly, a shallow groundwater flow that manifests from seepage to drainage lines after heavy rainfall events - these groundwater transport times are typically in the order of days. Secondly, an intermediate system that provides much of the baseflow to discharge points - these groundwater transport times are typically in the order of weeks through to

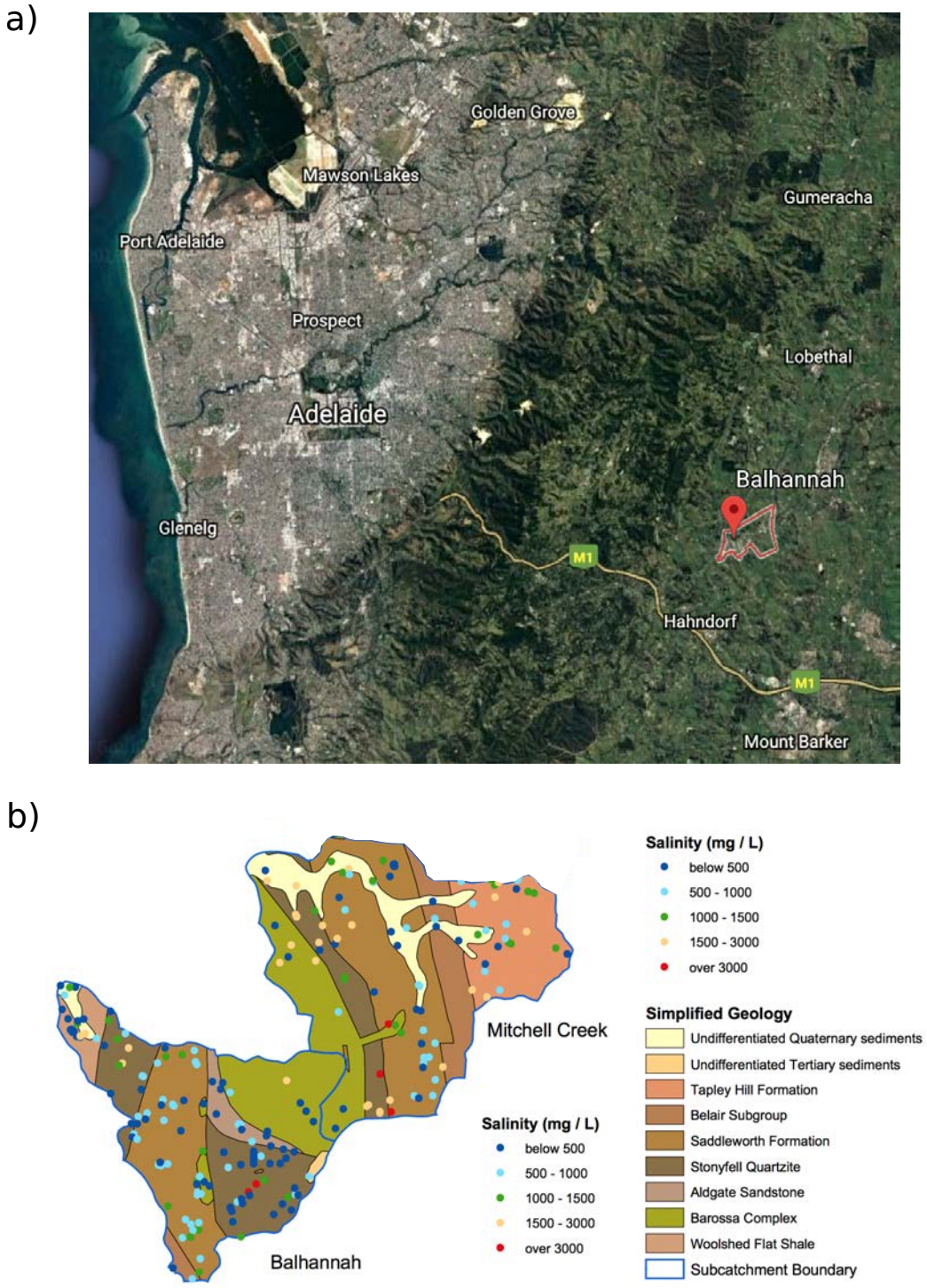

Figure 4.1: *a)* Location map of the Balhannah Region, Adelaide Hills, approximately 50 km south-east from Adelaide City.*b)* A generalised geological map and approximate borehole yield rates of the Balhannah and surrounding Adelaide Hills region. As is the nature of fractured rock aquifers with complex heterogeneous flow paths, groundwater borehole yield in the region bears no obvious geographical interrelationships. Yield is generally low (below < 1 L/s), although some high yield boreholes (> 10 L/s) do exist. Reworked from original figure by Zulfic et al. (2008).

decades. Finally, a deeper regional system where groundwater transport times are typically in the order of several decades to centuries or more.

Aquifer yield, salinity, and recharge rates can vary quite significantly within, and across the sub-catchment areas. Groundwater yield (Figure 4.1) and salinity are more favourable in the western catchment areas, in comparison to the east in areas such as Balhannah. Due to the nature of fractured rock aquifers, recharge rates are broadly varied with no obvious geographical interrelationship.

Within the Balhannah region, there is no obvious correlation between geology type and groundwater resource quality. Groundwater salinities are highly variable, ranging from between 500 to 3000 mg/L, and typically supplies from aquifers are below 5 L/s. A small number of bores managed to supply in the 5-10 L/s range.

The current groundwater usage in the region is estimated at 930 ML per annum. First-order approximations for the Balhannah regions aquifer recharge is 1300 ML per annum. To satisfy the concept of sustainable yield from an aquifer, the long-term rate of withdrawal should be equal to, or should not exceed the average annual recharge of the groundwater resource. Due to the reliability and limitations of methods used to determine recharge values, it is suggested that no higher than 50% annual recharge (650 ML p.a.) is extracted. As actual usage near exceeds the 75% annual recharge, it is evident that there is a potential to over use groundwater resources.

4.3 Field survey

A graphical representation of the Balhannah site layout, and the locations of pumping and observation wells can be seen in Figure 4.2. A surface array of 48 electrodes was used to measure changes to the electrical potential field as a result of groundwater pumping. The array comprised of four lines split in two for a total of eight straight-section lines. Each of these straight line sections hosted six electrodes. Lines two, three and four were positioned directly within the zone of observation wells. Line one was positioned further from the pumping zone to provide a more spatially distributed array, and therefore a potentially greater range of electrokinetic signal contrast during the pumping investigation.

A spacing of 5 m was used between each electrode along the line, and between each of the split lines. Each of the four full lines were spaced 10 m apart. Overall, the gridded array covered a total 50 m by 25 m area. A reference electrode was buried approximately 200 m from the central pump well. This distance was greatly limited by inaccessible, urbanised zones surrounding the site.

The array positioning was central to the groundwater pumping well. A total of seven observation wells were used to monitor the sites groundwater drawdown. Hand-held piezometers were used to monitor drainage rates, and overall shape of the localised water table as a result of the groundwater extraction process. Observations were recorded pre-pumping, throughout and post-groundwater pumping.

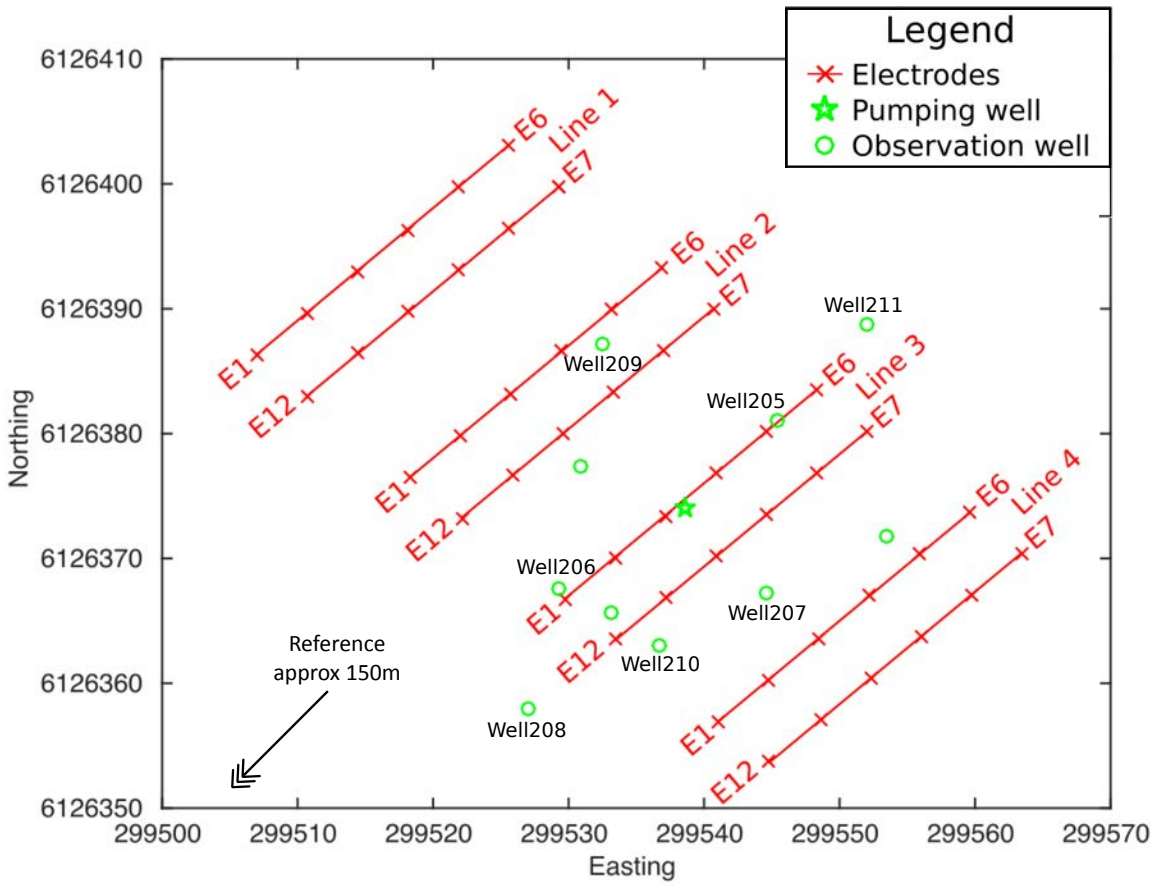

Figure 4.2: A map of the Balhannah, Adelaide Hills, South Australia groundwater investigation site. The SP surface array comprised of a total 48 electrodes forming a gridded formation. Three of the four SP lines (Lines 2, 3 and 4) were central to the pumping and observation wells. Line 1 was positioned further from the pumping well to provide a greater contrast to the observed electrokinetic signal caused by flow of groundwater.

4.4 Results

4.4.1 Groundwater pumping

Groundwater pumping commenced at the investigations sites central pumping well on February 4th, 2015. The overall observation and pumping well drawdown levels (hydraulic head) can be viewed in Figure 4.3. Following some allowance of time for buried electrodes to settle, The initial extraction period (P1) commenced at 13:15:00 with a steady rate of 1 L/s. An almost immediate drawdown of 5 m was recorded in the pumping well, but steadied relatively quickly for the remaining length of the P1 period. All observation wells recorded observable change during this period, and

therefore were all considered hydrogeologically connected with the pumping well.

The P2 pumping period was commenced at 15:35:00, increasing the pumping rate to 1.5 L/s. The pumping well water level began to rapidly subside, decrease 20 m within a one hour period. The increase P2 flow did not increase drawdown rates of the surrounding observation wells. It was evident there was a greatly limited permeability between the pumping and observation wells. Finally, the P3 phase which commenced at 16:35:00 increased pumping rate to 2.0 L/s. Due to recharge rate, the increase rate was only sustained for approximately 5 minutes until the pumping well was dry to its maximum depth of 60 m.

Radially outwards from the pumping well, surrounding observation well water table levels had not been greatly reduced. After all three pumping phases were complete, total drawdown within surrounding observation wells were between 2 m to 5 m total depth. Subsequently, an acute cone of groundwater depression had been formed during the groundwater investigation. These cones are typical of groundwater pumping investigations, however the particuarly acute cone shape was likely a result of limited permeability in the aquifers interconnecting conduits.

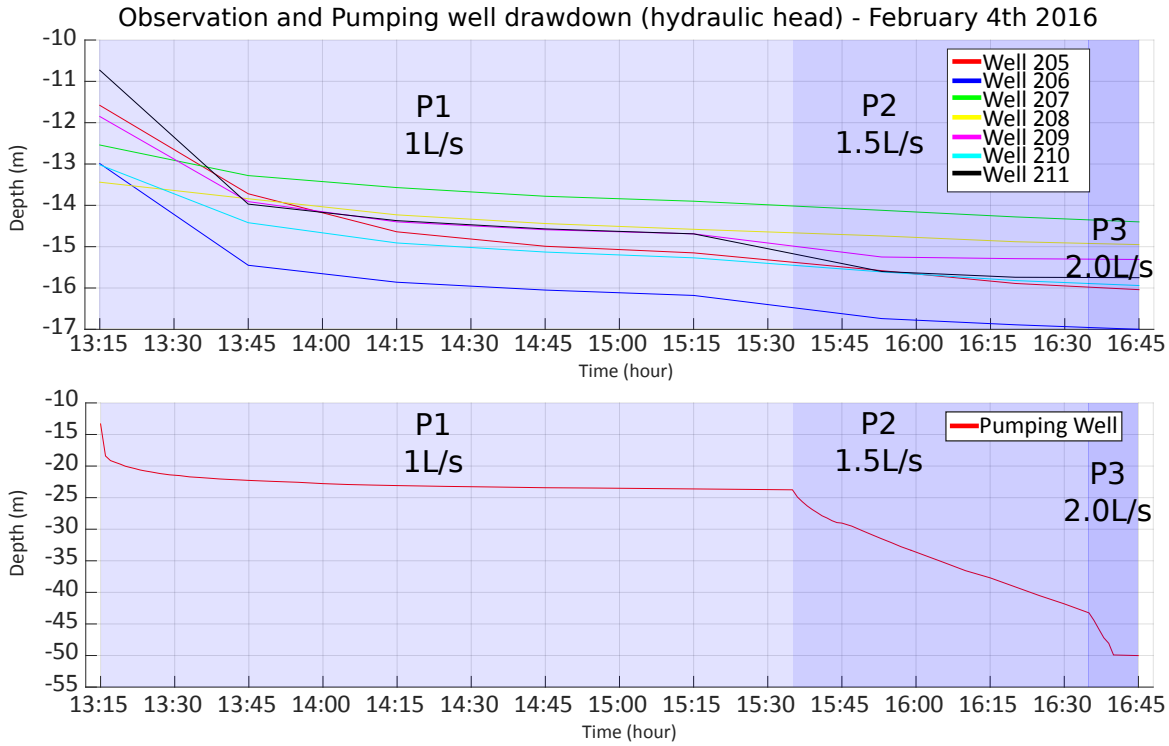

Figure 4.3: Observation and pumping well drawdown (or hydraulic head) of groundwater pumping investigation at Balhannah, Adelaide Hills. Blue periods P1, P2 and P3 represent active groundwater pumping periods (from the pumping well) at rates of 1.0 L/s, 1.5 L/s and 2.0 L/s respectively. The pumping well reaches its maximum well depth of 60 m at the conclusion of the pumping period. All surrounding observation wells record drawdown variations during the pump, most significantly on average approximately 2.5 m in 30 minutes at the commence of pumping (P1 period).

4.4.2 SP dataset

Full results of the Line 1 and 4 SP dataset are presented in Figure 4.4. Analysing these results, at first glance a significant amount of sporadic electrical behavior is evident.

Pre-commencement of the P1 pumping phase, a vast majority of the electrodes signals appear to be quasi-static and overall ideal, particularly in lines SP1 and SP4. At both the commencement or early stages of the P1 pumping phase, no low-frequency signal amplitude fluctuations due to the generation of a localised electrokinetic field are detectable. Several electrodes on lines SP4 exhibit some time correlated (see times 14:20, 14:50 and 15:45) square wave features that from 2 mV to 5 mV in amplitude.

These electrodes have no spatial significance to one another, and its source was not determined.

The P2 phase displayed multiple time correlated, high frequency features (see times 16:05 to 16:15). These are considered unwanted noise, likely caused by anthropogenic features. Again, during both P2 and the final P3 phase there were no observed and correlating low-frequency shifts of signal amplitude.

Presented in Figure 4.5 are a select number of electrodes from each of the four SP lines that best represented the overall dataset trend. The additional filtration provides insight to the low signal amplitudes and fluctuations observed during pumping. Histograms for one of the lowest fluctuating (bottom left, Figure 4.5, Line 1-E11) and highest fluctuating (bottom right Figure 4.5, Line 3-E11) electrode signals present considerably small amplitude distributions from mean of 0.1 mV and 0.4 mV respectively. The higher amplitude Line 3-E11 was situated in the near vicinity (5 m) of the pumping well, and components of trend and increased amplitudes could possibly be related to pumping activity. This trend and increased amplitudes were not observable to neighbouring electrodes, however.

Long term electrode drifting effects are particularly notable. These effects were likely due to known polarisation issues of the alloy electrodes being tested as part of the overall SP investigation. Although disruptive, the linear nature of the drift can be corrected with pre-processing, and therefore bears little influence on detectability and measurement of anomalous, short-term electrical features.

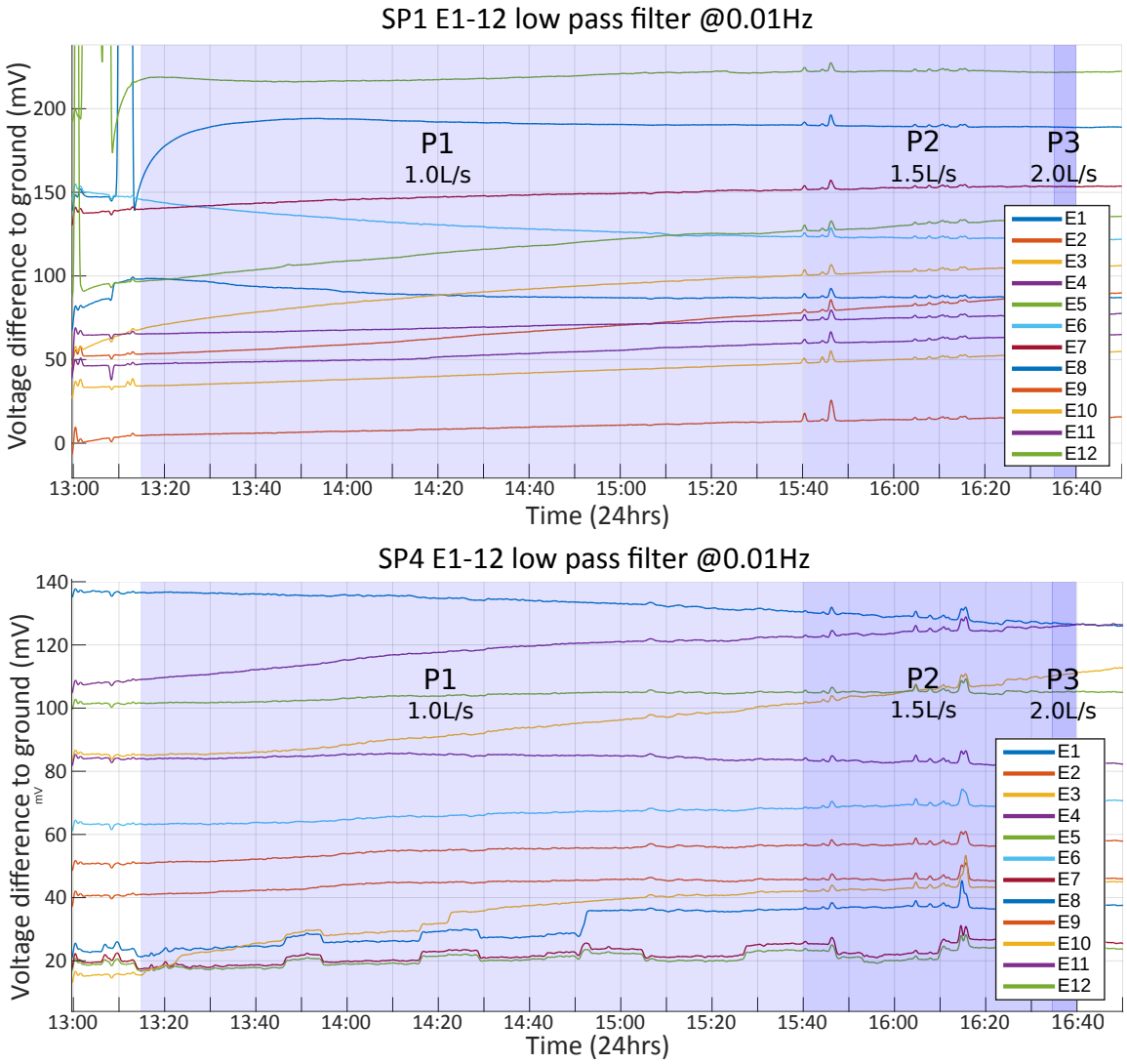

Figure 4.4: SP data results (mV difference from ground) for highest quality lines SP1 and SP4 during groundwater pumping tests at Balhannah, Adelaide Hills. A low pass filter @0.01Hz was utilised to reduce high frequency noise. Signals were all characterised by little to no low-frequency signal fluctuation that which could be attributed to the presence of groundwater flow (electrokinetic signal), varying degrees of longer term drift, and some high amplitude electrical disturbances and general instability. Likely reasons for low quality SP survey results can be attributed to the use of experimental alloy electrodes, and presence of anthropogenic noise at the investigation site.

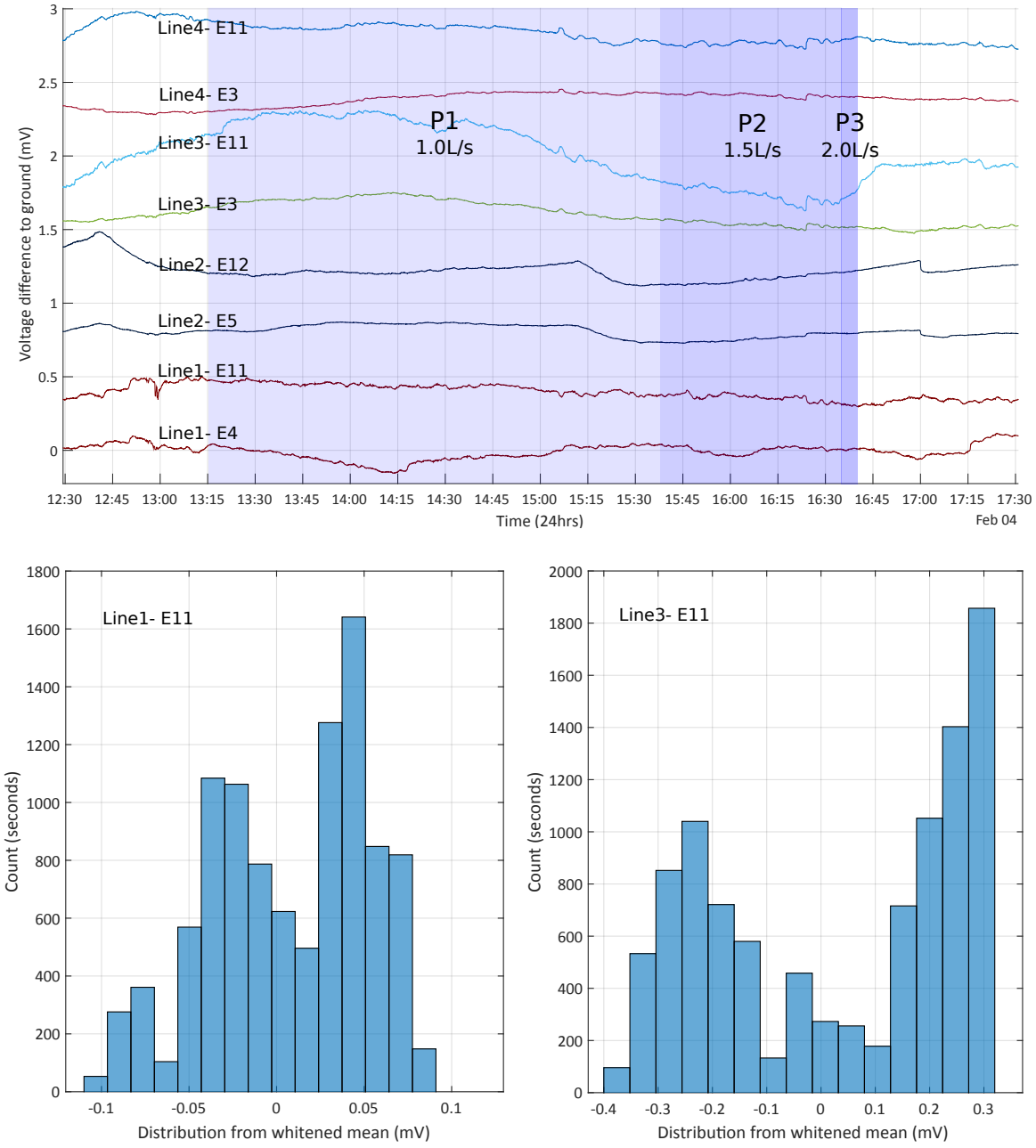

Figure 4.5: SP data results (mV difference from ground) for a select number of electrodes during groundwater pumping tests at Balhannah, Adelaide Hills. Two electrodes were selected from each line within the array that best represented the overall dataset trend. SP data was whitened (meaned) to zero, a low pass filter @0.01Hz was utilised to reduce high frequency noise, and a linear detrend applied to reduce electrode drift effects. Spacing was applied between electrodes for purpose of comparison. Overall, all electrodes observed very low amplitude signal variances. Below are signal distribution histograms for Line 1-E11 (left) with considerably low signal variance, and Line 3-E11 (right) which observed the highest signal variance within the array. Note the considerably low amplitude of signal variance in both these histograms.

4.5 Discussion

With a large part of the experimental aim regarding the analysis of the alternative alloy electrodes (and in general low-cost electrodes) effectiveness, pre-commencement of SP recording the electrodes contact (to ground) resistances were continually assessed for approximately two hours. For these measurements, handheld digital-multimeters (in resistance mode) were used at the analogue channel inputs. Each electrode was tested to be in the vicinity of 10 kΩ when possible, but were ensured to be always below 100 kΩ. When an electrodes contact resistance was considered too high, the electrode would be adjusted or moved a small distance (approximately 20 cm). No water was added to increase the electrodes contact to ground, and therefore once contact was properly established resistances did not readily fluctuate within this two hour period.

A large amount of high-frequency noise observed was likely due to anthropogenic effects. The site was situated next to a main transport road with nearby above ground electrical power lines. This is also the likely source of the square wave signals, although its spatial variability (not present in all or most electrodes) is difficult to understand. Due to this spatial variability, there may have been some instrument issues. Self-calibration tests post-survey returned that the instrument had no internal issues, and previous testing of the components (see Section 2.3.2 presents the logger to be highly accurate over long periods.

Although a great deal of effort went into ensuring the alloy electrodes were both effectively pre-cleaned of any residues, and on installation had adequate contact to ground, results were still disappointing. Overall, reasonable SP data of the sites electrical fluctuations could not be generated. All electrode signals were stable and consistent, although very little low-frequency fluctuation could be seen. Some electrodes, particularly all electrodes of line SP1 had very little signal electrical amplitude (high or low).

4.6 Conclusion

Lower quality SP data was expected as a result of trialling alternative iron alloy, zinc galvanised electrodes. However, data obtained was severely

lacking features of any considerable fluctuations in signal amplitude, was sensitive to high-frequency noise which required filtering, and overall no likely sources of electrokinetic phenomena were likely across the entire array. Previous laboratory testing concluded electrical signal was comparable to that of several other Petiau style and alloy electrodes, and had not alluded to the severity of these potential issues encountered.

Tomography methods applied to any of the three recorded pumping phases were not helpful in identifying any plausiable sources of a potential electrokinetic phenomena source. It is possible that very little to no surface detectable electrokinetic signal was generated, however both considering the shallow depth of the investigation, and comparing obtained signal to that of previous fractured rock aquifer investigations in Watervale, Clare Valley which utilised the same recording equipment setup (excluding electrodes), one would conclude the overall non-success was likely due to electrode selection.

Although disheartening, it was a valuable lesson regarding the importance of using more reputable non-polarising electrodes when conducting electrokinetic investigations. In comparison to alternative geophysical methods, particuarly non-passive methods, SP surveys are already considered considerably lower cost. Further investigations aiming at industry level implementation should be conducted and encouraged to assist in promotion of the methods revivial, in particuarly for its usefulness as a groundwater flow-sensitive tool in complex fractured rock investigations.

CHAPTER

FIVE

4-D TOMOGRAPHY OF EASTERN MOUNT LOFTY RANGES

In 2007, with the assistance of various government environmental agencies and landowner's permissions, the University of Adelaide collected an extensive geophysical dataset within the Eastern Mount Lofty Ranges (EMLR) region. In total, 21 groundwater pump investigations were conducted utilising both SP techniques, and complimentary borehole-to-surface electrical resistivity techniques. These collected SP datasets were generated into electrical potential maps, and analysed in conjunction with supporting two-dimensional borehole-to-surface electrical resistivity (ER) datasets. A majority of these EMLR sites were published in a government report by Zulfic et al. (2008).

Raw SP data from the original EMLR region investigation was made available, and four sites were selected to be reprocessed and analysed utilising newly presented 4-D tomographic processing methods. Tomography methods and addition of dimensions greatly improved on geospatial delineation of potential electrokinetic sources, and allows a viewer to recognise and differentiate electrical activity at various phases of the groundwater pumping event.

5.1 Aim

Extensive SP data previously collected in 2007 by the University of Adelaide and various government agencies provided some further insight for the analysis of fractured rock aquifers. SP proved to be in particularly useful for both comparison and verification of supporting ER geophysical dataset findings. These findings were presented in Zulfic et al. (2008) as both signal difference as a function of time, and alternatively as singular two-dimensional surface maps.

Expanding on these previous works, this chapter aims to draw further conclusion from SP datasets of groundwater flow activity by addition of both a spatial third-dimension and fourth time-dimension within a singular tomographic analysis framework. The addition of these third and fourth-dimensions allow for electrokinetic source depth delineation, and time-based smoothing to reduce the effects of inconsistent and spurious noise sources.

Newly developed four-dimensional tomographic results will be compared for both similarities and inconsistencies with original ER results from Zulfic et al. (2008). Discussion and an overall conclusion will be drawn regarding the usefulness of higher-dimensional analysis of SP datasets for groundwater flow investigations.

5.2 Background

5.2.1 Site description

The Eastern Mount Lofty Ranges (EMLR) region is located approximately 50 km south-east of Adelaide, South Australia. The region spans a total area of 2845 km^2, connecting eastern slopes of the Mount Lofty Ranges across to the western Murray Plains, and from Milendella Creek catchment in the north through to Currency Creek catchment in the south. A total of thirteen water catchments form the EMLR region, draining into both the River Murray and Lake Alexandria.

Water resources of the EMLR region support local agricultural and industrial activity. The regions economic and population growth are heavily reliant on both a readily available, and rapidly expandable groundwater

supply. Overdrawing of the finite resource can result in increased salinities due to lateral movement of saline groundwater lenses, and a deepening of the groundwater level for inexplicit time periods. No monitoring to date has made evident any adverse impacts on the regions groundwater resource (Zulfic et al., 2003). It is of importance however to further understand and continually investigate the state of a groundwater resource which is heavily relied upon.

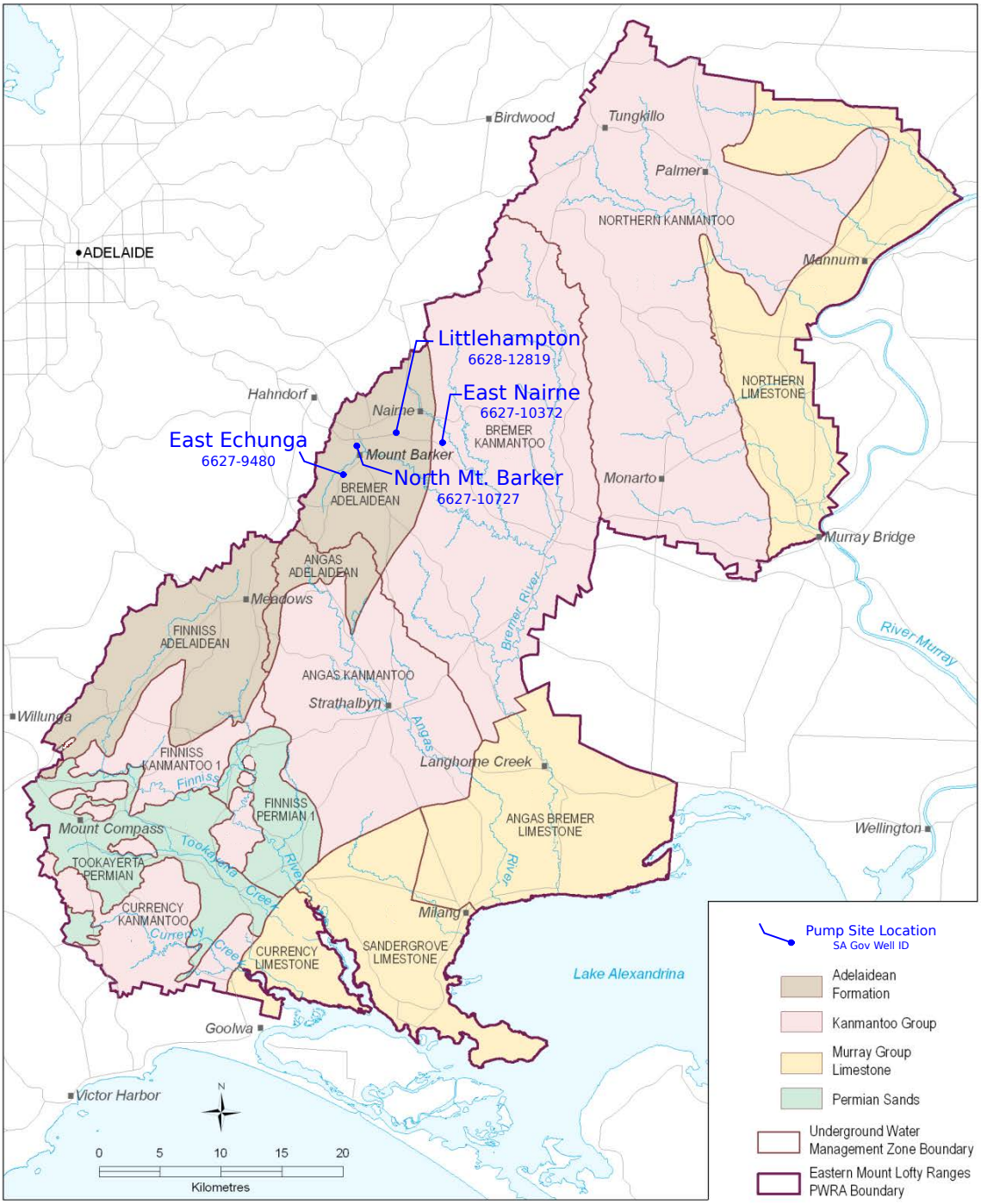

Figure 5.1: The Eastern Mount Lofty Ranges (EMLR) region of South Australia, and the locations of sites selected from Zulfic et al. (2008) for reprocessing of original SP datasets. The sites are named in accordance their nearest township, and their South Australian government well identification numbers. Reworked from original figure by Zulfic et al. (2008).

5.2.2 Geology

The EMLR region forms a part of the larger Adelaide Geosyncline; a failed continental rift valley exposed as ranges in South Australia extending from inland Arkaroola, south towards to Kangaroo Island (Love et al., 2001). A majority of faults in the EMLR trend north-east to south-west (Tokarev and Gostin, 2003)

Catchments of the EMLR region are underlain by consolidated basement rocks beneath elevated areas, and unconsolidated sediments beneath the lower Murray Plains. Principal litholgies include: the Kanmantoo Group comprised of metamorphosed schists, greywackes, and gneisses; the Normanville Group comprised of calcareous shale, phosphatic phullite, and marble; the Umberatanna Group comprised of shales and siltstones; the Wilpena group comprised of siltstones; and finally the Burra Group comprised of quartzites, sandstones, dolomites and shales (Zulfic et al., 2003).

5.2.3 Groundwater

Mean annual rainfall in the EMLR is estimated at a highly variable 500-800 mm/year. This ranges from 1600 mm/year at Mounty Lofty summit, to less than 300 mm/year in the Monarto area. Typically, a majority of this rainfall occurs during winter months (Zulfic et al., 2008).

Major freshwater streams that flow from the EMLR into the River Murray include both the Marne River, and Reedy Creek (Zulfic et al., 2003). Additional streams contribute small quantities of water into the River Murray and Lake Alexandrina catchments, but these are generally ephemeral and highly saline streams.

The regional groundwater catchments are also highly variable, and an estimated 75% of the region is underlain by poor quality aquifers bearing low yield (below 5 L/s) and highly saline (greater than 3000 mg/L) properties. Additionally, there is very little to no capacity for development of these groundwater resources through use of fracking or flushing techniques. Salinity can vary from less than 300 mg/L in higher rainfall and topography areas, to upwards of 10,000 mg/L in lower rainfall regions. Due to higher rainfall and presence of the permeable Adelaidean fractured rock

and Permian sands, groundwater yield and salinities are most favourable in the western and southern EMLR areas.

5.3 Field surveys

Original acquisition techniques and field survey processes are described from information originally provided by the Zulfic et al. (2008) report.

5.3.1 Borehole-to-surface electrical resistivity

Borehole-to-surface electrical resistivity (ER) surveys were conducted at each of the EMLR sites to provide additional complimentary geophysical data for SP surveys. At each site, the active source current was located either downhole of the groundwater bore, or if available connected to its metal borehole casing. This arrangement ensured each site was both energised to depths below that of weathered surface materials and within the water table.

Uniformalised arrays of 72 surface electrodes were used at each site. The array structure consisted of 12 straight-line radial arms at 30° separations, all extending from the centralised groundwater pump location. Each radial arm consisted of six electrodes; the first of six electrodes beginning at 5 m distances from the centralised pump, and all subsequent electrodes evenly spaced at 5 m intervals from the previous. Alike to the SP setup, each of the 12 radial arms extends to a total distance of 30 m from the centralised pump (commencing at 5 m towards 30 m). A return current electrode was located at an approximate 200 m distance from the surface electrode array, and subsequently completing the electrical circuit where the return current electrode's value was considered as infinity.

Contoured surface maps were produced showing electrical potential measured, normalised by the input current (sometimes called the transverse resistance) (Skinner and Heinson, 2004; DEWNR, 2009). Zones of high electric potential were interpreted to have good electrical connection with the borehole, which in theory would indicate the location of hydrous fractures or bedding planes.

Dip and strike of conductive elements at each site could be inferred from data. Dip calculated by measuring the distance of lateral offset of the maximum transfer resistance value from its expected location (directly above

the current electrode). Strike can be determined by orientation of the maximum axis of the equipotential ellipse of the surface maps (Skinner and Heinson, 2004). It can be implied there is a dipping conductive structure when the maximum normalised potential is offset from directly above the borehole. The direction of dip of the conducting structures can be inferred as at a right angle to the strike, and towards the more resistive surrounding structures (Skinner and Heinson, 2004).

From concentric, symmetrically (isotropic) distributed normalised potential contour maps, we can infer that there is one major orientation for the conductive groundwater fractures. Asymmetrical (anisotropic) distribution of normalised potential contour maps can be indicative of a secondary directional conductive fracture zone.

Patterns of slightly asymmetrical, anisotropic shapes around the borehole are likely due to errors in the positioning of the electrodes and are to be discarded. Positioning errors will affect electrodes closest to the borehole when compared against electrodes further out.

5.3.2 SP survey

As measurable and reliable groundwater movement was required to stimulate the desired electrokinetic phenomena, site locations were selected based on their groundwater yield. In many cases, pre-existing in-hole pumps at depths ranging between 30 m and 80 m were utilised. However, some sites did require an external pump brought to site.

SP surveys within the EMLR region were conducted using a uniformalised surface array consisting of 36 surface electrodes and a distant reference. The uniform array structure consisted of six straight-line radial arms at 60° separations, all extending from a centralised groundwater pump location. Each radial arm consisted of six electrodes; the first of six electrodes beginning at 5 m distances from the centralised pump, and all subsequent electrodes evenly spaced at 5 m intervals from the previous. The radial arms extend to a total distance of 30 m from the centralised pump (commencing at 5 m towards 30 m). Reference electrodes were located at approximately 200 m distances from surface arrays. The given distance ensures the reference is entirely by unaffected by any stimulated groundwater pumping

activity, but however is likely to share identical or very similar regolith and lithological to that of the surface array.

SP measurements were recorded previous to, during, and post groundwater pumping regimes to capture all three major aspects of resulting electrical activity including the steady state, groundwater extraction, and groundwater recovery stages respectively. Potential electrical difference measurements between the surface array (36 electrodes) and the reference (200 m distance) were recorded at 5 second intervals.

5.4 4-D tomography methods

Construction of four-dimensional tomographic models utilised previously discussed works by Hämmann et al. (1997), which was an expansion of previous works by Patella (1997a). Enhancements of these original works to a three-dimensional algorithm were modified and jointly constructed with Gard (2015). For a detailed explanation of the constructed three-dimensional tomography algorithm, refer to the previous Chapter 3, Section 3.4.2.1.

Compared with previous two-dimensional models of the EMLR SP datasets, a third-dimension provides additional depth delineation of potential electrokinetic sources. An additional fourth-dimension of time provides orderliness to an otherwise singular tomography output figure of averages or other statistical measures. Singular outputs can be dominated by, or only representative of electrical features from a singular investigation phase. These outputs may therefore consist of only relative truths, or be discriminatory to investigation phases that are not supportive of a coherent investigation outcome.

The four-dimensional tomography produced a single three-dimensional model at each one minute period of SP data available. Using various methods to establish a sites conceived electrical potential baseline, each time period represents the electrical change since baseline at that point in time. Depending on amplitude of change and pumping activity, a receding period may bear influence to its proceeding period.

5.4.1 Data filtering and processing

An overall minimalist handling and filtering approach was implemented to raw data, as the EMLR SP data was generally of a high quality and considered to be unambiguous. However, for a variety of reasons some tomography enhancing filtering or processing methods were implemented which included: cleaning of inconsistent or bad data; establishing electrical baseline of a site utilising various factors; and the use of signal amplitude change over time as a smoothness determining function.

Incorrect and faulty data can be identified as values considered extremely high or low in comparison to its surrounding electrodes values. For many reasons electrodes may also be unresponsive, and therefore not generate any data. Incorrect electrode data points were identified by implementing upper/lower data value limit filters (including NA detection). When an incorrect electrode was identified within the array, its surrounding electrodes values were averaged together to generate a filling data value entry. In the case that incorrect data occurred at the beginning or ending of a radial arm line, the incorrect data point shared the data values of its closest singular neighbouring electrode. This form of filtering was chosen versus entirely removing incorrect data values, as the latter allowed for data-absent holes that could ultimately affect the formation of the broader tomographic electrical structures.

Substantial time pre-pumping was provided to allow for electrodes to settle at an investigation site. By calculating an electrodes overall median value from its pre-pumping period data, and subtracting this resulting singular median value from each individual timestep (of each individual electrode) , a median correction was applied to each individual electrode within the array. This correction minimised localised electrode differences (in mV), providing uniformity and enhanced clarity for comparison of electrodes within the array. After correction, electrodes potential difference values could sit near 0 mV while no stimulated groundwater movement was occurring.

In the circumstances that pre-pumping phase data was not of sufficient length or stability to fairly determine a baseline signal when utilising previously discussed median methods, alternatives methods were required. To

establish baseline, a mean value of the one-minute period prior to pumping phase commencement was effective at normalising electrodes potential difference values to zero.

Inconsistent or sporadic electrical values were considered to be random unknown noise stimuli which were often undetected by surrounding electrodes of the array, and were generally considerably low in amplitude. To dampen the effects of these unknown noise stimuli, data was collated into 60-second time periods (or dimensions), and average data values were generated for each electrode within each of these time dimensions. To provide dampening of noisy electrode fluctuations across time dimensions, a rule based smoothing filter was applied:

$$SP_{N,i} = \begin{cases} SP_{N,i} , & \text{if } \Delta > 20\% \\ SP_{N,i} + SP_{N+1,i}/2 , & \text{otherwise} \end{cases} \tag{5.1}$$

where N is the N^{th} time dimension, i is the i^{th} electrode, and Δ is the difference of electrical signal between time dimensions at the same electrode. A minimum change threshold of 20% was applied, however this could be adapted for each site to best represent conditions (eg. slower pump rate, noisier electrical conditions). Threshold percentage can be altered based on target aquifer depth or general noise envelope, or adapt dynamically by input parameters including pumping phase, dimension of time in pumping phase, or even flow rate (if known). This method ensured that low amplitude unwanted noise fluctuations were further smoothed, and therefore surfaces and visible electrical structures did not drastically and unrealistically sway between time dimensions. Significantly higher amplitude signal changes, caused by non-equilibrium events such as the flow of groundwater, were allowed to pass unfiltered and therefore be distinguishable.

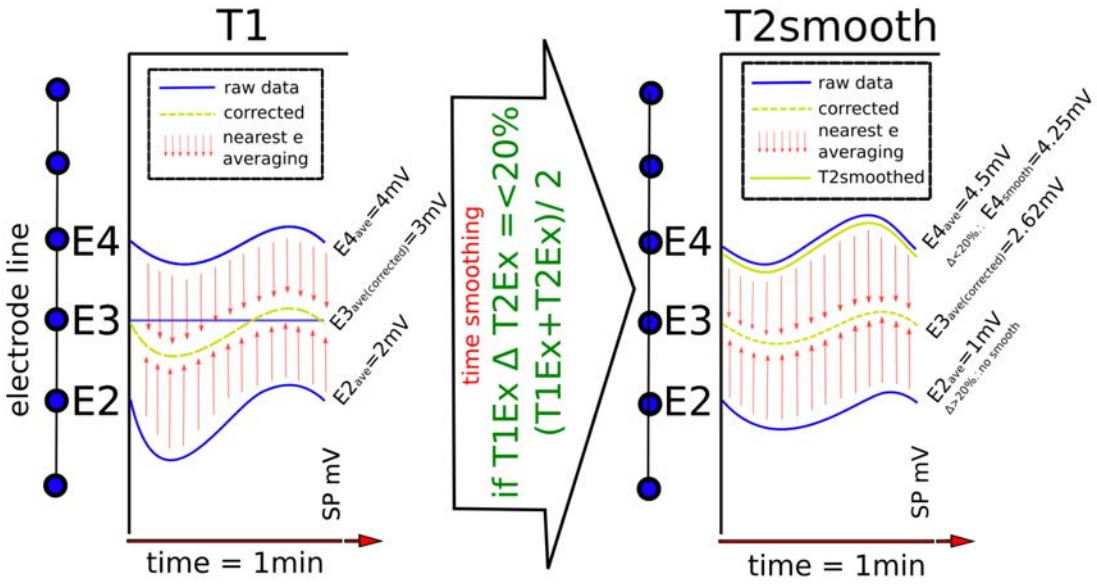

Figure 5.2: A graphical representation of the incorrect data identifier, and time-based smoothing filters for theoretical SP data. In 1-minute period T1, electrodes E2 and E4 average together to correct electrode E3, which was incorrectly recording flat data (due to bad connection). When moving forwards in time 1-minute to T2smooth, the time smoothing formula is applied to all electrode data which satisfies change less than 20% when comparing T1-raw vs. T2-raw. Subsequently within T2smooth, electrode E4 is smoothed (4 mV vs 4.5 mV = 20% change) , E3 is still corrected and calculated from surrounding E2 and E4 ($average[E2, E4] = 2.62$ mV), and E2 is unchanged (2 mV vs 1 mV $\neq$ 20%).

5.5 Results

5.5.1 Interpreting the 4-D model

A consistent presentation framework has been established to display results for each of the four selected EMLR sites that were reprocessed.

For presentation, various time periods from sites were selected that best summarises a phases conditions at its most typical (for pre and post pumping), or largest maximum or minimum electrical change points (for during or post pumping). Periods have been named based on their pumping phase conditions, and sorted downwards on page the page in chronological order of events.

Each time period slice model is presented in both a flat (birds-eye, tilt at 90°) north facing view, and as a tilt-angled and azimuth-spun three-dimensional view. The tilt and azimuth angles are adapted to best represent a models key features such as positive and negative correlation zones.

Each period slice plots a total of four colour-netted meshed layers. These layers are plotted to the surfaces of the models 80% (red lining), 60% (orange lining), 40% (yellow lining), and 20% (blue lining) overall electrical data value percentile ranks. Therefore, 80% the highest displayed electrical change in signal and 20% the lowest. These provide a consistent and comparable representation for the highest, middle ranges, and the lowest SP tomographic correlation zones. Use of more than four layers visually overcomplicated the model, and fewer layers did not provide adequate information to the viewer. As the model is an entirely three-dimensional point-source model, a user can custom select any number and range of meshed layers to be presented in the model.

The strength of likelihood a layer has a positive or negative tomographic correlation coefficient, that meaning the layer is a likely source point of electrical signal fluctuation, is determined by the layers face colour. Blue denotes a strongly negative correlation, through opaque yellows as neutrally correlated, and finally red denoting a strongly positive correlation. These strongly positive and negative colours therefore denote regions of interest which are the most likely sources of upwelling or downwelling of groundwater flowing motions respectively (Inverarity, 2014).

Because of the explained consistent framework of the electrical data value percentile ranks, all four meshes (20%, 40%, 60% and 80%) are always plotted even if there are no high or low (red or blue) electrical signal fluctuations. There just may be very little likelihood of groundwater flow this given time, and this is reflective in the colour of the layer. This allows a viewer to still consistently visualise any electrical structures of interest present in the earths.

5.5.2 Littlehampton site

Of the 21 sites completed in the EMLP region investigation, Littlehampton exhibited the highest magnitude of pumping induced change in surface electrical potential measurements. With reference to the central pumping well location, electrical potential differences peaked at a maximum of 60 mV in the north-westerly direction.

The ER normalised potential contour map in figure x provides an insight to the sites heterogenous, anisotropic resistivity distribution. With reference to the central pump, the north-westerly region from ground surface to 20 m is the most conductive at ~0.20 mV, and the south-easterly region from 20 m to 30 m the least conductive at ~0.04 mV.

In Figure 5.3, four slices of the four-dimensional model represent different key phases of the pumping cycle, including: pre-pumping (I), during-pumping (II), post-pumping (III), and the recovered phase (IV).

The pre-pumping phase (Figure 5.3, I) is in good agreement with the heterogenous ER potential contour map (Figure 5.4), where positive zones (80% percentile, red lining) in the north-west and negative zones (20% percentile, blue lining) in the south-east fall within the most and least conductive zones respectively. The face colours represent a neutral tomographic correlation coefficient, as pumping is not occurring during this phase.

Within the during-pumping phase (Figure 5.3, II), the site experiences change towards negative tomographic correlation coefficient due to the expected electrical drainage effects. Shallow, near surface drainage is experienced across the whole site, although a highly anisotropic drainage shape develops as the strongest negative tomographic correlation occurs in the north-west zone. The negative structure extends from near surface at roughly 5 m depth, curling and dipping at a near 90° into the earth, and out of the model beyond 20 m in depth. As previously mentioned, the north-west zone was notably highly conductive. Based on supporting results of the two methods, it is probable that this north-west zone of increased conductivity was as a result of increased groundwater saturation (rather than heterogenous bedrock or regolith), and that the zone is a preferred groundwater path towards the pumping well.

During post-pumping phase (Figure 5.3, III), the groundwater recovery process does not exhibit any high strength tomography correlation zones. A low strength positive correlation zone can be seen across most of the whole eastern half of the model, and is likely a result of slow near surface recharge occurring where previous near surface drainage occurred. No obvious recharge features can be seen in the north-west zone (previously high strength negative tomographic correlation). Due to proximity from surface electrodes, near surface groundwater flow is more readily detected than flow at depth.

Pumping recovery phase (Figure 5.3, IV) shows the site returns to a near identical electrical state from previous to the pumping. The site recovers groundwater rapidly in contrast to other investigation sites within the EMLR, as generally most sites never returned to their pre-pumping phase electrical state before recording was stopped.

The presented ER contour map and tomographic correlation maps overall are in good agreement concerning the potential structures and locations of major hydraulically active fractures or bedding plane zones.

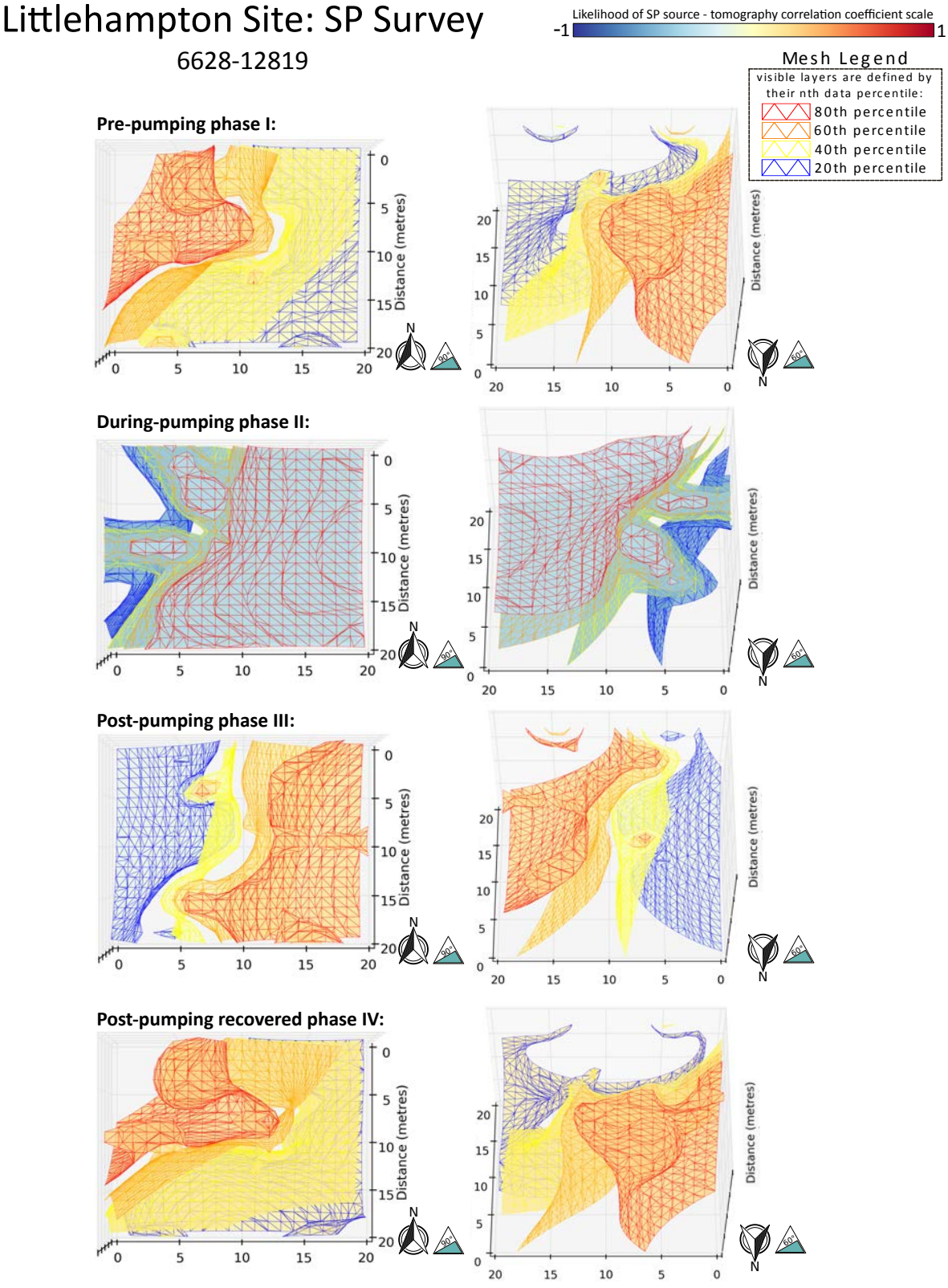

Figure 5.3: Four-Dimensional tomography results of the Littlehampton Site, EMLR region. Four netting-colours and their surfaces positions represent percentile rankings and spatial positions of a tomography datasets values during each gien phase. Colours of surfaces represent the regions likelihood of hosting an SP anomaly source. SP data sourced from Zulfic et al. (2008).

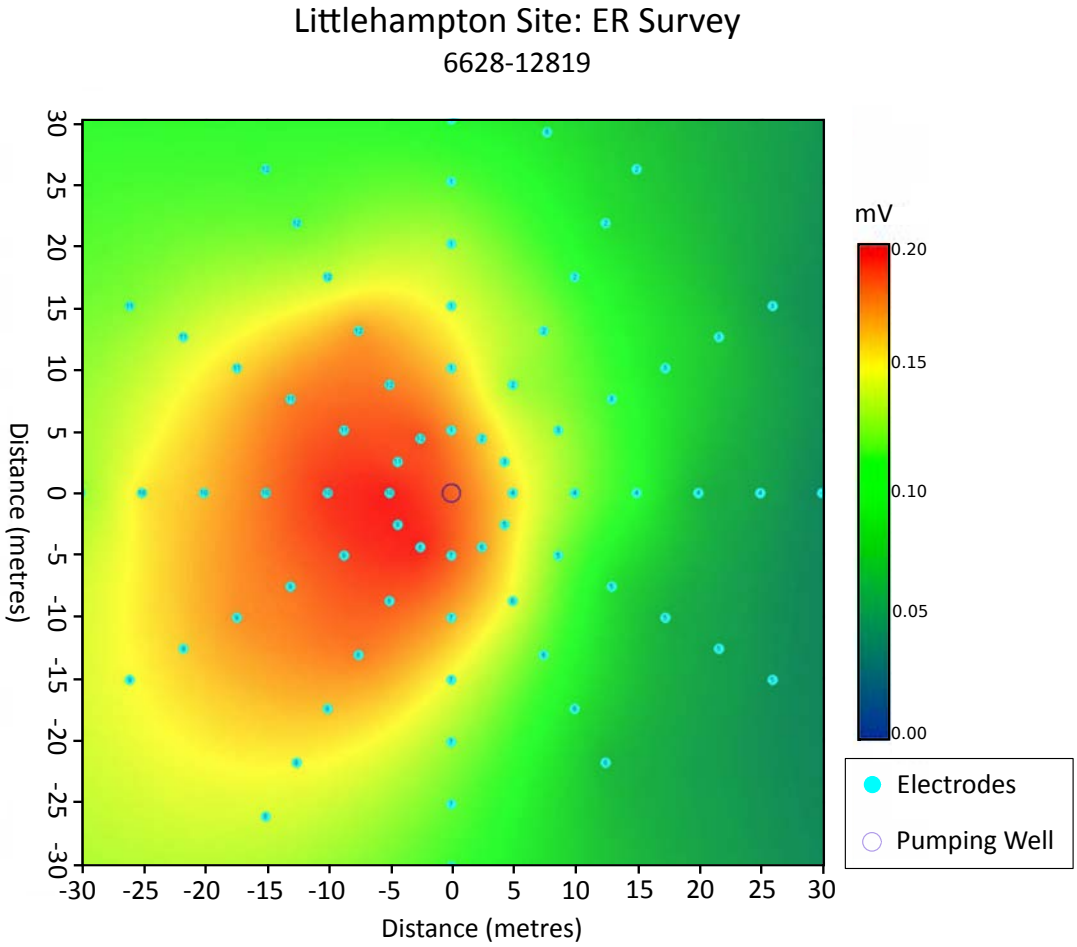

Figure 5.4: At Littlehampton Site, EMLR region, a normalised potential distribution contour map from a borehole-to-surface DC electrical resistivity survey. Reworked from original figure by Zulfic et al. (2008).

5.5.3 North Mt.Barker site

The North Mt.Barker site exhibited only minute voltages change, in the order of ~0.3 mV. The ER normalised potential contour map in Figure 5.6 show that the conductivity distribution is isotropic and symmetrical. A higher potential contour region of ~0.6 mV surrounds the central pumping well, which gradually reduces moving outwards from the pumping well in a concentric pattern towards ~0.05 mV.

In Figure 5.5, four slices of the four-dimensional model represent different key phases of the pumping cycle, including: pre-pumping (I), during-pumping (II), post-pumping (III), and the early recovery phase (IV).

Pre-pumping phase (Figure 5.5, I) exhibits a uniform flat distribution across the whole site. All four percentile layers are flat, with no apparent heterogenous electrical features at depth.

During-pumping phase (Figure 5.5, II), the uniform nature of the earlier pre-pumping phase follows through. All six radial arms exhibit very similar high strength positive tomographic correlation coefficients. As the potential electrical difference signal is quite week (maximum change of $0.3mV$), the groundwater movement is likely to be at some depth rather than near surface. The model shows the highest positive tomographic correlation layer (80% percentile layer) at a depth of $/sim$15 m, dipping at approximately 20° west.

The post-pumping phase (Figure 5.5, III) show strong negative tomographic correlation coefficients likely as a result of groundwater recovery processes. Although the previous during-pumping phase showed the highest positive tomographic correlation layer dipping 20° west, the highest negative layer now dips 10° east. Over the pumping phase, the dip gradually moves from a positive westerly dip, to a negative easterly dip. This would be characteristic of drainage and flow towards the pump well initial moving from the western groundwater zone, but latter aquifer recharging occurring at depth from the east (relative to the central pump) . When dealing with such a low voltage amplitude of change (0.3 mV), further investigation would be required to more effectively evaluate the aquifer and groundwater conditions.

At the recovery phase (Figure 5.5, IV), moderate strength negative tomographic correlation zones still exist in central-west and central southwest zones of the site. This is consistent with the deeply underlying high strength tomographic correlation in the western region of the previous earlier post-pumping phase (II) model . A full recovery to a pre-pumping phase state was not evident before recordings end.

The ER map (Figure 5.6) and tomographic correlation maps (Figure 5.5) are overall in good agreement with regards to the symmetrical, isotropic

distribution of groundwater flow at the site. Of particular interest within the tomographic correlation maps are the dipping structures at depths below ~15 m. However, due to low surface voltage changes (0.3 mV) and this being within reasonable environmental/instrument noise range, further self-potential pump testing would be required. Repeating of the same pumping testing would allow results to be stacked and subsequently noise minimised, further increasing model confidence.

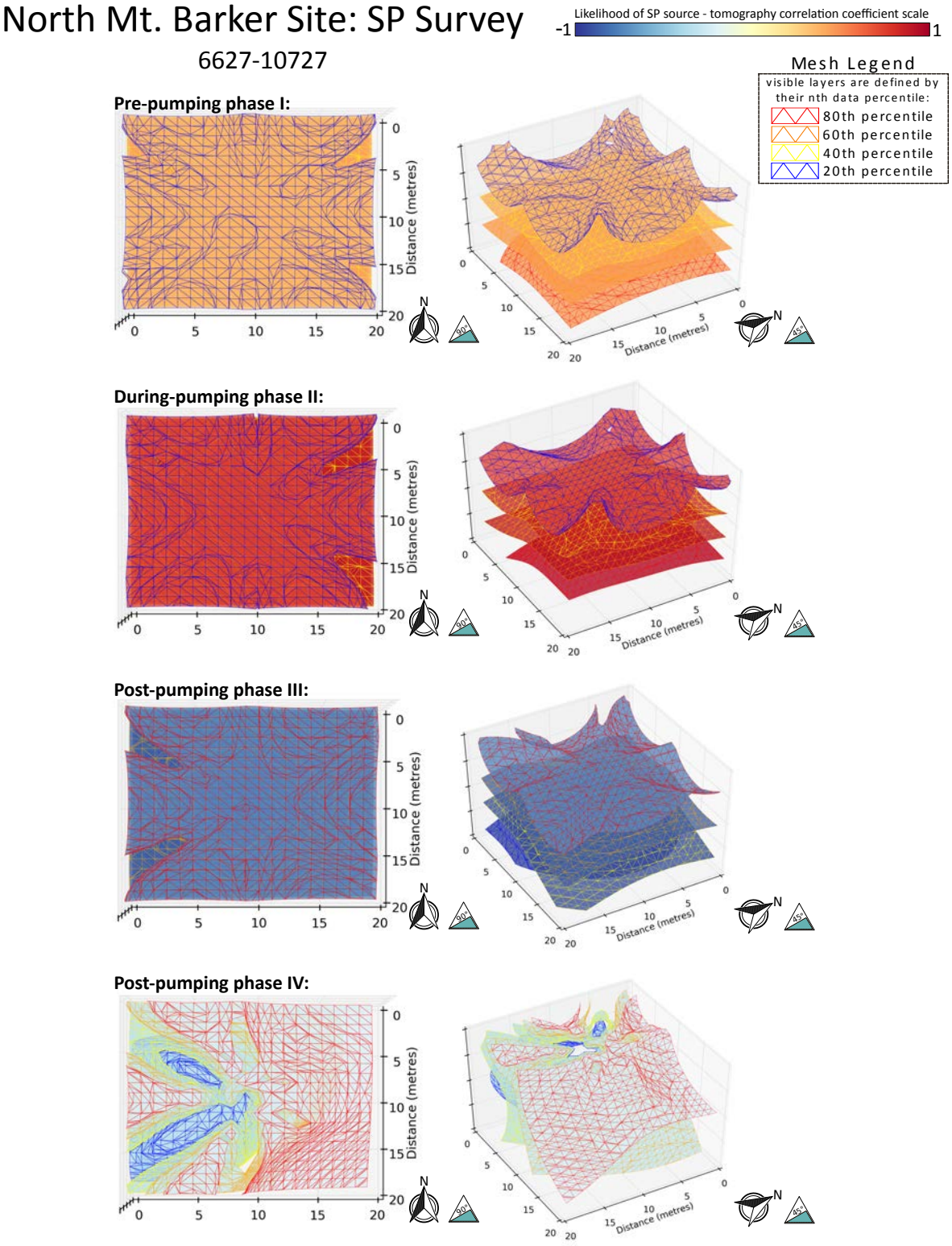

Figure 5.5: Four-Dimensional tomography results of the North Mt.Barker Site, EMLR region. Four netting-colours and their surfaces positions represent percentile rankings and spatial positions of a tomography datasets values during each gien phase. Colours of surfaces represent the regions likelihood of hosting an SP anomaly source. SP data sourced from Zulfic et al. (2008).

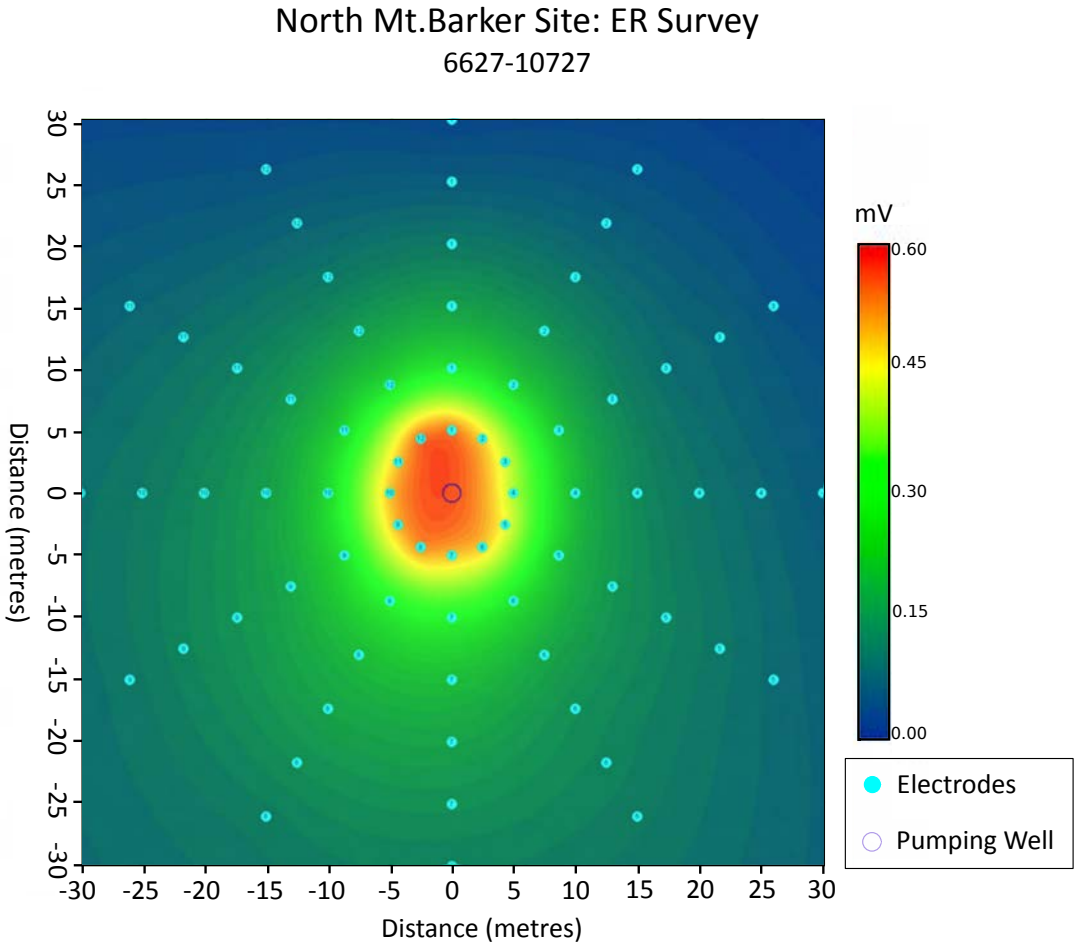

Figure 5.6: At North Mt.Barker Site, EMLR region, a normalised potential distribution contour map from a borehole-to-surface DC electrical resistivity survey. Reworked from original figure by Zulfic et al. (2008).

5.5.4 East Echunga site

The East Echunga site exhibited a maximum potential difference voltage change of 4 mV during pumping. The ER normalised potential contour map in Figure 5.8 shows conductivity distribution is uniform and isotropic. A higher potential contour region of ~2.3 mV surrounds the central pumping well, which gradually reduces moving outwards from the pumping well in a concentric pattern towards ~0.7 mV.

In Figure 5.7, four slices of the four-dimensional model represent different key phases of the pumping cycle, including: pre-pumping (I), during-pumping (II), post-pumping (III), and the post-pumping recovery (IV).

Pre-pumping phase (Figure 5.7, I) exhibits 90° boundaries splitting the high and low percentile layers. This shape is likely influenced by localised differences in resistivity.

During-pumping phase (Figure 5.7, II), the site experiences a change towards negative tomographic correlation due to expected electrical drainage effects. Shallow, near surface drainage is experienced across the whole site, however a highly anisotropic drainage shape develops in the north-east. The negative structure extends from near surface at roughly three metres depth, dipping at 70° towards the pumpwell, and out of the model beyond 20 m in depth.

Post-pumping phase (Figure 5.7, III) soon after pumping is halted shows tomographic layers revert to an almost exact pre-pumping phase state. It should be noted that the high (80%) and low (20%) layers have switched places, and this is likely due to the commencement of groundwater recovery.

Post-pumping recovery phase (Figure 5.7, IV) reveals the commencing stage of a full groundwater recovery. Highly positive tomographic correlation zones can be seen in the north-east region, mimicking where the previous negative tomographic correlation existed within the during-pumping phase.

The ER map (Figure 5.8) and tomographic correlation maps (Figure 5.7) are overall not in good agreement. The ER map reveals the site to be mostly isotropic, and tomographic correlation mapping during pre (I) and post-pumping (II) phases reveal anisotropic conditions likely exist, with preferred flow orientation in a north-east direction both near surface and at some depth.

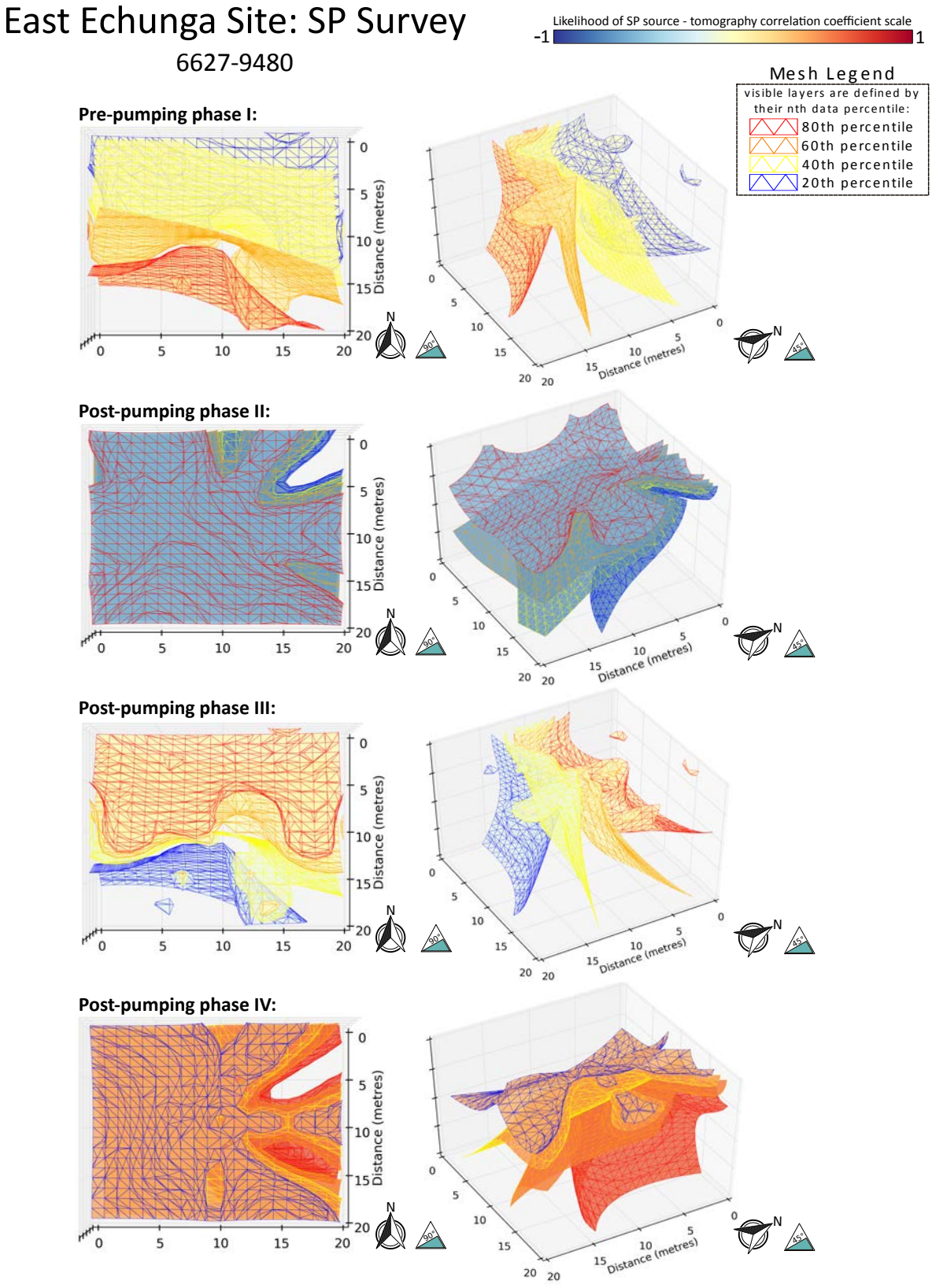

Figure 5.7: Four-Dimensional tomography results of the Ecnunga site, EMLR region. Four netting-colours and their surfaces positions represent percentile rankings and spatial positions of a tomography datasets values during each gien phase. Colours of surfaces represent the regions likelihood of hosting an SP anomaly source. SP data sourced from Zulfic et al. (2008).

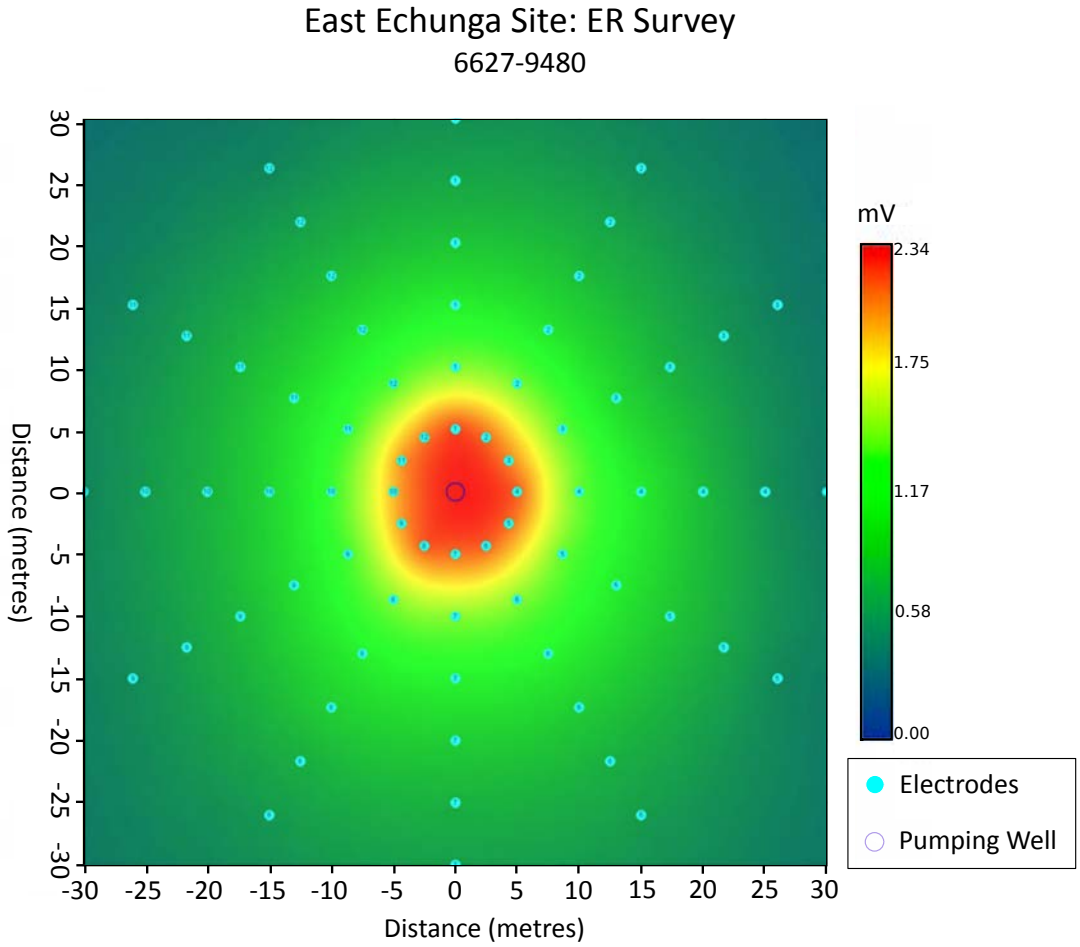

Figure 5.8: At Echunga Site, EMLR region, a normalised potential distribution contour map from a borehole-to-surface DC electrical resistivity survey. Reworked from original figure by Zulfic et al. (2008).

5.5.5 East Nairne site

The East Nairne site exhibited a maximum potential difference voltage change of 7 mV during groundwater pumping. The ER normalised potential contour map in Figure 5.10 shows conductivity distribution is uniform and isotropic. A higher potential contour region of ~3.5 mV surrounds the central pumping well, which gradually reduces moving outwards from the pumping well in a concentric pattern toward ~1.0 mV

The East Nairne model evaluation in Figure 5.9 is presented in a slightly varied format to previous site models. The four slices of the four-dimensional model represent different key phases across two consecutive pumping tests conducted: first during-pumping (I), first post-pumping (II), and second during-pumping (II), and second post-pumping (IV).

As a result of groundwater drainage, the first during-pumping phase (Figure 5.9, I) exhibits a high strength positive tomography correlation coefficient. The distribution is highly uniform across the site, with all layer surfaces near completely flat. The highest likelihood of self-potential signal strength originates from the 80th percentile layer (red) at ~18 m depth.

The first post-pumping phase (Figure 5.9, II) captures the groundwater relaxation process occurring. The strength of tomographic correlation reduces to an intermediate level, potentially indicating a slower groundwater refill and relaxation process. Alike to the previous phase (I), distribution of the layers are highly uniform, and all layer surfaces remain near flat.

The tomography signal strength of the second during-pumping phase (Figure 5.9, III) is comparable to that of the previous during-pumping phase (I) at near surface depths. However, at depth some non-uniform electrical structures begin to take shape. The highest strength layer forms in the deeper eastern region of the site. Beginning at ~10 m depth, and dipping at ~45° towards the pump well (west), the layer exits the site model at the 20 m depth boundary almost directly below the central pump-well location.

The second post-pumping phase (Figure 5.9, IV) still maintains a prominent, non-uniform electrical structure originating from the deeper eastern region. The structure has both shifted further east, and is now shallower at ~5 m depth from surface.

The ER map (Figure 5.8) and tomographic correlation maps (Figure 5.7) are overall not in average agreement. The ER map reveals the site to be slightly heterogeneous in a north-west to south-east direction, and tomographic correlation mapping during pumping (III) and post-pumping (IV) phases reveal homogeneous flow or recharge conditions likely exist from an eastern direction.

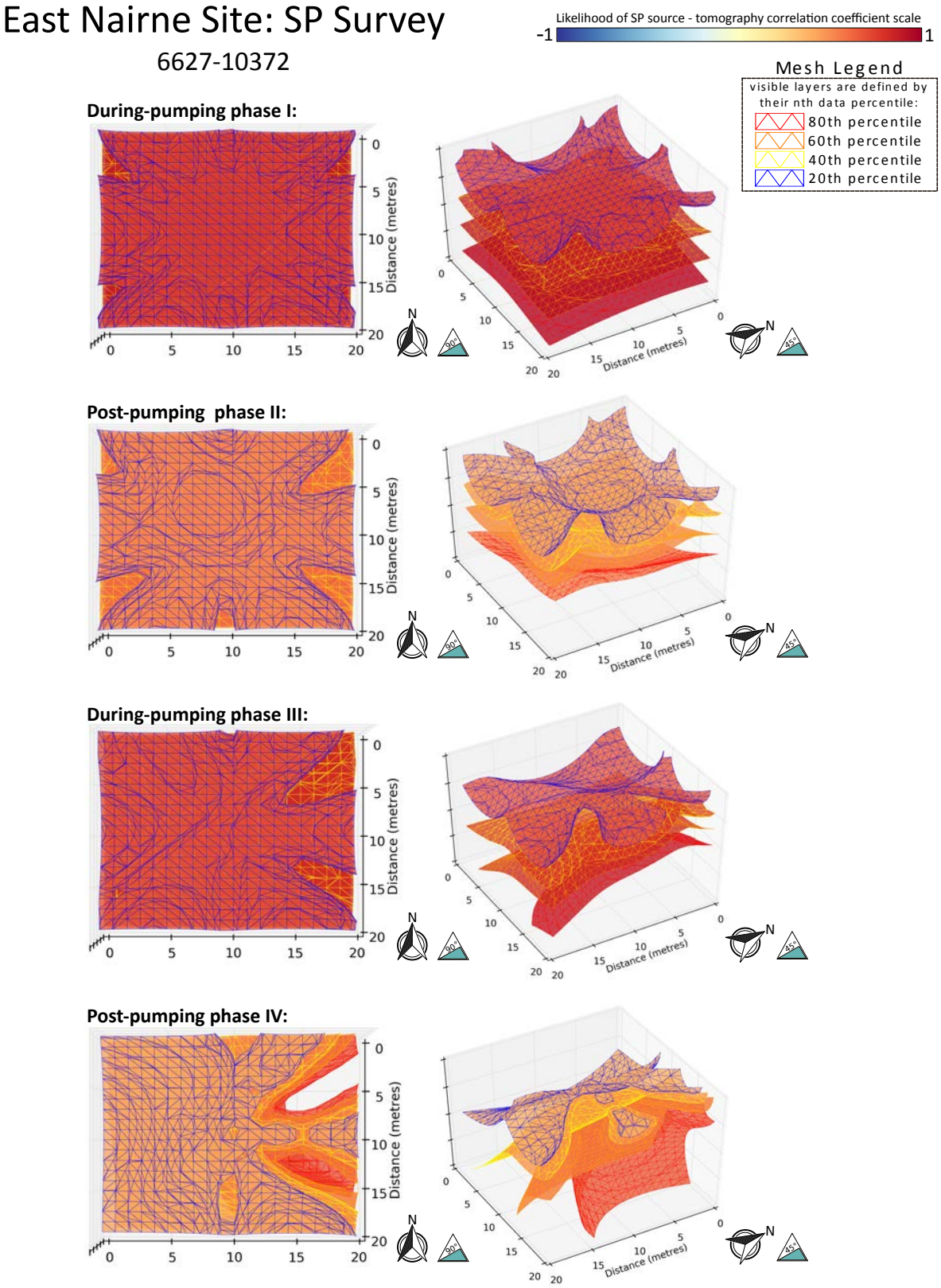

Figure 5.9: Four-dimensional tomography results of the East Nairne site, EMLR region. Four netting-colours and their surfaces positions represent percentile rankings and spatial positions of a tomography datasets values during each gien phase. Colours of surfaces represent the regions likelihood of hosting an SP anomaly source. SP data sourced from Zulfic et al. (2008).

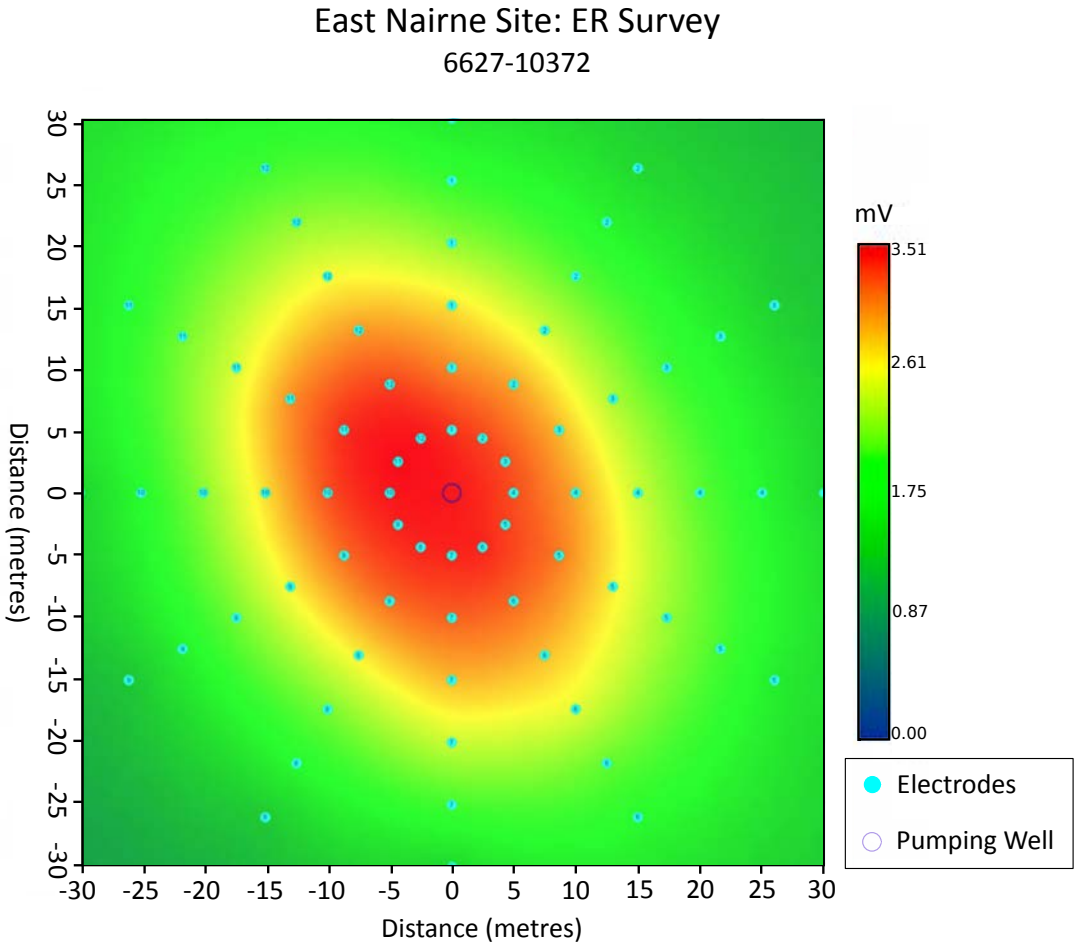

Figure 5.10: At East Nairne site, EMLR region, a normalised potential distribution contour map from a borehole-to-surface DC electrical resistivity survey. Reworked from original figure by Zulfic et al. (2008).

5.6 Conclusion

In comparison to two-dimensional or three-dimensional tomography, analysis utilising four-dimensional methods significantly enhances detectability and migration patterns of even subtle changes within a field sites subsurface electrical structures - in particularly for electrical structures at depth which could otherwise go unnoticed. The inclusion of a continuous time-dimension yield results less amenable to overfitting, and avoids oversimplification of results to a singular output. Results can therefore be interpreted with a higher level of confidence.

As the frame by frame tomography slides can be understood with some relative ease and are immensely visually appealing, a complete pumping event tomography time series can be provided for viewing to any commercial stakeholders associated with the investigation.

Regarding future work and possible improvements to filtering techniques of the four-dimensional tomography method: Just as we monitor an electrodes change in signal across time dimensions to minimise ambiguous noise (refer to Formula 5.1), alike to the incorrect data identifier (refer Figure 5.2) the presence and amplitudes of signal changes for electrodes neighbouring or near (spatially) one another within an array could be treated as an additional measure of noise or signal confidence to implement additional filtering rules. Due to factors including distances, and consistent and inconsistent heterogeneities between array electrodes, the overall methodology and extremity of filtering effects would have to be explored further in some detail

CHAPTER

SIX

NEURAL NETWORK SELF-POTENTIAL METHODS

6.1 Introduction

The past decade has seen a rapid expansion in the research and application of artificial neural networks (ANNs) to a wide range of industries, including geophysics. The networks can be applied as universal approximators to any continuous function with an arbitrary precision, and consequently have the ability to yield important contributions to a variety of geophysical applications (Baan and Jutten, 2000). The impetus behind the growth has been the method's ability to offer solutions not amenable to conventional techniques, in particularly domains involving pattern recognition, prediction and control (Sandham and Leggett, 2013).

Across the discipline, ANNs and fuzzy logic are already employed routinely in earthquake and seismic exploration seismology (Murat and Rudman, 1992; Wang and Mendel, 1992; He and Zhou, 2003), electromagnetic and potential field research (Poulton et al., 1992; Sandham and Leggett, 2013), and geophysical data inversion (Zhang and Paulson, 1997; Baddari et al., 2009).

Larger quantities of data are being collected due to increased software and hardware availability and capabilities, increased instrument sampling

rates and number of data channels, and the emerging trend of three and four dimensional modeling. We require more efficient techniques to better process large data volumes, and a subsequent review of how to more effectively utilise all available data versus the common practice of omitting undesirable data.

6.1.1 What are neural networks

The artificial neural network was conceived by McCulloch and Pitts (1943) to mathematically mimic the behaviour of a biological neuron for means of information processing.

In a simplified explanation, a biological neuron receives an input signal from several other connected neurons. Several inputs are attenuated via temporal and spatial variation from previous neurons to generate an information output. This output signal is further transmitted to other neurons and the input, attenuation and output process is continued until a goal (eg. body movement, thought processing) is achieved (Baan and Jutten, 2000).

The mathematical neuron is similar, whereas the attenuated weighted sum of previous neuron's inputs is processed by a non-linear transfer function (i.e. activation function) for further scaling. Therefore, each neuron is behaving as a simple logistic regression process along a chain. A constant bias independent of signal input is also applied to allow shifting of the transfer function from a central point. Without bias, a function will always attempt to fit through the origin, and subsequently may have a poorer fit to data.

There are many types of artificial neural networks available with varied network architectures, activation functions, learning structures and specific performance outcomes ideal for varying approximation situations. For additional information regarding general background and introduction to a diverse range of neural networks, refer to the book Neural Network Design, written by Demuth et al. (2014).

6.1.2 Recurrent neural networks

As the latter part of this thesis utilities and presents recurrent neural network data processing techniques, only this particular class of artificial network will be discussed.

A recurrent neural network is a class of network where connections between neurons can form a multi-direction cycle, allowing for data to flow both forwards and backwards from neurons and therefore generating one or more feedback loops. Feedback loops are a key regulatory motif in many biological systems and act much the same in neural networks (Dong et al., 2012). Positive or negative feedback loops are used to determine the required quantitative changes required for a more precise data fit. As neurons in RNNs form these directed cycles, an implicit internal memory of a dataset is formed. This internal memory gives them the ability to naturally take time into account, and hence RNNs are adapted to problems dealing with signals evolving through time. Valuable approximation results can be obtained for these dynamic systems (Boné and Cardot, 2011). RNNs constitute a very powerful class of computational models, capable of instantiating almost arbitrary dynamics (Gers and Schmidhuber, 2000)

Just as there are several classes of neural network, there are also several architectures of recurrent neural networks. The Long Short-Term Memory (LSTM) (Gers et al., 2000) is a recurrent neural network that is well suited to classification, processing and prediction problems. LSTMs can store values for long or short time periods, can function with long temporal delays in datasets, and can handle a mix of both low and high frequency components.

6.1.2.1 Training neural networks

Several methodologies exist which can be used to train a neural network for various learning goals, but the most commonly utilised are both supervised and unsupervised learning processes.

Supervised learning, which is utilised in this chapter, requires labelled examples as training data to make predictions for unseen points. A labeled example is a pair consisting of an input object, and a desired output value to the input. This technique produces an inferred understanding of relationships or more complex functions, and is the most commonly

used training technique for classification, regression and ranking problems (Mohri et al., 2012a). Unsupervised learning uses unlabelled training data where a desired output value is unknown, and predictions are made for unseen points. This learning method is commonly used for clustering and dimensionality reduction problems (Hinton and Sejnowski, 1999). Further discussion of network training and learning scenarios can be found within Mohri et al. (2012b) textbook: Foundations of Machine Learning. Supervised learning can be optimised using a stochastic gradient descent approach, a first order iterative optimization algorithm for minimising the loss function. Backpropagation through time (BPTT) (Mozer, 1989) is used to calculate the error contribution of each neuron after processing data, where the learned error is then re-distributed back through the network's neurons. This process is continually repeated to further minimise loss between the prediction and labeled training data.

6.1.3 Applications SP research

ANNs are used widley within both the science and geophysics communities; its uptake within SP research is less developed. ANN methods have been successfully applied to the interpretation and inversion of buried SP anomalies for both synthetic and real datasets (Al-Garni, 2010; Kaftan and Akdemir, 2014). In these studies, a synthetic data training set was produced and used to teach an ANN how to best characterise and invert a two-dimensional anomaly profile for a spherical anomaly at a point. Resulting performance of these models show good agreement with traditional least squares inversion techniques.

To date, the use of any ANN technique has not been implemented in any format of SP groundwater investigation research; this includes both signal interpretation and inversion techniques. Successful ANN methodologies proposed by Kaftan and Akdemir (2014) could be replicated and applicable to pumping scenario groundwater investigations. Adapted only slightly by taking into account an additional dimension of time, the methodology could profile anomalous SP generated by groundwater movement within selected time periods and draw comparison over time. Although a seemingly ideal adaption, unfortunately the anomalous SP signal gradients when mapping groundwater movement are generally far lower amplitude than those of large buried anomalous bodies. As also previously discussed, it

is difficult in field conditions to have a time constant stabilised SP signal. Many factors contribute to a time fluctuating SP signal, further complicating the definition of identifying pumping induced anomalous features.

6.2 Aims

This chapter will explore the feasibility of novel ANN techniques proposed for medium to long duration (beyond one week) SP groundwater pumping investigations, and application of environmental noise handling techniques for SP surveying that can also be applicable to a broad range of surface electrical geophysical data collection processes.

First, we have attempted to train an ANN to recognise the existence of stimulated groundwater movement due to pumping processes, using only surface SP signals as an input. In comparison to previous work by Kaftan and Akdemir (2014) which synthetically generated training sets to replicate expected electrical physical properties of earth, our training set is a real two week SP dataset.

Utilising relevant pumping well data logs for labeling, the first one week of real SP data was used to produce a training dataset classified into two categories: no pumping occurring (0), or pumping occurring (1). With this classified training set, the ANN was tasked to learn the typical SP surface array response during these pumping or no pumping periods. The ANN applies these learnings by predicting the likelihood (ranging between 0-1) that pumping was in fact occurring at each given point in time (1 second periods). The ANN inspects fit of output likelihood predictions to the known classified data, therefore allowing it to continually adjust and improve on its previous predictions.

Secondly, using ANNs we have attempted to deconvolute unwanted environmental noise signals from our SP data set. Utilising accurate weather station data obtained from the Australian Bureau of Meteorology, magnetic data from the Geoscience Australia Alice Springs observatory, and on-site automated pumping well data logs, we analysed the contributing effects these variables could be having on our SP dataset results. The principal theory behind this was that although these given environmental variables are more or less consistent across all stations, inevitable variances exist between the distant reference electrode and points in the array,

and these variations would be somewhat expressed within the SP data set. From the full length 43 day SP dataset recorded at the site, six evenly spaced Petiau style electrodes were chosen to represent stable variations of electrical potential signal within the surface array. Again, the data was split in two components: half was used as labelled training data, and half as validation data. For the training process, the ANN was supplied with both the actual SP data from the six representative surface electrodes, and the time matched corresponding 12 environmental variables. Post training and learning processes, and utilising only the 12 environmental variables as input, the ANN was tasked to predict the most likely real SP data set values of the six surface electrodes. A comparison of the predicted SP versus actual SP can then be made to identify and validate if the environmental variables could be responsible for any underlying trends or discontinuities. This form of noise to signal 'reverse engineering' can be a both practical and powerful quantitative or qualitative noise reduction tool that will be explored further in the upcoming discussion segment.

6.3 Site information

On the 21st of December 2016, a self-potential monitoring array was established at the Morphettville Race Course, South Australia. The site is one of many national locations involved in a government initiative Managed Aquifer Recharge Scheme (MAR). The MAR process begins with the capture of surface rainwater, in Morphettville's scenario this is via the use of an artificial wetland, which is then slowly filtered through natural plant reedbed processes. After filtering occurs, the clean water is extracted from the wetland and pumped downwards into a storage aquifer for future use. Locally, the scheme allows excess winter rainfall to be pumped back into the aquifer, which during summer months the Morphettville racecourse uses to irrigate the grounds. The array was left to record electrical potential difference above the MAR aquifer until the 2nd of February 2017, for a total period of 43 days.

6.3.1 Instrument layout

A surface array of 48 electrodes were used to measure changes in the electrical potential field as a result of MAR scheme groundwater extraction pumping at the Morphettville Racecourse site. The array was comprised

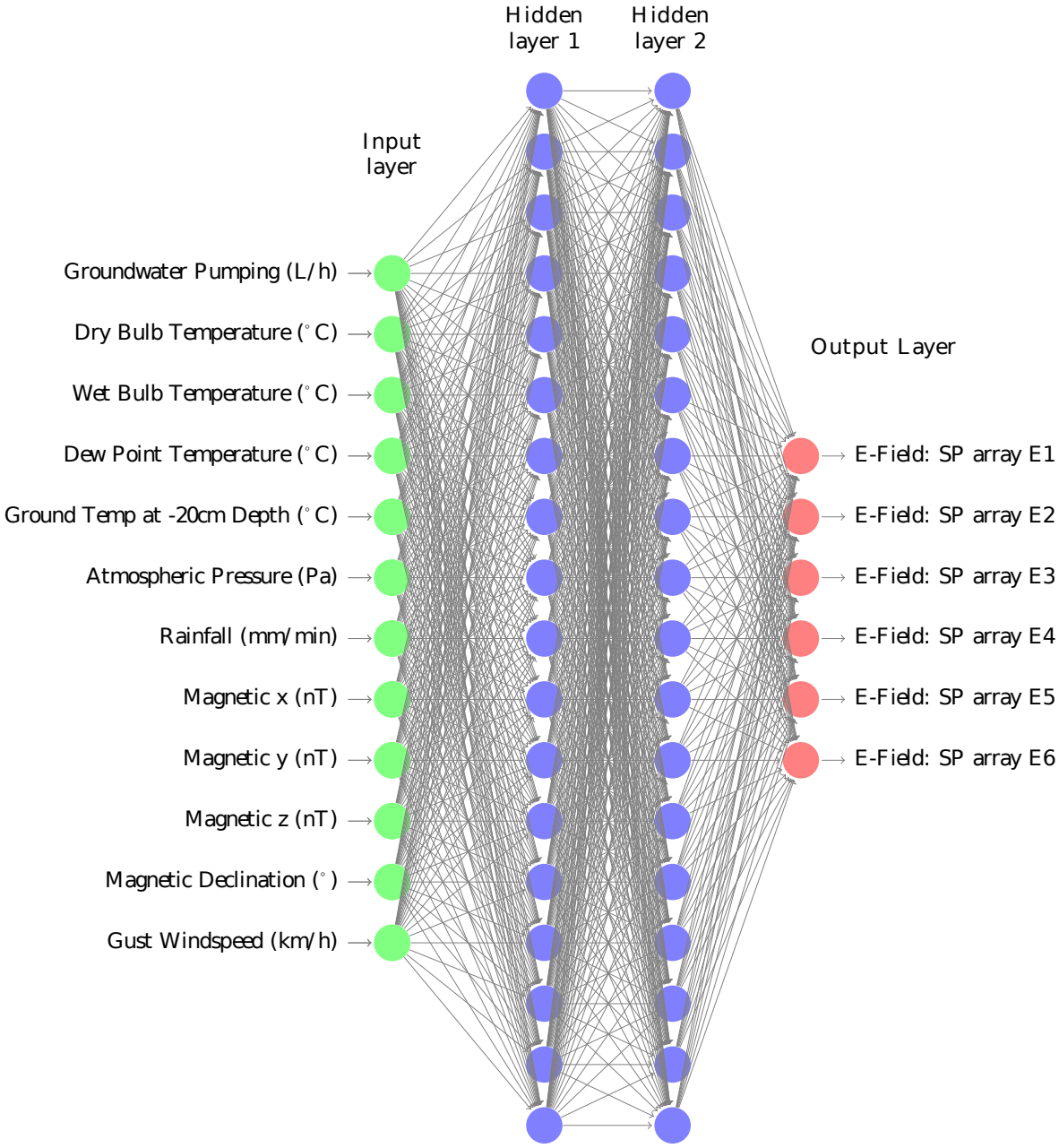

Figure 6.1: A visualization of the recurrent artificial neural network. 12 datasets, including pumping well hydraulic head, environmental and magnetics are fed into the input layer of the model. Considered as a regression problem, all input datasets are treated as a shared function of the six labelled real surface SP signal datasets used to train the network. Neurons within the two hidden layers of the ANN form directed cycles where an implicit internal memory of the datasets is formed. The six output models are the resulting theorized surface SP datasets, constructed by the ANNs learned function of all the inputs combined influences during regression analysis of the real SP data training set.

of four straight lines, each of which hosting 12 electrodes. Lines 1 through 4 ran at 240°, 250°, 260° and 270° respectively. Orientations of the lines

Figure 6.2: Stormwater aquifer storage and recovery (ASR) scheme locations around Australia. In South Australia ASR schemes supply approximately 20 GL/yr of groundwater recharge. Recharge estimations of 60 GL/yr are expected by 2050. Figure from CSIRO: Managed aquifer recharge scheme (2017).

were hindered by landscape features such as the artificial wetland, car access tracks, and on-site machinery. Spacing between electrodes along a line was uniform at five metres. Electrode one on each line began closest to the pumping well, beginning at 10 m from the location of the pumping well.

Of the 48 electrodes used, 36 were iron based, zinc galvanized alloy electrodes, and 12 were non-polarizing Petiau style $PbPbCl$ electrodes. Three Petiau electrodes were evenly distributed across each of the four lines at electrode positions three, six, and nine. A shared reference electrode was buried approximately 150 m south-east from the pumping well.

Drawdown and groundwater flow rates were monitored by previously established measuring devices within the main pumping well; time stamped outputs of CSV files were collected and used to determine periods of potential SP activity. The pumping well (SA water unit number 6628-21045) has a maximum depth of 75 m, and has a high flow capacity of 40 L/s. The well

draws from the Adelaide T1 porous media aquifer, comprised of mainly interbedded limestones, sandstones and fossiliferous sands (DEWNR, 2016).

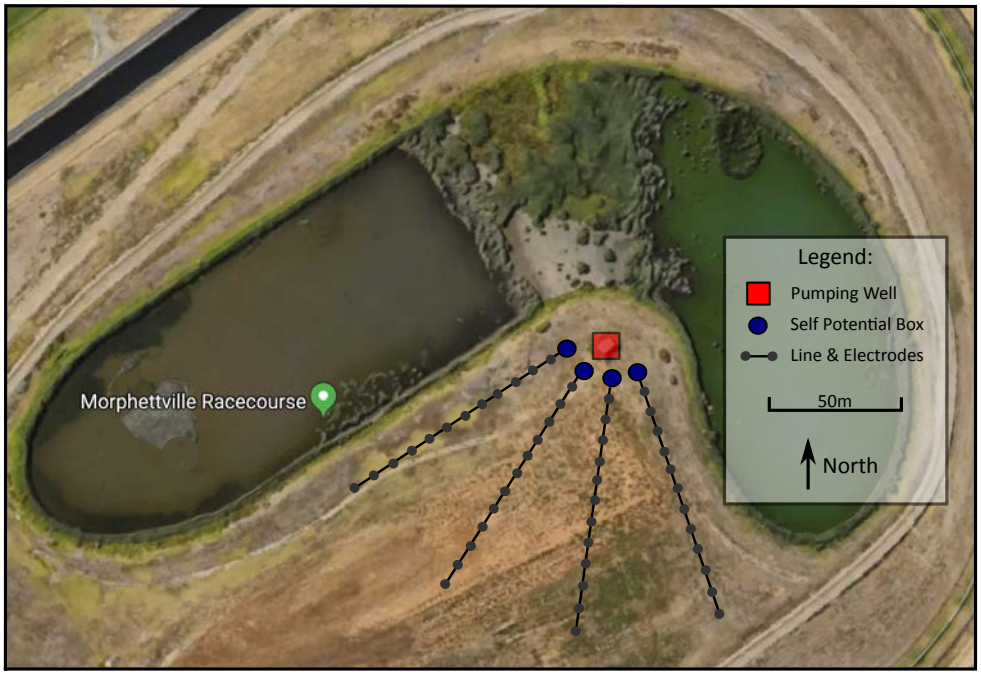

Figure 6.3: A satellite image map of the Morphettville racecourse managed aquifer recharge site. Four self-potential loggers and lines collected one-second data along 48 electrodes. Electrode locations began 15 m from the central pumping well, spanning outwards in straight radial arms at a spacing of 10 metres between electrodes.

6.4 Datasets

All datasets recorded, obtained and utilised for ANN learning processes from the entire 42 day investigation period can be viewed in full at Figures 6.4 and 6.5.

6.4.1 SP dataset

SP data obtained from the described surface array of 48 electrodes all referenced to a shared singular electrode approximately 200 m from the central pumping well. This was the maximum reference distance obtainable due to both the sites layout, and restrictions imposed due to the operational requirements of the racecourse. Data obtained by the iron based, zinc gal-

vanized alloy electrodes were considered to be of average quality. These electrodes data were greatly compromised by noise and sporadic drift effects. Due to the sites urbanised location and the high frequency nature of the signal, encountered noise was likely due to anthropogenic sources. All collected data was filtered with a 60 second median low-pass filter, mainly to minimize effects of anthropogenic noise.

One objective of this project was to identify electrokinetic phenomena induced by groundwater flow from the MAR schemes pumping activity. Using this data we could make inferences of the aquifers permeability and preferential flow pattern. Whilst the electrokinetic signal from pumping was captured during some instances, these low-amplitude signals were only detectable during early morning hours in the absence of solar effects and several environmental effects. Electrical data collected during sunlight hours were not capable of detecting SP anomalies. Low-pass filtering methods where utilised, however the low amplitude SP signals and remaining noise patterns could not be effectively and consistently decoupled.

A long data collection period of 43 days introduced further complication regarding inconsistencies in detectable amplitude and spatial patterns. During pumping, the array would often produce inconsistent SP anomalies that did not allow for repetitive amplitude and spatial patterns to be recognizable. As discussed previously in Section reffieldsiteconditions, in conductive Australian conditions where electrical signal to noise ratio is an issue, repeatability is crucial for eradicating noise that can be erroneously interpreted as SP signal. Often is the case in SP research, due to time and expense constraints, that only singular (or one day) pumping events will be conducted. Repeatability of results is often therefore unquestioned, and returning or repeating scientific studies will bear a burden of unreproducible results.

6.4.2 Additional datasets

From the central pumping well, automated logs of flow rate and water level (hydraulic head) were obtained. Hydraulic head generally rested at approximately 22 m depth, and while pumping was occurring at flow rates of 28-35 L/s, hydraulic head fell to approximately 17 m. Post groundwater extraction, the aquifer would recover to its original 22 m depth generally

within 15-30 minutes. Days of heavy surface precipitation (53.2 mm on 23/12/2016) did not have any effect on hydraulic head level.

Minute value magnetic X, Y, Z and Declination data was acquired from Geoscience Australia at the nearest observatory in Alice Springs. From the Bureau of Meterology, minute values of air temperature, wet bulb temperature, ground temperature at 10 cm depth, rainfall (mm/min), dew point and humidity, wind speed max and atmospheric pressure were obtained from the Adelaide Airport weather station. This weather station is only approximately 3km distance from the site.

6.4.3 Preprocessing of datasets

The important factors regarding most effectively training an ANN are data cleansing, preprocessing techniques, and the architecture and optimization decisions. Decision making in these regards follow a somewhat standardised practise for cleansing and preprocessing of data, although architectural and optimization decisions are determined by factors including: aim and perceived complexity of the task, dataset sizes, computational capacity, the leading and most current software tools available, and finally a great deal of trial and error.

Regarding preprocessing, some both standard and non-standard techniques were used to achieve a best result: All input values amplitudes were refactored to between 0 to 1, and data points considered as outliers (eg. 55mm over 6 hours) were suppressed as to not cause over-dampening of the entire input. Preprocessing of the labelled surface SP data was also required, and as was the case with external inputs these where also refactored. Once refactored, a 'difference of previous timestep' approach was utilised: Each one second value was subtracted by the previous one second value, therefore each one second value consisted of only the change in SP signal. This technique abolished the ANNs consideration of static signal difference (between array electrodes and their grounding electrode) being of any significance to its learning aims, as well as minimising the effects of continual very-slow electrode drifting effects. This simple preprocessing technique proved to be the most effective tool for improving the learning capabilities and therefore quality of predictions from the ANN.

Comparing results during trial and error processes, it was evident the differencing preprocessing technique greatly improved the learning capabilities, and therefore quality of predictions from the ANN process. The ANN could more effectively recognize and relate external inputs to electrical fluctuations

6.5 Results

6.5.1 Categorising pumping events

The first of two proposed ANN techniques utilised only the surface array SP dataset and the pumping well hydraulic head dataset. For this method we categorised a two week portion of the survey period into two groups: Groundwater pumping occurring, and groundwater pumping not occurring. The ANN would attempt to learn how the input surface SP dataset behaved during or in response to these altering pumping states, and therefore attempt to predict likelihood of their occurrences.

Input and labeled datasets are split into two groups: training data, and validation data. As their names suggest, training data is used in training an ANN to understand how inputs (the surface SP dataset) can or are affect by a labeled training dataset (in this case, groundwater pumping), and validation data sets are held out of any training techniques, as to genuinely identify if the ANN can make accurate predictions for unseen data points.

Results of the supervised ANN predicting periods of groundwater pumping can be viewed in Figure 6.6. Overall the ANN was slightly to moderately successful at predicting time periods of groundwater pumping occurring; in particular during the training period, where the relationship between surface SP data and periods of actual groundwater pumping is computed. Predicted versus actual results from the validation period were less correlated than in the training period, indicating there was potentially some ANN overfitting to the training data occuring.

Within both training and validation periods, there are several clear examples of the ANN predicting a very high likelihood of pumping, however no actual pumping events are occurring. Prolonged periods of no actual pumping occurring correlated with periods of high surface precipitation

at the site (refer to Figures 6.4 and 6.5). As these precipitation events were highly disruptive to electrical measurements of the SP surface array, and yet the ANN still predicted occurrences of groundwater pumping with high confidence during these times, it was therefore unlikely the ANN was predicting groundwater pumping schedules utilising small electrokinetic anomalies.

Further analysis of the prediction results, and continual tweaking of various ANN network structures made evident some additional relationship features which the ANN used to predict periods of groundwater pumping occurrence. Firstly, groundwater pumping occurred almost always during early morning or evening periods, as to minimise surface evaporation effects when watering the grounds. During these times solar, temperature and anthropogenic environmental noise effects were minimal, and therefore SP data signals are very stable. Additionally, due to automated scheduling pumping would often commence at approximately 03:30AM - 04:00AM. These two factors combined were too obvious and repetitive for determining groundwater flow, therefore distorting the ANNs ability to effectively detect groundwater pumping utilising only miunute SP data fluctuations.

Various ANN designs where trialed to overcome these effects, however all results were of a similar outcome. It was also likely that irrespective of the sites groundwater pumping pattern, the presence and amplitudes of SP anomalies caused by the groundwater pumping were not of an adequate and recognisable strength.

6.5.2 Calculation and filtering of environmental noise

The second of the two proposed ANN techniques utilised a total of 12 inputs, represented in Figure 6.4 and Figure 6.5. It aimed to predict the signal fluctuations that a surface SP array would experience when these input undesired external effects combined. The surface SP array dataset was used as the labelled training dataset. If the effects of undesired noise signals could be effectively predicted, this could be taken into consideration and subtracted from the unknown signal, theoretically leaving only the targeted and desired electrical effects contributing to signal change.

Ideally in future work when environmental filtering techniques are more developed, if a user was conducting a groundwater pumping investigation

then pumping data would not be provided to the ANN. Therefore, with all other sources of environmental noise accounted for and decoupled, the remaining signal would be of only electrokinetic groundwater effects.

Several modifications of recurrent ANN architectures and optimization features where trialed and tested before selection of a most optimal solution. Results presented in 6.7 utilised the following model architecture and features: a Sequential model of a 12 neuron input layer; two Gated Recurrent Unit (GRU) (Cho et al., 2014) hidden layers with variations of 12,18,24 or 30 neurons models (variations specified in 6.7), with a Rectified Linear Unit (ReLU) (Nair and Hinton, 2010) activation, a recurrent dropout value of 0.3 (Gal and Ghahramani, 2016), and an l1 and l2 regularization value of 0.1; and finally, a Dense output layer of six neurons with a sigmoid activation.

Training (labelled SP data) and validation (predicting of unlabelled SP data) phases are generally split as 70% and 30% of total data respectively, however for this research data was split in 50% halves. The reasoning for this was our research aim is more concerned in the resulting SP data predictions overall resemblance to the real SP data, versus the perfectness of the trained functions fit between SP data and our given input parameters.

Generally with use of ANNs, several statistical measures including accuracy, loss, R^2, or mean square error (MSE) values are used to determine the effectiveness of an ANN models fit to an ideal prediction or outcome. These values are instrumental for guiding a user during customisation and tweaking of an ANN model (eg. addition or subtraction of neurons and layers, use of dropout or regularization, various optimizers, learning rate), and generally indicate a more successful final prediction. Additionally, visualisation of each result can be overly time consuming. When relying alone on these values to analyse a final prediction, it can greatly oversimplify a models failure or success. Due to factors such as static shift which can negatively effect an ANNs statistical measurement values, several undisplayed ANN final prediction models had far superior MSE measures, however upon visual inspection of results these predictions were in fact less fitting with the overall aim of the investigation. As these quantitative measurements cannot take into account the key aims of an ANN's task,

epoch	mean squared error	val mean squared error
1	0.2427	0.2401
5	0.2338	0.2312
10	0.2221	0.2194
15	0.2093	0.2063
20	0.1949	0.1916
25	0.1786	0.1748
30	0.16	0.1559
35	0.1395	0.1351
40	0.1175	0.1131
45	0.0954	0.0912
50	0.0744	0.0708

Table 6.1: An output table of ANN training results per fifth epoch for the 2*30 neuron hidden layer model which summarises accuracy, loss, and mean square error for both training and validation datasets. 50 epochs per various tested ANN structure was the maximum epoch number given to reach the point of convergence (the estimated full learning potential of the model). Additional epochs, or a slower learning rate, would often result in overfitting of the training data and therefore lower quality results. Mean square error is the estimate of variance of residuals (or non-fit) in the population, and reached a considerable low 0.0744 and 0.0708 for training and validation data respectively.

it is important to visualise results in 6.7 in conjunction with statistical measures in Table 6.1.

Figure 6.7 presents results of four hidden layer neuron variations for the most overall successful Gated Recurrent Unit (GRU) architecture ANNs. Overall success was determined by combined factors of low mean square error value, and visual agreement of prediction data vs real SP data. Real SP data (top Figure 6.7) was filtered with a 60 second median filter, filtered for long term drifting trends, and whitened (static corrected) to zero. Both the presented real SP data and predicted SP data results (bottom Figure 6.7) were originally input and output from the ANN as six spatially individual SP array datasets. Six datasets were used to determine if any variances (predominately due to geospatial reasons) could be determined by the ANN. All real SP input data initially presented very little variance along array points, which all remained generally within a < 5 mV envelope of one another. With particular emphasis on assessing periods of pumping, no obvious geospatial differences or trends were evident among the six

individual SP prediction outputs. All six real and predicted SP data sets were therefore averaged and combined for ease of viewing results.

The results presented in Figure 6.7, in particularly the 24 and 30 neuron architecture predictions, show some encouraging correlation with the real SP dataset. Signal amplitudes are comparable and reasonable. Some prediction periods present a visible slight lag, or in some cases a lead, when compared to the real data. Some regions of predicted and real data do experience a break in, or lack of overall continuity.

The largest real SP signal increase on January 20th 2017 (top Figure 6.7, approximately central) was induced by a 12 mm rainfall event. Throughout the 42 day survey period, in excess of 80 mm of precipitation fell across just four significant rainfall events - an unusually high rainfall for a South Australian summer. These precipitation events had drastic effects on the real SP signal dataset, and due to their infrequency was the most difficult input for the ANN to accurately predict.

As hypothesised, subtraction of the real signal from the predicted signal does not result in a smooth, baseline zero SP signal. Amplitudes could not be appropriately matched, and lag and lead features caused displacement of the noise as opposed to reduction of the noise.

These various neuron results also emphasise the difference only small architectural changes can make to a final prediction result. Increasing the number of neurons to an architecture generally increases the number of overall decision paths. Too few neurons, and an architectures predictions can be too simplistic and therefore underdetermined - too many neurons and a prediction can be overdetermined.

6.6 Future work and improvements

Overall, several elements of the Morphetville field work and data collection program could be improved upon to ensure a future higher quality ANN prediction result.

Firstly and most importantly - as many as possible input variables should be recorded on site. Compact, low cost and high accuracy weather stations could be stationed on site as to not rely on nearby Bureau of Meterology weather station data. A magnetic station can also be used on site, rather

than from the nearest magnetic observatory in Alice Springs. Additional data collection to increase the number of ANN inputs should also be considered, including: measurement of redox potential and its fluctuations using platnium electrode techniques (Fiedler et al., 2007); measurement of moisture soil content fluctuations; and continual measurement of fluctuating contact resistance at each electrode along the array. Any additional environmental measurements that can provide an insight into any fluctuating soil chemistry properties would be greatly value adding.

A long term (approximately 3 to 6 month) research investigation would provide a great deal of data to train an ANN, and then determine with some confidence if the electrical fluctuations of a field site can be successfully predicted, and eventually effectively deconvolute the electrical signal

For groundwater investigations, or for other geophysical investigations regarding the isolation of a singular unknown electrical stimulus - further consideration must be given to the merging or subtraction of a predicted electrical signal from a real signal profile. A prediction will never be perfect, and it is harmful to introduce this additional bias into a result particularly in when signal to noise ratio is low. An additional output vector of an ANN's prediction confidence over time would be ideal for automating elements of this task.

6.7 Conclusions

In regards to the first trialed ANN for detection of pumping and non-pumping time periods, it was originally hypothesised that correlating a large dataset of SP fluctuations to causative factors would be challenging. As ANNs are an effective pattern recognition tool, this process was to explore the possibility that during groundwater pumping, at any singular or amongst multiple electrodes within the surface SP array, a potentially unique signature electrokinetic electrical response was formed. The ANN successfully recognised a pattern in time, but not in the arrays electrical responses for effective predictive capabilities in determining the status of a pumping event.

The second ANN trialed to calculate and filter environmental noise from SP data was a natural progression towards deciphering and differentiation of a causal factors potentially resulting electrical variation. This process was

investigated to challenge thinking regarding current filtering, processing, and information extraction techniques for SP surveys. There is seemingly a lacking scope of environment specific filtering methodologies available for SP surveys, and low-frequency electrical methods in general. Several papers do discuss to some depth the affect which various environmental conditions can have on an electrical monitoring program - in particularly, several studies do incorporate on site temperature monitoring to offset known linear thermoelectric effects on electrodes (Rizzo et al., 2004). However, no current studies could be found which aimed to incorporate any magnetic or advanced meteorological datasets using ANN techniques with long term electrical potential datasets.

The nature of manual, user defined analysis and filtering of electrical data can bear some unavoidable difficulties including: requiring an individual possessing the required domain knowledge to utilise appropriate toolsets; the potential for the introduction of user bias; and particularly, consumption of time to complete the task. Automating this process either nullifies or reduces the effects of these difficulties.

The use of ANNs and additional external datasets for noise filtering is proposed not as only relevant in the field of groundwater SP studies, which in fact are more often only short-term monitoring programs, but for all geophysical subdisciplines which utilise long-term electrical monitoring (eg. dam or volcanic zone monitoring, magnetotelluric investigations).

As of yet, it is premature to conclude if this form of filtering was successful as a further research is required, taking into account some of the previously discussed potential technique improvements. Exploration of ideas, such as these presented ANN techniques, that aim to more autonomously and effectively utilise rapidly improving low-cost computing capabilities, will sit at the forefront of this coming generation of geophysical research.

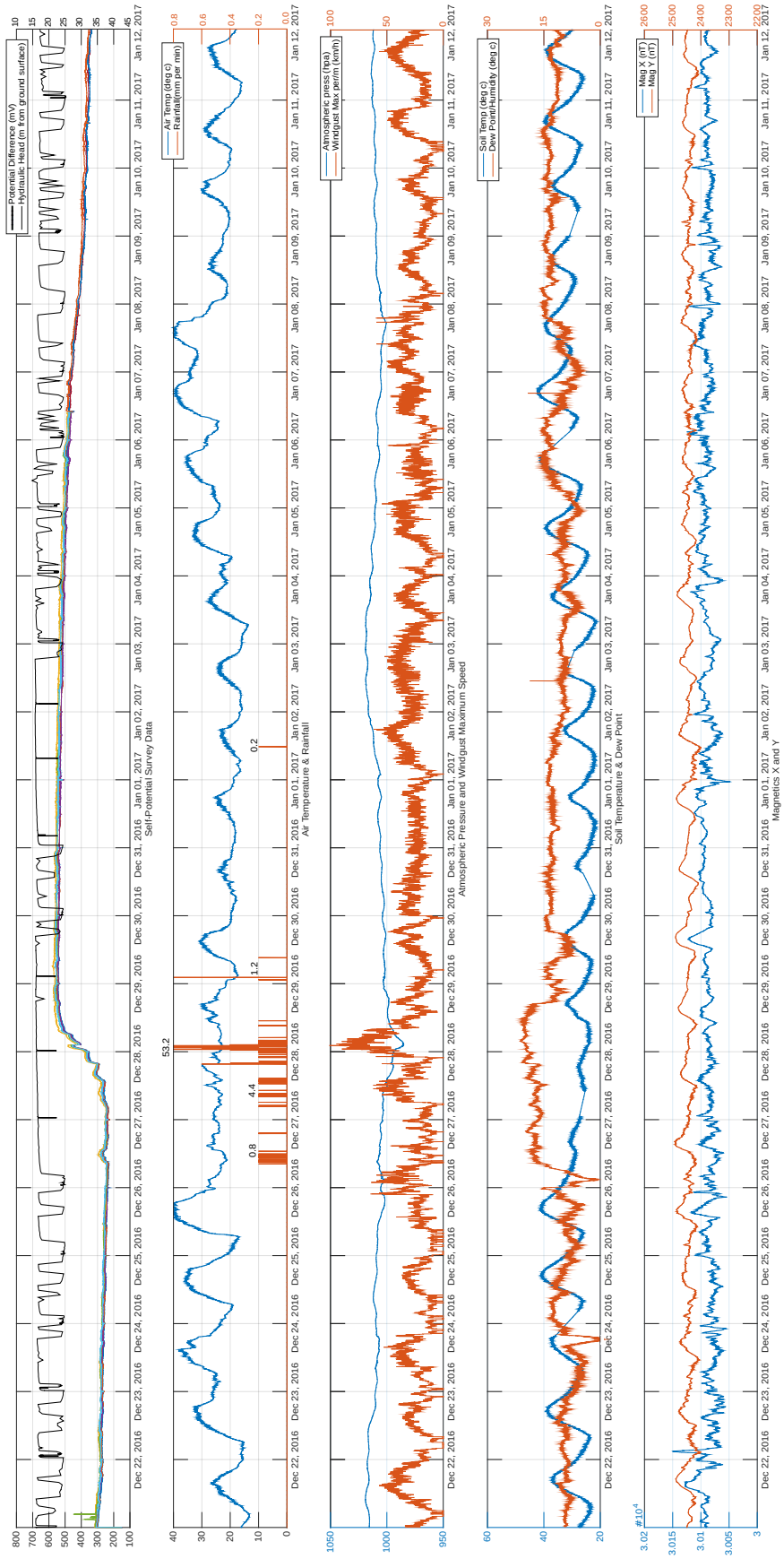

Figure 6.4: First of two: At the Morphettville Site, surface SP, hydraulic head level, environmental and magnetic datasets used in the noise filtering ANN. Datasets collected on ground by a SP surface array of 48 electrodes, autonomous well logging systems, the Bureau of Meteorology Adelaide Airport station 3 km north of site, and the Geoscience Australia magnetic observatory in Alice Springs respectively.

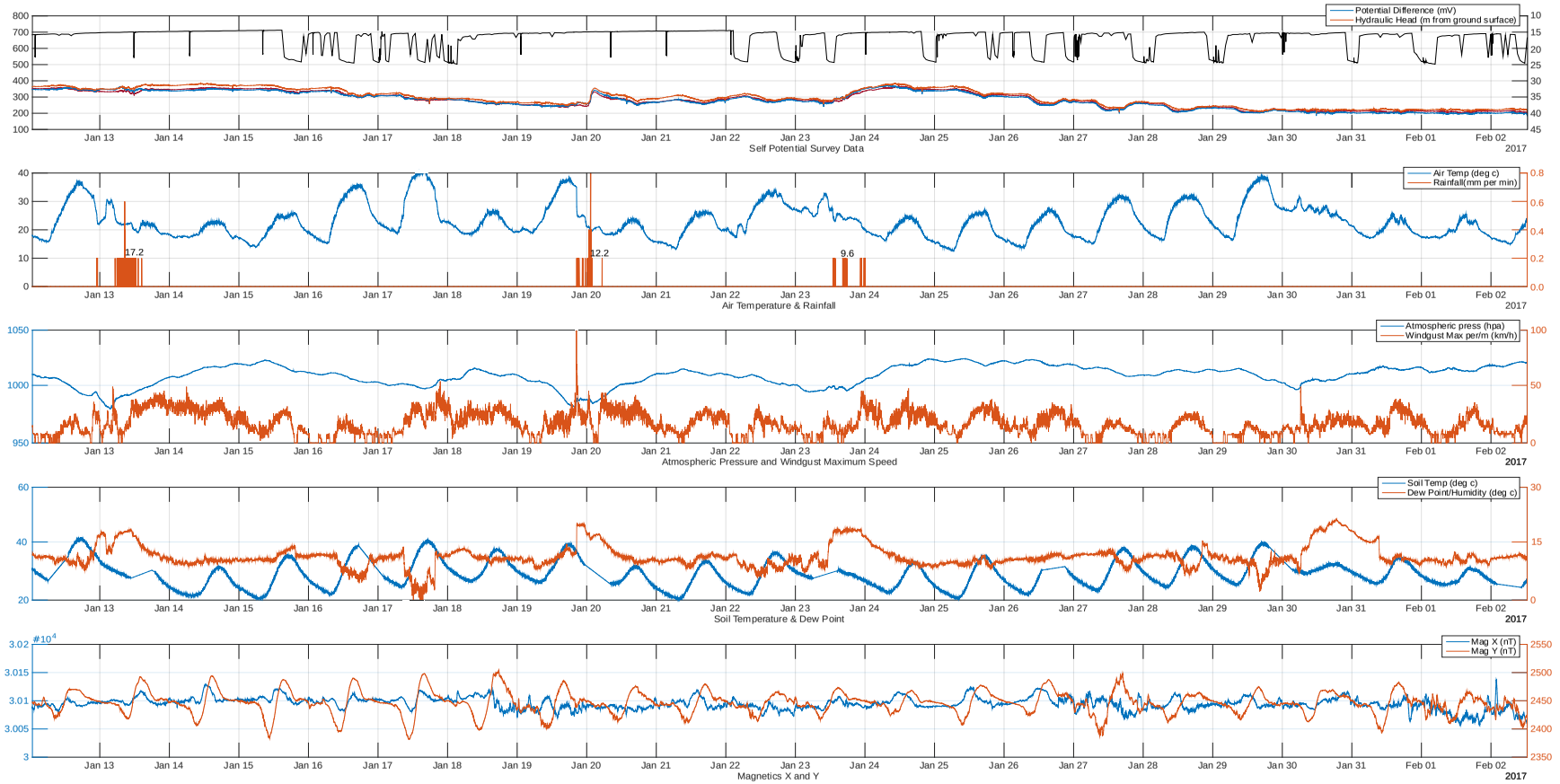

Figure 6.5: Second of two: At the Morphettville Site, surface SP, hydraulic head level, environmental and magnetic datasets used in the noise filtering ANN. Datasets collected on ground by a SP surface array of 48 electrodes, autonomous well logging systems, the Bureau of Meteorology Adelaide Airport station (3 km north of site), and the Geoscience Australia magnetic observatory in Alice Springs respectively.

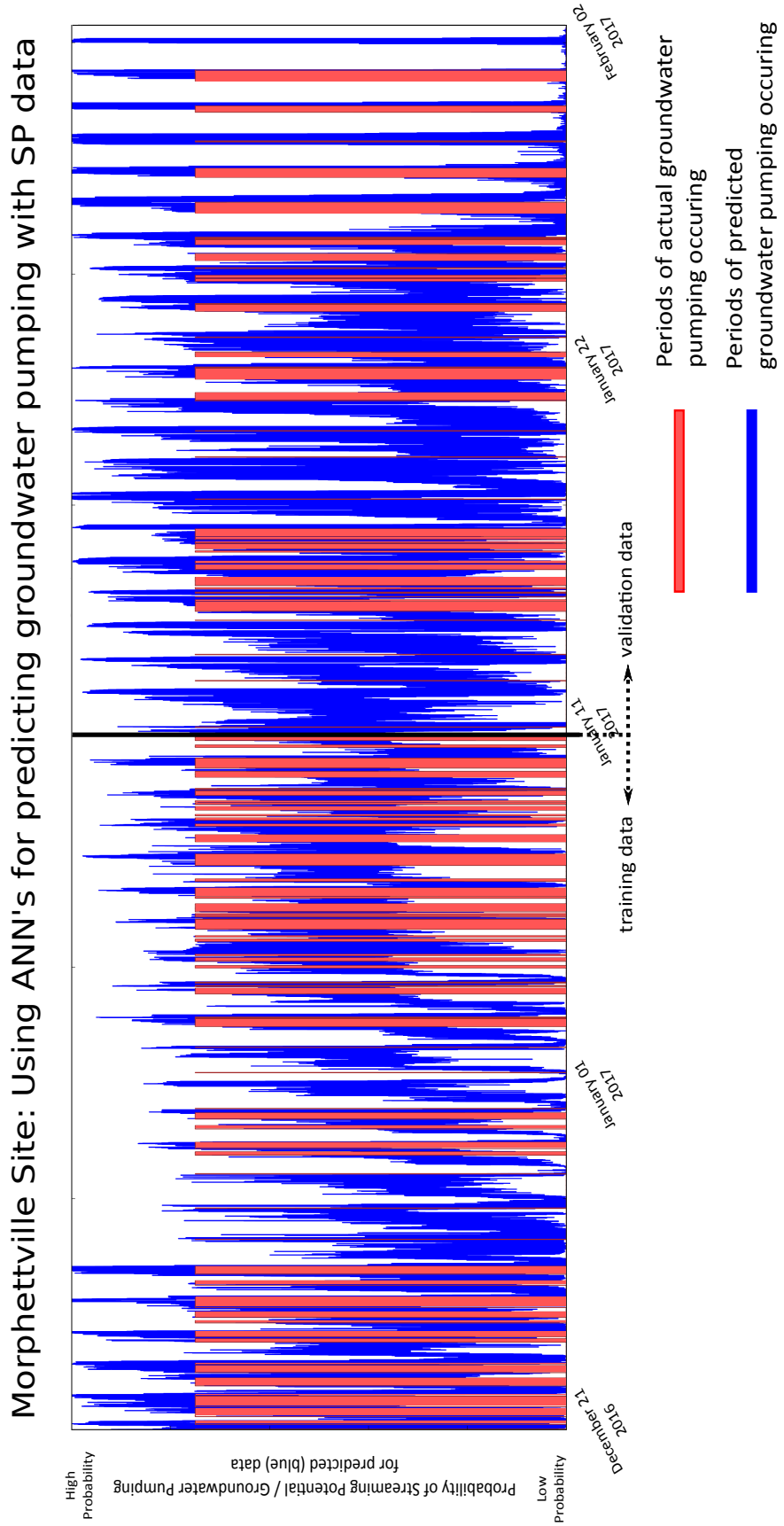

Figure 6.6: Results of supervised ANN for predicting periods of groundwater pumping occurrence at the Morphettville site. With pumping well data logs used for labeling of the training set, the ANN utilities fluctuations of real surface SP data to then predict likelihood of groundwater pumping occurring at a given point in time. With the y-axis representing the probability of groundwater pumping occurring, resulting predictions (blue) attempt to align with periods of actual pumping occurring (red) for an ideal fit of prediction.

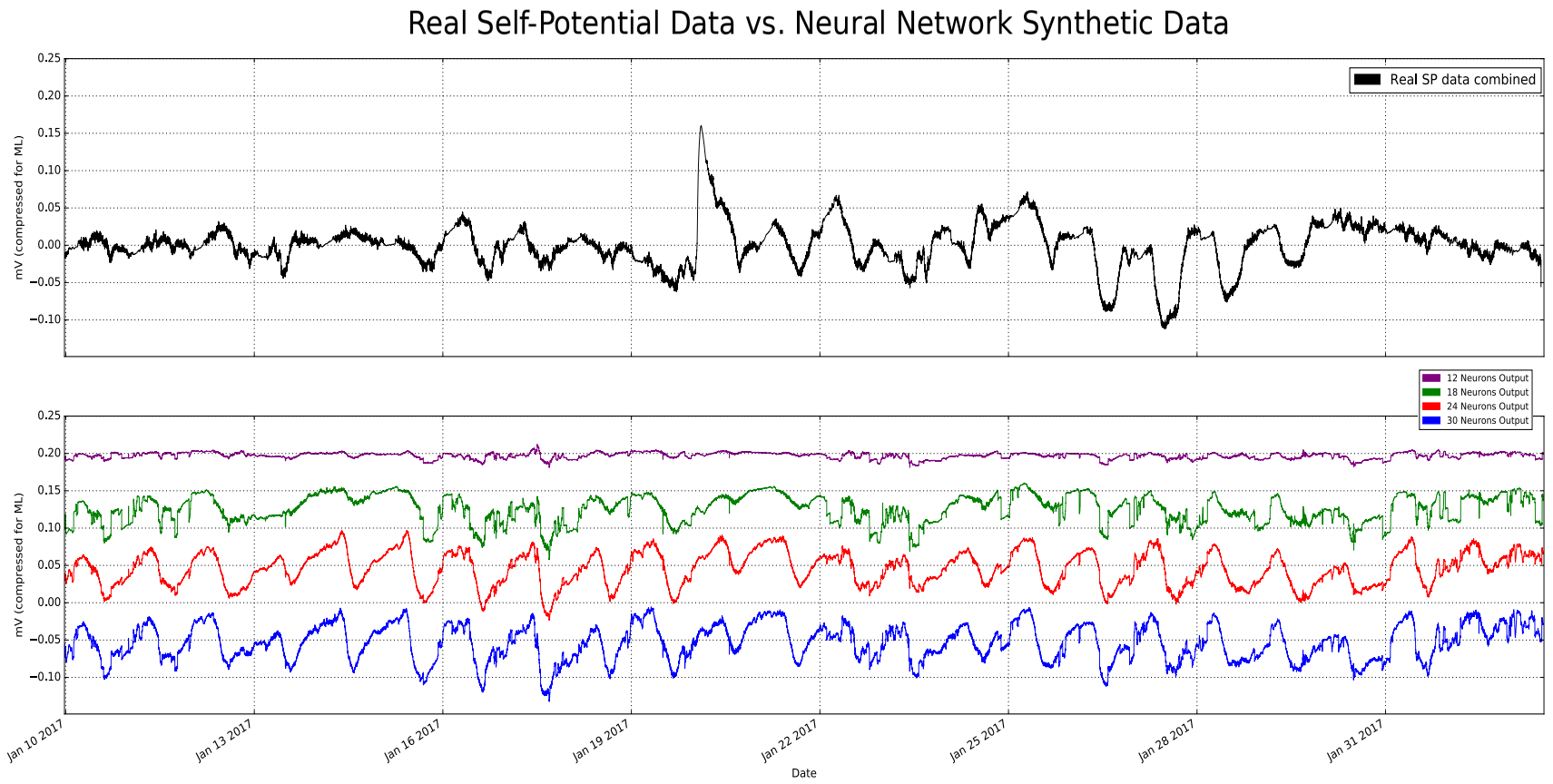

Figure 6.7: Results for the Morphettville SP ANN environmental noise filtering technique investigation. Above: A real Morphettville SP data profile averaged from six stable electrodes of the surface array, with a 60 second median filter applied, and long term static drift effects removed. Below: Output of four various ANN architecture (12, 18, 24 and 30 neuron) validation (results) datasets of the predicted surface SP data at Morphettville. The presented validation dataset utilises only 12 various environmental, magnetic, and groundwater inputs for prediction of a synthetic SP signal. The synthetic signal can be regarded as an attempted replication of the real SP signal. The supervised recurrent neural network was trained using the initial 50% of the total 43 day Morphetville real surface SP dataset as labelled data.

CHAPTER

SEVEN

CONCLUDING REMARKS

As one of the oldest standing methods in geophysics, self-potential techniques have been applied to a broad range of uses over time.

Its application and role in groundwater research as a qualitative, or more recently quantitative tool, is emerging rapidly. Due partially to advancements in instrumentation and processing capabilities, it is likely this trend will continue. Future research will further improve the resolution of the methodology, creating greater value to groundwater investigations.

Currently, there are still several challenges the technique faces, and results presented in this thesis have touched on a number of these challenging aspects.

Problematic since its conception, deciphering of actual electrokinetic signal from background electrical noise continues to be a significant issue. In this program, we observed numerous ambiguous electrical potential sources within all datasets acquired.

With electrical hardware instrumentation capabilities now relatively plateaued, increasing the utilisation of rapidly advancing computational and processing capabilities could be of assistance to the technique. Works at Morphettville utilising artificial neural networks for noise filtering were a first

of its kind. Visual inspection of real versus predicted self-potential signal results were encouraging, however further research is required.

Correct use of instrumentation, set-up methodologies, and understanding the limitations of the technique in regards to applicable settings are also of critical importance. Although advancements to instrumentation have increased signal accuracy and precision, there is still significant difficulties regarding the practical, real world application of self-potential techniques. These real world difficulties will need to be overcome before the self-potential method can become sufficiently commonplace in groundwater investigations

Irrespective of its problematic elements, for good reason the self-potential method is one of the oldest yet still broadly practiced geophysical techniques. Regarded as the only geophysical technique sensitive to the actual flow of groundwater, low in cost, and a non-invasive alternative to drilling investigations, researchers will continue to remove ambiguities from the timeless technique.

BIBLIOGRAPHY

Adler, P. M., Thovert, J.-F., Jacquin, C., Morat, P., and Le Mouel, J.-L. (1997). Electrical signals induced by the atmospheric pressure variations in unsaturated media. *Comptes rendus de l'Académie des sciences. Série 2. Sciences de la terre et des planètes*, 324(9):711–718.

Ahmed, A. S., Jardani, A., Revil, A., and Dupont, J. P. (2016). Specific storage and hydraulic conductivity tomography through the joint inversion of hydraulic heads and self-potential data. *Advances in Water Resources*, 89:80–90.

Al-Garni, M. A. (2010). Interpretation of spontaneous potential anomalies from some simple geometrically shaped bodies using neural network inversion. *Acta Geophysica*, 58(1):143.

Allègre, V., Jouniaux, L., Lehmann, F., and Sailhac, P. (2010). Streaming potential dependence on water-content in Fontainebleau sand. *Geophysical Journal International*, 182(3):1248–1266.

Allègre, V., Jouniaux, L., Lehmann, F., Sailhac, P., and Toussaint, R. (2015). Influence of water pressure dynamics and fluid flow on the streaming-potential response for unsaturated conditions. *Geophysical Prospecting*, 63(3):694–712.

Aubert, M. and Atangana, Q. Y. (1996). Self-potential method in hydrogeological exploration of volcanic areas. *Groundwater*, 34(6):1010–1016.

Baan, M. and Jutten, C. (2000). Neural networks in geophysical applications. *Geophysics*, 65(4):1032–1047.

Baddari, K., Aïfa, T., Djarfour, N., and Ferahtia, J. (2009). Application of a radial basis function artificial neural network to seismic data inversion. *Computers & Geosciences*, 35(12):2338–2344.

Bader, S. (2005). *Osmosis in groundwater: chemical and electrical extensions to Darcy's Law*. Ponsen and Looijen.

Bigalke, J. and Grabner, E. W. (1997). The geobattery model: a contribution to large scale electrochemistry. *Electrochimica Acta*, 42(23):3443–3452.

Birch, F. (1993). Testing Fournier's method for finding water table from self-potential. *Groundwater*, 31(1):50–56.

Birch, F. (1998). Imaging the water table by filtering self-potential profiles. *Groundwater*, 36(5):779–782.

Bockris, J. O. and Khan, S. U. (2013). *Surface electrochemistry: a molecular level approach*. Springer Science & Business Media.

Bogoslovsky, V. V. and Ogilvy, A. A. (1973). Deformations of natural electric fields near drainage structures *. *Geophysical Prospecting*, 21(4):716–723.

Boné, R. and Cardot, H. (2011). Advanced methods for time series prediction using recurrent neural networks. In *Recurrent Neural Networks for Temporal Data Processing*. InTech.

Brauchler, R., Hu, R., Hu, L., Jiménez, S., Bayer, P., Dietrich, P., and Ptak, T. (2013). Rapid field application of hydraulic tomography for resolving aquifer heterogeneity in unconsolidated sediments. *Water Resources Research*, 49(4).

Bultreys, T., Boone, M. A., Boone, M. N., De Schryver, T., Masschaele, B., Van Loo, D., Van Hoorebeke, L., and Cnudde, V. (2015). Real-time visualization of Haines jumps in sandstone with laboratory-based microcomputed tomography. *Water Resources Research*, 51(10):8668–8676.

Butler, J. J. and Zhan, X. (2004). Hydraulic tests in highly permeable aquifers. *Water Resources Research*, 40(12):1–12.

Cho, K., Van Merriënboer, B., Gulcehre, C., Bahdanau, D., Bougares, F., Schwenk, H., and Bengio, Y. (2014). Learning phrase representations using RNN encoder-decoder for statistical machine translation. *arXiv preprint arXiv:1406.1078*.

Cooley, R. L. (1977). A method of estimating parameters and assessing reliability for models of steady state groundwater flow: 1. theory and numerical properties. *Water Resources Research*, 13(2):318–324.

Corry, C. E. (1985). Spontaneous polarization associated with porphyry sulfide mineralization. *Geophysics*, 50(6):1020–1034.

Corwin, R. (1990). The self-potential method for environmental and engineering applications. In *Geotechnical and Environmental Geophysics*, Investigations in Geophysics, pages 127–146. Society of Exploration Geophysicists.

Corwin, R. and Hoover, D. (1979). The self-potential method in geothermal exploration. *Geophysics*, 44(2):226–245.

Corwin, R. F. (1989). Data quality for engineering self-potential surveys. In *Detection of Subsurface Flow Phenomena*, pages 49–72. Springer.

CSIRO: Managed aquifer recharge scheme (2017). MAR information website. `https://research.csiro.au/mar/using-managed-aquifer-recharge/#map`.

Darnet, M. and Marquis, G. (2004). Modelling streaming potential (SP) signals induced by water movement in the vadose zone. *Journal of Hydrology*, 285(1-4):114–124.

DataTaker Intelligent data loggers website (2018). Datataker DT85 instrument specifications. `http://www.datataker.com/DT85.php`.

Demuth, H. B., Beale, M. H., De Jess, O., and Hagan, M. T. (2014). *Neural network design*. Martin Hagan.

DesRoches, A. J., Butler, K. E., and MacQuarrie, K. T. (2017). Surface self-potential patterns related to transmissive fracture trends during a water injection test. *Geophysical Journal International*, 212(3):2047–2060.

DEWNR (2009). Clare Valley PWRA fractured rock aquifer 2009-2014 groundwater level and salinity status report: Government of South Australia: Department of Environment, Water and Natural Resources.

DEWNR (2016). Central Adelaide PWA T1 aquifer groundwater level and salinity status report: Government of South Australia: Department of Environment, Water and Natural Resources.

Dong, C.-Y., Shin, D., Joo, S., Nam, Y., and Cho, K.-H. (2012). Identification of feedback loops in neural networks based on multi-step Granger causality. *Bioinformatics*, 28(16):2146–2153.

Ernstson, K. and Scherer, H. U. (1986). Self-potential variations with time and their relation to hydrogeologic and meteorological parameters. *Geophysics*, 51(10):1967–1977.

Esmaeili, S., Rahbar, M., Pahlavanzadeh, H., and Ayatollahi, S. (2016). Investigation of streaming potential coupling coefficients and zeta potential at low and high salinity conditions: Experimental and modeling approaches. *Journal of Petroleum Science and Engineering*, 145:137–147.

Fagerlund, F. and Heinson, G. (2003). Detecting subsurface groundwater flow in fractured rock using self-potential (SP) methods. *Environmental Geology*, 43(7):782–794.

Fiedler, S., Vepraskas, M. J., and Richardson, J. (2007). Soil redox potential: importance, field measurements, and observations. *Advances in Agronomy*, 94:1–54.

Fitterman, D. V. (1978). Electrokinetic and magnetic anomalies associated with dilatant regions in a layered earth. *Journal of Geophysical Research: Solid Earth*, 83(B12):5923–5928.

Fitterman, D. V. (1979). Calculations of self-potential anomalies near vertical contacts. *Geophysics*, 44(2):195–205.

Fitterman, D. V. and Corwin, R. F. (1982). Inversion of self-potential data from the Cerro Prieto geothermal field, Mexico. *Geophysics*, 47(6):938–945.

Foden, J., Elburg, M. A., Dougherty-Page, J., and Burtt, A. (2006). The timing and duration of the Delamerian Orogeny: correlation with the Ross Orogen and implications for Gondwana assembly. *The Journal of Geology*, 114(2):189–210.

Fournier, C. (1989). Spontaneous potentials and resistivity surveys applied to hydrogeology in a volcanic area: Case history of the Chaîne des Puys (Puy-de-Dôme, France). *Geophysical Prospecting*, 37(6):647–668.

Fox, R. W. (1830). On the electro-magnetic properties of metalliferous veins in the mines of Cornwall. *Philosophical Transactions of the Royal Society of London*, 120:399–414.

Furness, P. (1992). Modelling spontaneous mineralization potentials with a new integral equation. *Journal of Applied Geophysics*, 29(2):143–155.

Gal, Y. and Ghahramani, Z. (2016). A theoretically grounded application of dropout in recurrent neural networks. In *Advances in neural information processing systems*, pages 1019–1027.

Gard, M. (2015). Monitoring groundwater flow in fractured rock environments using self-potential methods. University of Adelaide: Thesis submission for BSc (Honours) in Geophysics.

Gers, F. A. and Schmidhuber, J. (2000). Recurrent nets that time and count. In *Neural Networks, 2000. IJCNN 2000, Proceedings of the IEEE-INNS-ENNS International Joint Conference on*, volume 3, pages 189–194. IEEE.

Gers, F. A., Schmidhuber, J., and Cummins, F. (2000). Learning to forget: Continual prediction with LSTM. *Neural Computation*, 12(10):2451–2471.

Gibert, D. and Pessel, M. (2001). Identification of sources of potential fields with the continuous wavelet transform: Application to self-potential profiles. *Geophysical Research Letters*, 28(9):1863–1866.

Glover, P. (2015). Treatise on geophysics. In *Geophysical properties of the near surface Earth: Electrical properties*. Elsevier.

Glover, P. and Déry, N. (2010). Streaming potential coupling coefficient of quartz glass bead packs: Dependence on grain diameter, pore size, and pore throat radius. *Geophysics*, 75(6):F225–F241.

Glover, P. W., Walker, E., and Jackson, M. D. (2012). Streaming-potential coefficient of reservoir rock: A theoretical model. *Geophysics*, 77(2):D17–D43.

Gorelik, A. and Nesterenko, I. (1956). Metod potentsialov elektrofil'-tratsii pri opredelenii radiusa depressionnoi voronki v khode otkachki iz skvazhini (method of electro-filtration potential in the determination of radius of the depression cone during a pumping test from borehole). *Izvestia Akad. Nauk SSSR, Ser. Geofiz.(Solid Earth Phys.)*, 11:1361–1363.

Haas, A. and Revil, A. (2009). Electrical burst signature of pore-scale displacements. *Water Resources Research*, 45(10).

Hämmann, M., Maurer, H., Green, A., and Horstmeyer, H. (1997). Self-potential image reconstruction: capabilities and limitations. *Journal of environmental and engineering geophysics*, 2(1):21–35.

He, Q. and Zhou, H. (2003). Application of artificial neural networks to seismic waveform inversion. In *Geophysical Applications of Artificial Neural Networks and Fuzzy Logic*, Modern Approaches in Geophysics, pages 89–101. Springer, Dordrecht. DOI: 10.1007/978-94-017-0271-3_7.

Hinton, G. E. and Sejnowski, T. J. (1999). *Unsupervised learning: foundations of neural computation*. MIT press.

Hornby, P., Boschetti, F., and Horowitz, F. (1999). Analysis of potential field data in the wavelet domain. *Geophysical Journal International*, 137(1):175–196.

Huo, D. and Benson, S. M. (2015). An experimental investigation of stress-dependent permeability and permeability hysteresis behavior in rock fractures. *Fluid dynamics in complex fractured-porous systems*, pages 99–114.

Inverarity, K. (2014). *Electrical geophysics of carbonate mound spring complexes of the South-Western Great Artesian Basin*. phdthesis, The University of Adelaide. http://hdl.handle.net/2440/92549.

Ishido, T. and Mizutani, H. (1981). Experimental and theoretical basis of electrokinetic phenomena in rock-water systems and its applications to geophysics. *Journal of Geophysical Research: Solid Earth*, 86:1763–1775.

Iuliano, T., Mauriello, P., and Patella, D. (2002). Looking inside Mount Vesuvius by potential fields integrated probability tomographies. *Journal of Volcanology and Geothermal Research*, 113(3):363–378.

Jaafar, M., Vinogradov, J., and Jackson, M. (2009). Measurement of streaming potential coupling coefficient in sandstones saturated with high salinity NaCl brine. *Geophysical Research Letters*, 36(21).

Jackson, D. B. and Kauahikaua, J. (1987). Regional self-potential anomalies at Kilauea volcano. *US Geol. Surv. Prof. Pap*, 1350(40):947–959.

Jacobson, G. and Lau, J. (2017). Hydrogeology map of Australia (G.Jacobson and JE.Lau hydrogeology map). `https://data.gov.au/dataset/hydrogeology-map-of-australia-g-jacobson-and-je-lau-hydrogeology-map`

Jardani, A., Revil, A., Barrash, W., Crespy, A., Rizzo, E., Straface, S., Cardiff, M., Malama, B., Miller, C., and Johnson, T. (2009). Reconstruction of the water table from self-potential data: A bayesian approach. *Groundwater*, 47(2):213–227.

Jardani, A., Revil, A., Bolève, A., Crespy, A., Dupont, J.-P., Barrash, W., and Malama, B. (2007). Tomography of the darcy velocity from self-potential measurements. *Geophysical Research Letters*, 34(24).

Jardani, A., Revil, A., Bolève, A., and Dupont, J. P. (2008). Three-dimensional inversion of self-potential data used to constrain the pattern of groundwater flow in geothermal fields. *Journal of Geophysical Research: Solid Earth*, 113:B09204.

Jiang, Y., Shan, F., Jin, H., Zhou, L., and Sheng, P. (1998). A method for measuring electrokinetic coefficients of porous media and its potential

application in hydrocarbon exploration. *Geophysical Research Letters*, 25(10):1581–1584.

Jougnot, D. and Linde, N. (2013). Self-potentials in partially saturated media: the importance of explicit modeling of electrode effects. *Vadose Zone Journal*, 12(2).

Jouniaux, L. and Bordes, C. (2012). Frequency-dependent streaming-potentials: a review. *International Journal of Geophysics*, 2012.

Jouniaux, L. and Ishido, T. (2012). Electrokinetics in earth sciences: A tutorial. *International Journal of Geophysics*, 2012:e286107.

Jouniaux, L., Maineult, A., Naudet, V., Pessel, M., and Sailhac, P. (2009). Review of self-potential methods in hydrogeophysics. *Comptes Rendus Geoscience*, 341(10-11):928–936.

Jouniaux, L. and Pozzi, J.-P. (1995). Streaming potential and permeability of saturated sandstones under triaxial stress: Consequences for electrotelluric anomalies prior to earthquakes. *Journal of Geophysical Research: Solid Earth*, 100(B6):10197–10209.

Kaftan, Ilknur, S. P. and Akdemir, Ö. (2014). Inversion of self potential anomalies with Multilayer Perceptron neural networks. *Pure and Applied Geophysics*, 171(8):1939–1949.

Khesin, B. E., Alexeyev, V., and Eppelbaum, L. (2013). *Interpretation of geophysical fields in complicated environments*, volume 14. Springer Science & Business Media.

Kilty, K. T. (1984). On the origin and interpretation of self-potential anomalies. *Geophysical Prospecting*, 32(1):51–62.

Kitanidis, P. K. (1986). Parameter uncertainty in estimation of spatial functions: Bayesian analysis. *Water Resources Research*, 22(4):499–507.

Krásnỳ, J. and Sharp, J. M. (2007). *Groundwater in fractured rocks: IAH selected paper series*, volume 9. CRC Press.

Lapenna, V., Patella, D., and Piscitelli, S. (2000). Tomographic analysis of self-potential data in a seismic area of southern italy. *Annals of Geophysics*, 43(2).

Levine, S., Marriott, J. R., Neale, G., and Epstein, N. (1975). Theory of electrokinetic flow in fine cylindrical capillaries at high zeta-potentials. *Journal of Colloid and Interface Science*, 52(1):136–149.

Linde, N., Jougnot, D., Revil, A., Matthäi, S., Arora, T., Renard, D., and Doussan, C. (2007). Streaming current generation in two-phase flow conditions. *Geophysical Research Letters*, 34(3).

Loaiciga, H. A. and Mariño, M. A. (1987). Parameter estimation in groundwater: classical, bayesian, and deterministic assumptions and their impact on management policies. *Water Resources Research*, 23(6):1027–1035.

Love, A., Cook, P., Harrington, G., and Simmons, C. (2001). Resource assessment division of the Department for Water Resources. `https://www.waterconnect.sa.gov.au/Content/Publications/DEW/Groundwater%20flow%20in%20the%20Clare%20Valley.pdf`.

Luong, D. and Sprik, R. (2013). Streaming potential and electroosmosis measurements to characterize porous materials. *IRSN Geophysics*, 2013.

MacAllister, D., Jackson, M., Butler, A., and Vinogradov, J. (2016). Tidal influence on self-potential measurements. *Journal of Geophysical Research: Solid Earth*, 121(12):8432–8452.

Mao, D., Yeh, T.-C. J., Wan, L., Wen, J.-C., Lu, W., Lee, C.-H., and Hsu, K.-C. (2013). Joint interpretation of sequential pumping tests in unconfined aquifers. *Water Resources Research*, 49(4):1782–1796.

Mauri, G., Williams-Jones, G., and Saracco, G. (2010). Depth determinations of shallow hydrothermal systems by self-potential and multi-scale wavelet tomography. *Journal of Volcanology and Geothermal Research*, 191(3-4):233–244.

Maxwell, J. C. (1865). VIII. A dynamical theory of the electromagnetic field. *Philosophical transactions of the Royal Society of London*, 155:459–512.

McCulloch, W. S. and Pitts, W. (1943). A logical calculus of the ideas immanent in nervous activity. *The bulletin of mathematical biophysics*, 5(4):115–133.

Mohri, M., Rostamizadeh, A., and Talwalkar, A. (2012a). *Foundations of machine learning*. Adaptive computation and machine learning series. MIT Press.

Mohri, M., Rostamizadeh, A., and Talwalkar, A. (2012b). *Foundations of machine learning*. MIT press.

Moore, J. R. and Glaser, S. D. (2007). Self-potential observations during hydraulic fracturing. *Journal of Geophysical Research: Solid Earth*, 112(B2).

Moreau, F., Gibert, D., Holschneider, M., and Saracco, G. (1999). Identification of sources of potential fields with the continuous wavelet transform: Basic theory. *Journal of Geophysical Research: Solid Earth*, 104:5003–5013.

Mortimer, L., Aydin, A., Simmons, C., and Love, A. (2011). Is in situ stress important to groundwater flow in shallow fractured rock aquifers? *Journal of hydrology*, 399(3-4):185–200.

Morton, D., Love, A., Clarke, D., Martin, R., Cook, P., and McEwan, K. (1998). Clare Valley groundwater resources. *Dept Primary Industries Resources South Australia Program Report*, 1.

Mozer, M. C. (1989). A focused backpropagation algorithm for temporal pattern recognition.

Murat, M. E. and Rudman, A. J. (1992). Automated first arrival picking: A neural network approach1. *Geophysical Prospecting*, 40(6):587–604.

Murty, B. S. and Haricharan, P. (1985). Nomogram for the complete interpretation of spontaneous potential profiles over sheet-like and cylindrical two-dimensional sources. *Geophysics*, 50(7):1127–1135.

Nair, V. and Hinton, G. E. (2010). Rectified linear units improve restricted Boltzmann machines. In *Proceedings of the 27th international conference on machine learning (ICML-10)*, pages 807–814.

Naudet, V., Revil, A., Bottero, J.-Y., and Bégassat, P. (2003). Relationship between self-potential (SP) signals and redox conditions in contaminated groundwater. *Geophysical Research Letters*, 30(21):2091.

Naudet, V., Revil, A., Rizzo, E., Bottero, J.-Y., and Bégassat, P. (2004). Groundwater redox conditions and conductivity in a contaminant plume from geoelectrical investigations. *Hydrology and Earth System Sciences Discussions*, 8(1):8–22.

Neuman, S. P., Fogg, G. E., and Jacobson, E. A. (1980). A statistical approach to the inverse problem of aquifer hydrology: 2. Case study. *Water Resources Research*, 16(1):33–58.

Overbeek, J. T. (1956). The Donnan equilibrium. *Prog. Biophys. Biophys. Chem*, 6(1):57–84.

Patella, D. (1997a). Introduction to ground surface self-potential tomography. *Geophysical Prospecting*, 45(4):653–681.

Patella, D. (1997b). Self-potential global tomography including topographic effects. *Geophysical Prospecting*, 45(5):843–863.

Pengra, D. B., Xi Li, S., and Wong, P. (1999). Determination of rock properties by low-frequency AC electrokinetics. *Journal of Geophysical Research: Solid Earth*, 104(B12):29485–29508.

Perrier, F. and Morat, P. (2000). Characterization of electrical daily variations induced by capillary flow in the non-saturated zone. *Pure and Applied Geophysics*, 157(5):785–810.

Perrier, F. and Pant, S. R. (2005). Noise reduction in long-term self-potential monitoring with travelling electrode referencing. *pure and applied geophysics*, 162(1):165–179.

Perrier, F., Trique, M., Lorne, B., Avouac, J.-P., Hautot, S., and Tarits, P. (1998). Electric potential variations associated with yearly lake level variations. *Geophysical Research Letters*, 25(11):1955–1958.

Petiau, G. (2000). Second generation of lead-lead chloride electrodes for geophysical applications. *Pure and Applied Geophysics*, 157(3):357–382.

Poldini, E. (1938). Geophysical exploration by spontaneous polarization methods. *Min. Mag., 59 (1938), pp. 278-282*, Min. Mag., 59 (1938), pp. 347-352.

Poulton, M., Sternberg, B., and Glass, C. (1992). Location of subsurface targets in geophysical data using neural networks. *Geophysics*, 57(12):1534–1544.

Preiss, W. (1987). Tectonics of the Adelaide Geosyncline. *The Adelaide Geosyncline–late Proterozoic stratigraphy, sedimentation, palaeontology and tectonics: Geological Survey of South Australia Bulletin*, 53:255–282.

Preiss, W. (2006). Geology of the Clare Valley, South Australia: Earth resources information sheet: Division of Minerals and Energy Resources, PIRSA. `https://www.waterconnect.sa.gov.au/Content/Publications/DEW/Groundwater%20flow%20in%20the%20Clare%20Valley.pdf`.

Pride, S. (1994). Governing equations for the coupled electromagnetics and acoustics of porous media. *Physical Review B*, 50(21):15678–15696.

Quincke, G. (1859). About a new kind of electric currents. *Annalen der Physik*, 183(5):1–47.

Reppert, P. M. and Morgan, F. D. (2003). Temperature-dependent streaming potentials: 1. theory. *Journal of Geophysical Research: Solid Earth*, 108(B11).

Revil, A. (2016). New developments in induced polarization: from petrophysics to new approaches of tomography. In *AGU Fall Meeting Abstracts*.

Revil, A., Gevaudan, C., Lu, N., and Maineult, A. (2008). Hysteresis of the self-potential response associated with harmonic pumping tests. *Geophysical Research Letters*, 35(16):L16402.

Revil, A. and Glover, P. W. J. (1998). Nature of surface electrical conductivity in natural sands, sandstones, and clays. *Geophysical Research Letters*, 25(5):691–694.

Revil, A. and Jardani, A. (2013). *The self-potential method: theory and applications in environmental geosciences*. Cambridge University Press.

Revil, A., Karaoulis, M., Johnson, T., and Kemna, A. (2012). Review: Some low-frequency electrical methods for subsurface characterization and monitoring in hydrogeology. *Hydrogeology Journal*, 20(4):617–658.

Revil, A. and Leroy, P. (2001). Hydroelectric coupling in a clayey material. *Geophysical Research Letters*, 28(8):1643–1646.

Revil, A., Leroy, P., and Titov, K. (2005). Characterization of transport properties of argillaceous sediments: Application to the Callovo-Oxfordian argillite. *Journal of Geophysical Research: Solid Earth*, 110(B6).

Revil, A., Naudet, V., Nouzaret, J., and Pessel, M. (2003). Principles of electrography applied to self-potential electrokinetic sources and hydrogeological applications. *Water Resources Research*, 39(5):1114.

Revil, A., Pezard, P., and Glover, P. (1999a). Streaming potential in porous media 1. Theory of the zeta potential. *Journal of Geophysical Research: Solid Earth*, 104:20021–20031.

Revil, A., Schwaeger, H., Cathles, L. M., and Manhardt, P. D. (1999b). Streaming potential in porous media: 2. theory and application to geothermal systems. *Journal of Geophysical Research: Solid Earth*, 104:20033–20048.

Revil, A., Titov, K., Doussan, C., and Lapenna, V. (2006). Application of the self-potential method to hydrological problems. In Vereecken, H., Binley, A., Cassiani, G., Revil, A., and Titov, K., editors, *Applied Hydrogeophysics*, number 71 in NATO Science Series, pages 255–292. Springer Netherlands.

Rice, C. and Whitehead, R. (1965). Electrokinetic flow in a narrow cylindrical capillary. *The Journal of Physical Chemistry*, 69(11):4017–4024.

Rizzo, E., Suski, B., Revil, A., Straface, S., and Troisi, S. (2004). Self-potential signals associated with pumping tests experiments. *Journal of Geophysical Research: Solid Earth*, 109:B10203.

Roubinet, D., Linde, N., Jougnot, D., and Irving, J. (2016a). Streaming potential modeling in fractured rock: Insights into the identification of hydraulically active fractures. *Geophysical Research Letters*, 43(10):4937–4944.

Roubinet, D., Linde, N., Jougnot, D., and Irving, J. (2016b). Streaming potential modeling in fractured rock: Insights into the identification of hydraulically active fractures. *Geophysical Research Letters*, 43(10):4937–4944.

Sailhac, P., Darnet, M., and Marquis, G. (2004). Electrical streaming potential measured at the ground surface. *Vadose Zone Journal*, 3(4):1200–1206.

Sandham, W. and Leggett, M. (2013). *Geophysical Applications of Artificial Neural Networks and Fuzzy Logic*. Springer Science & Business Media. Google-Books-ID: hbTyCAAAQBAJ.

Saracco, G., Labazuy, P., and Moreau, F. (2004). Localization of self-potential sources in volcano-electric effect with complex continuous wavelet transform and electrical tomography methods for an active volcano. *Geophysical Research Letters*, 31(12).

Sato, M. and Mooney, H. (1960). Theory of geobattery. *Geophys., 15 (1960), p. 226*.

Saunders, J., Jackson, M., Gulamali, M., Vinogradov, J., and Pain, C. (2012). Streaming potentials at hydrocarbon reservoir conditions. *Geophysics*, 77(1):E77–E90.

Sen, P. (1991). Correspondence between membrane potential and conductivity. *GEOPHYSICS*, 56(4):461–471.

Sill, W. R. (1983). Self-potential modeling from primary flows. *GEOPHYSICS*, 48(1):76–86.

Sivenas, P. and Beales, F. W. (1982). Natural geobatteries associated with sulphide ore deposits, i. theoretical studies. *Journal of Geochemical Exploration*, 17(2):123–143.

Skinner, D. and Heinson, G. (2004). A comparison of electrical and electromagnetic methods for the detection of hydraulic pathways in a fractured rock aquifer, clare valley, south australia. *Hydrogeology Journal*, 12(5):576–590.

Slater, L. and Atekwana, E. (2013). Geophysical signatures of subsurface microbial processes. *Eos, Transactions American Geophysical Union*, 94(8):77–78.

Snow, D. T. (1968). Rock fracture spacings, openings, and porosities. *Journal of Soil Mechanics & Foundations Div.*

Soueid Ahmed, A., Jardani, A., Revil, A., and Dupont, J. (2013). SP2dinv: A 2d forward and inverse code for streaming potential problems. *Computers & Geosciences*, 59:9–16.

Soueid Ahmed, A., Jardani, A., Revil, A., and Dupont, J. P. (2014). Hydraulic conductivity field characterization from the joint inversion of hydraulic heads and self-potential data. *Water Resources Research*, 50(4):3502–3522.

Stoll, J., Bigalke, J., and Grabner, E. W. (1995). Electrochemical modelling of self-potential anomalies. *Surveys in Geophysics*, 16(1):107–120.

Straface, S., Rizzo, E., and Chidichimo, F. (2010). Estimation of hydraulic conductivity and water table map in a large-scale laboratory model by means of the self-potential method. *Journal of Geophysical Research: Solid Earth*, 115:B06105.

Stumm, W. and Morgan, J. J. (2012). *Aquatic chemistry: chemical equilibria and rates in natural waters*, volume 126. John Wiley & Sons.

Suski, B., Ladner, F., Baron, L., Vuataz, F.-D., Philippossian, F., and Holliger, K. (2008). Detection and characterization of hydraulically active fractures in a carbonate aquifer: results from self-potential, temperature and fluid electrical conductivity logging in the combioula hydrothermal system in the southwestern swiss alps. *Hydrogeology Journal*, 16(7):1319–1328.

Suski, B., Revil, A., Titov, K., Konosavsky, P., Voltz, M., Dagès, C., and Huttel, O. (2006). Monitoring of an infiltration experiment using the self-potential method. *Water Resources Research*, 42(8):W08418.

Tarantola, A. and Valette, B. (1982). Inverse problems= quest for information. *Journal of Geophysics*, 50(3):150–170.

Thanh, L. D. and Sprik, R. (2016). Permeability dependence of streaming potential coefficient in porous media. *Geophysical Prospecting*, 64(3):714–725.

Thony, J.-L., Morat, P., Vachaud, G., and Le Mouël, J.-L. (1997). Field characterization of the relationship between electrical potential gradients and soil water flux. *Comptes Rendus de l'Académie des Sciences - Series IIA - Earth and Planetary Science*, 325(5):317–321.

Timm, F. and Möller, P. (2001). The relation between electric and redox potential: evidence from laboratory and field measurements. *Journal of Geochemical Exploration*, 72(2):115–128.

Tokarev, V. and Gostin, V. (2003). Mount lofty ranges, south australia. *Cooperative Research Centre for Landscape Environments and Mineral Exploration (CRC LEME), 6p.*

Vinogradov, J., Jaafar, M., and Jackson, M. (2010). Measurement of streaming potential coupling coefficient in sandstones saturated with natural and artificial brines at high salinity. *Journal of Geophysical Research: Solid Earth*, 115(B12).

Vinogradov, J. and Jackson, M. D. (2015). Zeta potential in intact natural sandstones at elevated temperatures. *Geophysical Research Letters*, 42(15):2015GL064795.

Walker, E. and Glover, P. (2018). Measurements of the relationship between microstructure, ph, and the streaming and zeta potentials of sandstones. *Transport in Porous Media*, 121(1):183–206.

Wang, J., Hu, H., Guan, W., and Li, H. (2015). Electrokinetic experimental study on saturated rock samples: zeta potential and surface conductance. *Geophysical Journal International*, 201(2):869–877.

Wang, L.-X. and Mendel, J. M. (1992). Adaptive minimum prediction-error deconvolution and source wavelet estimation using hopfield neural networks. *Geophysics*, 57(5):670–679.

Wishart, D. N., Slater, L. D., and Gates, A. E. (2006). Self potential improves characterization of hydraulically-active fractures from azimuthal geoelectrical measurements. *Geophysical Research Letters*, 33(17).

Wishart, D. N., Slater, L. D., and Gates, A. E. (2008). Fracture anisotropy characterization in crystalline bedrock using field-scale azimuthal self potential gradient. *Journal of Hydrology*, 358(1-2):35–45.

Wurmstich, B. (1995). *3D self-consistent modeling of streaming potential responses: Theory and feasibility of applications in earth sciences*. PhD thesis, Texas A & M University.

Yeh, W. W.-G. and Yoon, Y. S. (1981). Aquifer parameter identification with optimum dimension in parameterization. *Water Resources Research*, 17(3):664–672.

Zhang, Y. and Paulson, K. V. (1997). Magnetotelluric inversion using regularized hopfield neural networks. *Geophysical Prospecting*, 45(5):725–743.

Zulfic, D., Barnett, S. R., and Van den Akker, J. (2003). *Mount Lofty Ranges Groundwater Assessment: Upper Onkaparinga Catchment*. Department of Water, Land and Biodiversity Conservation.

Zulfic, D., Love, A. J., South Australia, and Department of Water, and Biodiversity Conservation, L. (2008). *Hydrogeophysical mapping of fracture orientation and groundwater flow in the eastern Mount Lofty Ranges, South Australia*. Dept. of Water, Land and Biodiversity Conservation. OCLC: 436026105.